

Flow visualization through particle image velocimetry and computational fluid dynamics in realistic model of rhesus monkey's upper airway

金, 智雄

<https://hdl.handle.net/2324/1937186>

出版情報 : Kyushu University, 2018, 博士 (工学) , 課程博士
バージョン :
権利関係 :

Flow Visualization through Particle Image Velocimetry and Computational Fluid Dynamics in realistic model of rhesus monkey's upper airway

Ji-Woong KIM

A thesis for the degree of
Doctor of Philosophy

Interdisciplinary Graduate School of
Engineering Science
Kyushu University
Japan

April 2018

This thesis was reviewed and approved by the following:

Kazuhide Ito

Professor

Department of Advanced Environmental Science and Engineering

Faculty of Engineering Sciences

Kyushu University

Thesis Adviser

Chair of Committee

Masayuki Anyoji

Associate Professor

Department of Advanced Environmental Science and Engineering

Faculty of Engineering Sciences

Kyushu University

Taro Handa

Professor

Department of Advanced Science and Technology

Toyota Technological Institute

Thesis Summary

Individuals spend an increasing amount of time indoors leading to increased exposure to indoor air pollutants. It is necessary to clarify the detailed mechanism of inhalation exposure through airway. Inhalation toxicology studies and the development of respiratory drug delivery systems require biological testing by animals. However, the measurements by *in vivo* have many limitations owing to the complicated structure and small size of the nasal passage. Further, *in vivo* studies involving mammal surrogate models for inhalation toxicology studies have severe restrictions owing to ethics and protection.

In this study, I conducted an *in vitro* experiment and numerical prediction to investigate the flow distribution in the realistic geometry of a monkey airway as a representative surrogate mammal for test animals. *in vitro* experiment and numerical prediction models (*in silico*) were reproduced from CT data of an actual monkey airway for a 6-month-old male monkey whose scientific name is *Macaca fascicularis* and weighs 1.2 kg. Detailed measurements from the Particle Image Velocimetry (PIV) technique, as well as the numerical simulation through Computational Fluid Dynamics (CFD), are challenging in the understanding of

respiratory system. The purpose of the study included visualizing flow inside an upper airway with a complicated geometry.

PIV measurements of the *in vitro* provide an effective alternative to defining the flow patterns in realistic replicas of airway. PIV measurement was conducted under the oral and nasal inhalation condition. The numerical simulation was validated successfully using the observed 2D-PIV results. These results of measurement display the detailed mechanism of inhalation exposure of the physical behaviors. This study provides additional contributions in validating the use of CFD analyses to understand and predict monkey airway flows.

The contents of each chapter are summarized below,

Chapter1 introduce the necessary of clarify the detailed mechanism of inhalation exposure in airway for target monkey instead of the human. And objectives and organization of the dissertation.

Chapter 2 describes the PIV experiment method and the results of this study.

The results of PIV measurements at the 3D replica silicon model of a monkey airway then are showed using the 2-dimensional plane. A principles and applications of the basic PIV system is given in this chapter. The build-up procedure of the realistic model is described explicitly. The main content are described in this chapter on flow types, seeding, illumination, imaging, repetitive

correlation analysis, post-processing and result interpretation, with reference to experimental situations.

In Chapter 3, numerical methodology and turbulence model in use to the target airway monkey model is describes. For the grid independence study, the adequacy of grid resolution is tested by verifying fluid result with scalar velocities of PIV experimental result. In this chapter, four levels of grid resolution is adopted (4 million, 6 million, 8 million and 10 million total mesh cells with 10 prism layers). Hence the monkey airway geometry in case of 10 million total meshes is sufficient for predicting accuracy in this study.

In chapter 4, CFD prediction of airflow pattern in monkey airway model is compared with PIV experimental results using the monkey airway which has 10 million total mesh (in chapter 3). This analyses performed in this study use the Abe- Nagano - Kondoh model (LR-ANK) of low Reynolds number $k-\epsilon$. The airflow field under isothermal condition is visualized using velocity vector map and profile. This chapter aims to provide data with insight into the characteristic of flow patterns.

Chapter 5 describes conclusion, recommendations and future work for all content in this dissertation.

ACKNOWLEDGEMENTS

Firstly, I would like to express my sincere gratitude to my advisor Professor Kazuhide Ito for the continuous support of my doctoral studies and related research, for his great support, patience, motivation, enthusiasm, and immense knowledge. During the doctoral course, Prof. Ito encouraged, supported, and believed in me while actively steering my research. Without his guidance and encouragement, it would not have been possible to complete the research and finish writing my dissertation.

In addition to my advisor, I would like to thank the rest of my thesis committee: Prof. Taro Handa of Toyota Technological Institute and Prof. Masayuki Anyoji of Kyushu University, for their insightful comments and encouragement, but also for the hard questions which motivated me to widen my research to incorporate various perspectives.

Special thanks go to my colleague Dr. Nguyen Lu Phuong, who provided me with the tools that I needed to choose the right direction and successfully complete my dissertation. Without his precious support it would not have been possible to conduct this research.

I wish to acknowledge my lab members for their assistance and intellectual engagement: Dr. Yoo Sung-Jun, Dr. Chung Ju-Yeon, Alicia Murga and Kang Yu-Jin.

I would like to thank my family: my parents and my brother Noah for supporting me spiritually when I was writing my dissertation and for supporting me in life in general.

Last but not least, I would like to give my great appreciation of Ah-Reum - my wife. I couldn't have finished my PhD without her deep dedication and belief. Many thanks for leading me to come over hopelessness and loneliness with her meticulous care and considerations in every possible way. To my daughter, she is not born yet but already a part of my very soul and a motivation for me to accomplish this work.

CONTENT

Chapter 1 INTRODUCTION

1.1 MOTIVATION	1
1.2 OBJECTIVES	3
1.3 ORGANIZATION OF THE DISSERTATION.....	5
REFERENCE.....	7

Chapter 2 PARTICLE IMAGE VELOCIMETRY USING 3D REPLICA MONKEY AIRWAY

MODEL

2.1 PIV PRINCIPLE	9
2.2 3D REPLICA MONKEY AIRWAY MODEL	15
2.3 PIV APPARATUS AND EXPERIMENTAL PROCEDURES.....	16
2.3.1 Creation of a 3D silicon model	16
2.3.2 PIV measurement setup	18
2.4 RESULTS AND DISCUSSIONS	24
2.4.1 The case of PIV experiment.....	24
2.4.2 Uncertainty analysis of PIV measurements	26
2.4.3 Velocity vector map and profile obtained by PIV technique	30
2.4.4 Conclusion and discussions	44
REFERENCE.....	47

Chapter 3 NUMERICAL STUDY OF AIRFLOW PATTERN IN MONKEY AIRWAY MODEL

3.1 NUMERICAL ANALYSIS OF FLOW FIELD.....	49
3.1.1 Numerical methodology.....	49
3.1.2 Selection of turbulence model	54
3.2 NUMERICAL SETUP.....	66
3.2.1 Grid design.....	66
3.2.2 Inflow boundary profile prescription for numerical simulation of oral and nasal airflow	73
3.2.3 Grid independence	74
3.3 CONCLUSION AND DISCUSSIONS	75
REFERENCE.....	77

Chapter 4 VALIDATION FOR NUMERICAL SIMUATION AND AIRFLOW PATTERN IN
MONKEY AIRWAY MODEL

4.1 VALIDATION FOR NUMERICAL SIMULATION USING PIV RESULTS	79
4.2 COMPARISON OF CFD ANALYSIS RESULTS AND PIV EXPERIMENTAL RESULTS.....	84
4.3 CONCLUSION AND DISCUSSIONS.....	89

Chapter 5 CONCLUSION, RECOMMENDATIONS AND FUTURE WORK

5.1 CONCLUSION	91
5.2 RECOMMENDATION AND FUTURE WORK	94

CHAPTER 1

INTRODUCTION

1.1 MOTIVATION

The respiratory system is constantly being exposed to the various gases, harmful or not, contained in the ambient air, making its study an essential starting point in terms of human health and risk assessment due to inhalation. Due to the fact that the nose is a common site for particle deposition (Andersen I et al., 1982; Brain JD et al., 1979; Hounam RF et al., 1977; Lippman M., 1970; Proctor DF et al., 1987; Swift DL., 1981), and the absorption site of many gases and vapors (Aharonson EF et al., 1974; Brain JD et al., 1979; Morgan MS et al., 1977; Stott WT et al., 1984), this organ has the wide potential to be harmed by inhaled irritants – e.g ozone, formaldehyde, and sulfur dioxide (Buckley LA et al., 1984; Harkema JR., 1987; Monticello TM et al., 1987; Walker D., 1983). The protective function of the respiratory system makes it also vulnerable to several health risks, deriving in concerns for life quality management. In this instance, it becomes crucial to clearly define the detailed mechanisms of inhalation exposure through the airways for a deep understanding of phenomena like particle transport, deposition and mass transfer. Inhalation toxicology studies

and the development of respiratory drug delivery systems require biological animal testing. In order to estimate human inhalation from animal inhalation in a toxicology study, an acceptable extrapolation formula is required to indicate the relationship between animal and human body sizes and inhalation mechanisms. Fundamental information such as the analysis of the flow field created inside the airways is needed for further studies. Thus, previous studies have analyzed human models as well as other mammals models, such as rats, mice, dogs, and monkeys, to predict convective mass transfer characteristics for upper respiratory tracts and other fluid initiated parameters (Inthavong et al., 2014; Ito et al., 2016; Wen et al., 2008). Typically, rats, rabbits, and dogs have much more complex turbinate structures than primate mammals such as monkeys and humans (Carey et al., 2007). Based on monkey and human anatomical and physiological information, monkeys have been used as surrogate mammals for humans in inhalation toxicology studies due to the strong similarities between both respiratory tract structures at a gross and microscopic level (Corley et al., 2012; Hislop et al., 1984; Kepler et al., 1998; Martonen et al., 2001; Monticello et al., 1989).

However, the only previous attempt to investigate fluid flow in rhesus monkeys was done by Morgan et al. (1991) who observed flow patterns through dye-water transport in hollow acrylic molds of the rhesus monkey's nasal airways. Though the dye-water studies can provide qualitative information about the flow characteristics, they provide limited details of velocity data.

In this study, therefore, a monkey airway model that maintains most of the geometrical characteristics of respiratory structures from CT data of an actual monkey airway (6-month-old male, weight of 1.2 kg) has been developed. Then, an *in vitro* experiment to investigate the flow distribution in the realistic monkey airway geometry as a representative surrogate mammal for animal testing was conducted. The results of flow patterns in a realistic respiratory tract model using the Particle Image Velocimetry (PIV) technique, a 3-dimensional printer, and refraction control technique are hereby described.

The numerical simulation through Computational Fluid Dynamics (CFD) has been validated using the PIV experimental results. In addition, the visualization of flow inside the upper airways with a complicated geometry has been included. The experimental and numerical analyses have been conducted under oral and nasal inhalation conditions. The numerical simulation was validated successfully using the observed 2D-PIV results. These results of measurements show the detailed mechanisms of flow patterns. This study provides additional contributions in validating the use of CFD analysis to understand and predict monkey airway flows.

1.2 OBJECTIVES

The main objective of this dissertation aims to visualize results of Particle Image Velocimetry and numerical simulations in a realistic monkey airway model using various flow rates.

First target – Particle Image Velocimetry (PIV) for measuring airflow patterns of a monkey's upper airway

The great advantage of the PIV technique is that it indicates high resolution of flow velocity vector information of a whole plane in the flow field at one time and obtains instantaneous velocity information and patterns (2 or 3-dimensional). It has therefore mainly been used to study the structure of turbulent flow fields using instantaneous flow field information and experimentally induced flows, such as water flow in the limited area or around streamlined objects (air flow around wing profiles and plane models, etc.). In this study, a PIV experiment has been conducted to investigate the fluid flow patterns of the monkey upper airway by using transparent, realistic replica model with a working fluid instead of air.

Second target – Computational fluid dynamics (CFD) analysis validated by the PIV experimental results

Computational fluid dynamics (CFD) is a computerized method to predict airflow by using numerical methods and algorithms. For the numerical simulation, The Low Reynolds type k- ϵ model (Abe-Kondoh-Nagano type) was selected in terms of turbulence to consider viscous sub-layer on the near wall space. The CFD results were validated by using PIV experimental results.

The calculation in flow field was very challenging due to the complex geometry that has highly curved and narrow spaces in bifurcation/separation zones as it includes the nasal/oral cavity, pharynx, larynx until the trachea.

1.3 ORGANIZATION OF THIS DISSERTATION

Chapter 1 introduces the necessity of clarifying the detailed mechanisms of inhalation phenomena inside the airways in order to extrapolate monkey model information into human scale. It also includes the objectives and organization of this dissertation.

In Chapter 2, the PIV experimental method and its results were described. The velocity distribution of PIV experimental data in the 3D replica silicon model of a monkey airway are then shown using a 2-dimensional plane. The principles and applications of the basic PIV system are given in this chapter. The build-up procedure of the realistic model is described explicitly. The main contents are flow types, seeding, illumination, imaging, repetitive correlation analysis, post-processing and result interpretation, with reference to experimental situations.

In Chapter 3, numerical methodology and turbulence model that were used in the target airway monkey model are described. The adequacy of grid resolution was confirmed through five levels of grid resolution (4 million, 6 million, 8 million, 10 million and 12 million total mesh cells with 10 prism layers) to ensure prediction accuracy and efficient calculation time. Hence, the monkey airway geometry in case of 10 million elements mesh with 10 prism layers was considered to be sufficient in this study.

In chapter 4, CFD prediction of airflow patterns in the monkey airway model was compared with PIV experimental results using the case of the 10 million total mesh with 10 prism layers described in Chapter 3. The analyses performed in this study used the Abe- Nagano - Kondoh model (LR-ANK) of low Reynolds number $k-\varepsilon$ type. The airflow field under isothermal conditions was visualized using velocity vector maps and profiles. This chapter aimed to provide data with insight into the characteristic flow patterns and the validation using PIV experimental data.

Chapter 5 concludes by summarizing significant outcomes from each research section between Chapters 2 to 4. The final part of this chapter highlight the potential contribution of this study and provide recommendations for further work.

Reference

- 1-1) Andersen I and Proctor DF. The fate and effects of inhaled materials. In: *the nose: Upper airway Physiology and the Atmospheric Environment*. Elsevier Biomedical Press, Amsterdam, pp. 423-455. 1982.
- 1-2) Brain JD and Valberg PA. Deposition of aerosols in the respiratory tract. *Am. Rev. Respir. Dis.* 123:1325-1373. 1979.
- 1-3) Hounam RF and Morgan A. Particle deposition. In: *Respiratory Defense Mechanisms*, J. D. Brain, DF Proctor, and LM Reid (eds). Marcel Dekker, NY, pp.125-126. 1977.
- 1-4) Lippman M. Deposition and clearance of inhaled particles in the human nose. *Ann. Otol. Rhinol. Laryngol.* 79: 519-529. 1970.
- 1-5) Proctor DF, Andersen I , Adams GK, and Man SFP. Nasal mucociliary function in man. In: *Respiratory Tract Mucus*, Ciba Foundation Symposium 54 (new series), Elsevier/North Holland, Amsterdam, pp. 219-234. 1987.
- 1-6) Swift DL. Aerosol deposition and clearance in the human upper airways. *Ann. Biomed. Engl.* 9:593-604. 1981.
- 1-7) Aharonson EF, Menkes H, Gurtner G, Swift DL, and Proctor DF. The effect of respiratory airflow rate on the removal of soluble vapors by the nose. *J. Appl. Physiol.* 37: 654-657. 1974.
- 1-8) Morgan MS and Frank R. Uptake of pollutant gases by the respiratory system. In: *Respiratory Defense Mechanisms*, JD Brain, DF Proctor, and LM Reid (eds). Marcel Dekker, NY, pp. 157-189. 1977.
- 1-9) Stott WT and McKenna MJ. The comparative absorption and excretion of chemical vapors by the upper, lower, and intact respiratory tract of rats. *Fundam. Appl. Toxicol.* 4: 594-604. 1984.
- 1-10) Buckley LA, Jiang XZ, James RA, Morgan KT, and Barrow CS. Respiratory tract lesions induced by sensory irritants at the RD50 concentration. *Toxicol Appl. Pharmacol.* 74: 417-429. 1984.
- 1-11) Harkema JR, Plopper CG, Hyde DM, St. George JA, Wilson DW, and Dungworth DL. Response of the macaque nasal epithelium to ambient levels of ozone: A morphologic and morphometric study of the transitional and respiratory epithelium. *Am. J. Pathol.* 1128: 29-44. 1987.
- 1-12) Monticello TM, Morgan KT, Everitt JI, and Popp JA. Effects of formaldehyde gas on the respiratory epithelium in the rat. *Am. J. Anat.* 169: 31-43. 1987.
- 1-13) Walker D. Histopathology of the nasal cavity in laboratory animals exposed to cigarette smoke and other irritants. In: *Nasal Tumors in Animals and Man*, Vol. III, G Reznik and SF Stinson (eds). CRC Press, Boca Raton, FL, pp. 115-135. 1983.

- 1-14) Inthavong, K., Shang, Y., Tu, J. Surface mapping for visualization of wall stresses during inhalation in a human nasal cavity. *Respir. Physiol. Neurobiol.* 190, 54–61. <https://doi.org/10.1016/j.resp.2013.09.004>. 2014
- 1-15) Ito, K., Mitsumune, K., Kuga, K., Phuong, N.L., Tani, K., Inthavong, K. Prediction of convective heat transfer coefficients for the upper respiratory tracts of rat, dog, monkey, and humans. *Indoor Built Environ.* 26, 828–840. <https://doi.org/10.1177/1420326X16662111>. 2016.
- 1-16) Wen, J., Inthavong, K., Tu, J., Wang, S. Numerical simulations for detailed airflow dynamics in a human nasal cavity. *Respir. Physiol. Neurobiol.* 161, 125–35. <https://doi.org/10.1016/j.resp.2008.01.012>. 2008.
- 1-17) Carey, S.A., Minard, K.R., Trease, L.L., Wagner, J.G., Garcia, G.J.M., Ballinger, C.A., Kimbell, J.S., Plopper, C.G., Corley, R.A., Postlethwait, E.M., Harkema, J.R. Three-Dimensional Mapping of Ozone-Induced Injury in the Nasal Airways of Monkeys Using Magnetic Resonance Imaging and Morphometric Techniques. *Toxicol. Pathol.* 35, 27–40. <https://doi.org/10.1080/01926230601072343>. 2007
- 1-18) Corley, R.A., Kabilan, S., Kuprat, A.P., Carson, J.P., Minard, K.R., Jacob, R.E., Timchalk, C., Glenny, R., Pipavath, S., Cox, T., Wallis, C.D., Larson, R.F., Fanucchi, M. V., Postlethwait, E.M., Einstein, D.R. Comparative computational modeling of airflows and vapor dosimetry in the respiratory tracts of rat, monkey, and human. *Toxicol. Sci.* 128, 500–516. <https://doi.org/10.1093/toxsci/kfs168>. 2012.
- 1-19) Hislop, A., Howard, S., Fairweather, D.V.I. Morphometric studies on the structural development of the lung in *Macaca fascicularis* during fetal and postnatal life. *J. Anat* 138, 95–112. 1984.
- 1-20) Kepler, G.M., Richardson, R.B., Morgan, K.T., Kimbell, J.S. Computer simulation of inspiratory nasal airflow and inhaled gas uptake in a rhesus monkey. *Toxicol. Appl. Pharmacol.* 150, 1–11. <https://doi.org/10.1006/taap.1997.8350>. 1998.
- 1-21) Martonen, T.B., Katz, I.M., Musante, C. A Nonhuman Primate Aerosol Deposition Model for Toxicological and Pharmaceutical Studies. *Inhal. Toxicol.* 13, 307–356. <https://doi.org/10.1080/08958370117552>. 2001.
- 1-22) Monticello, T.M., Morgan, K.T., Everitt, J.I., Popp, J. a. Effects of formaldehyde gas on the respiratory tract of rhesus monkeys. Pathology and cell proliferation. *Am. J. Pathol.* 134, 515–27. <https://doi.org/10.1097/00043764-199004000-00003>. 1989.
- 1-23) Morgan, K.T., Kimbell, J.S., Monticello, T.M., Patra, A.L., Fleishman, A. Studies of inspiratory airflow patterns in the nasal passages of the F344 rat and rhesus monkey using nasal molds: Relevance to formaldehyde toxicity. *Toxicol. Appl. Pharmacol.* 110, 223–240. [https://doi.org/10.1016/S0041-008X\(05\)80005-5](https://doi.org/10.1016/S0041-008X(05)80005-5). 1991.

CHAPTER 2

PARTICLE IMAGE VELOCIMETRY USING 3D REPLICA MONKEY AIRWAY MODEL

This chapter describes the PIV experiment method and the results of this part of the study. The results of PIV measurements at the 3D replica silicon model of a monkey airway are then shown using a 2-dimensional plane. The principles and applications of the basic PIV system are given in this chapter and the build-up procedure of the realistic model is described explicitly. The main contents hereby described are flow types, seeding, illumination, imaging, repetitive correlation analysis, post-processing and result interpretation, with reference to experimental situations.

2.1 PIV PRINCIPLE

PIV technique has been developed to measure flow field of scalars and vectors in the experimental fluid from the 1980's (Adrian 1991). The great advantage of PIV technique are that it indicate high resolution flow velocity vector information of a whole plane in the flow field in one time and obtain instantaneous velocity information and 2 or 3-dimensional flow pattern of velocity information. It has therefore mainly been used to study the structure of

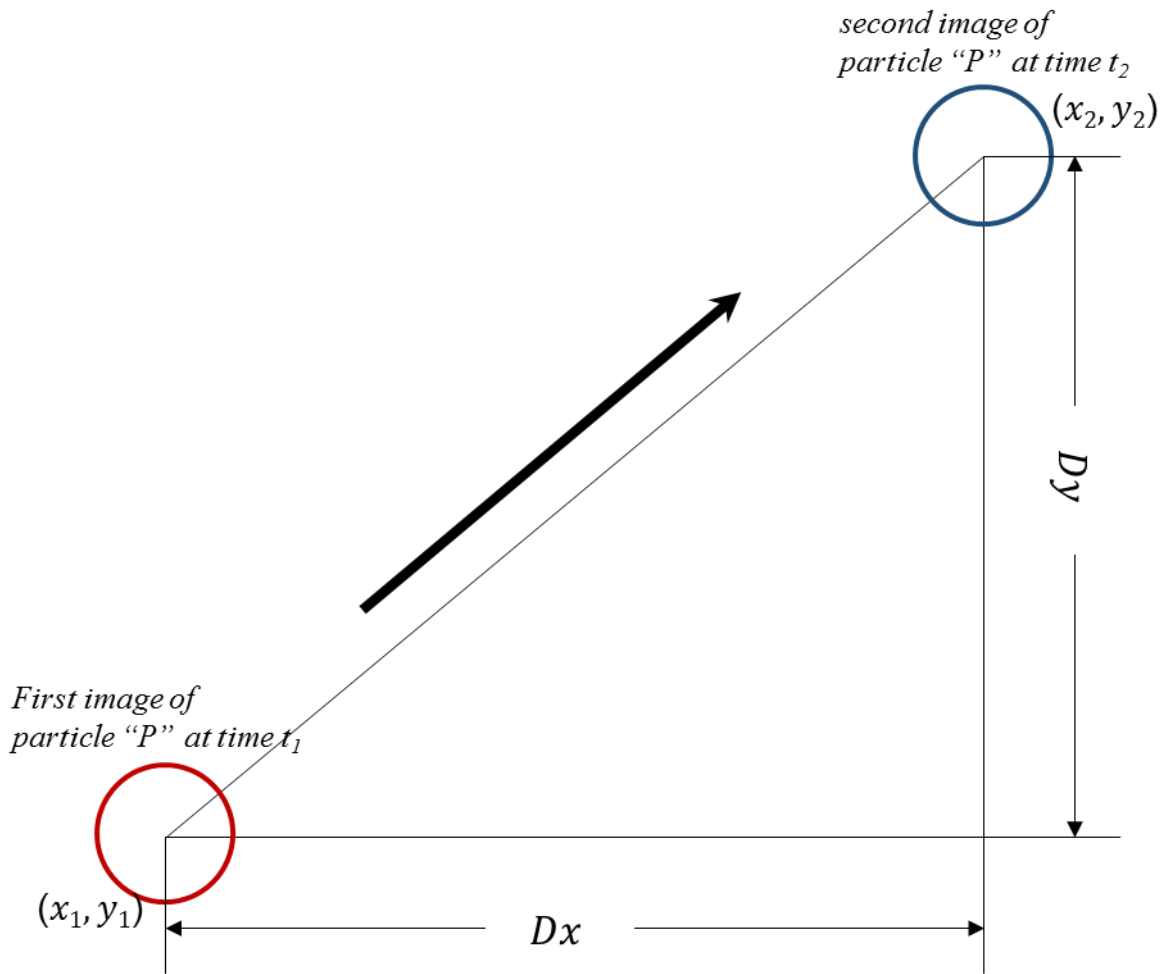


Figure 2.1 Diagram of PIV conceptual diagram

turbulent flow fields using instantaneous flow field information (Westerweel, 1996; Haigermoser, 2008) and the experimentally induced flows, such as water flow in the limited area or around streamlined objects, air flow around wing profiles and plane models, etc. (Adrian 1991; Stanislas et al. 2000). PIV techniques can be characterized as an optical method of flow visualization that measures the displacement of tracer particles that in the experimental fluid due to its non-intrusive character.

Using a high-speed digital camera, the particle moving is captured by capturing scattered light from the individual particles. The local velocity of a flow field is determined by the micro-linear distance and direction in which the tracer particles passing through a certain point move

during the minute time interval. The displacement of particle in the target region is calculated by captured successive images. To approximate u velocity of x-component and v velocity of y-component to the actual flow velocity, the displacement of particle must be sufficiently small. In other words, the trajectory drawn by the particles must be guaranteed to be linear and isotropic. PIV conceptual diagram is shown in Figure 2.1. u and v is expressed by following equation 2.1.

$$u = \lim_{t_2 \rightarrow t_1} \frac{x_2 - x_1}{t_2 - t_1} = \frac{\Delta x}{\Delta t}, v = \lim_{t_2 \rightarrow t_1} \frac{y_2 - y_1}{t_2 - t_1} = \frac{\Delta y}{\Delta t} \dots\dots\dots (2.1)$$

The captured PIV images are analyzed by divided image into a grid of interrogation areas that is smaller sub-areas. Then, a displacement vector for the tracer particles is detected in each interrogation area by using the cross-correlation statistical calculation. The process is repeated on each next interrogation area until reaching the last interrogation area. The single exposure frame is used to measure the single exposed image pairs between successive frames, by means of cross-correlation. The objective of the method is to locally find the best match between the images in a statistical sense (Figure 2.2). The correlation function R_{II} requires the evaluation of the following equation 2.2 (Raffel et al, 2007):

$$R_{II}(x, y) = \sum_{i=-K}^K \sum_{j=-L}^L I(i, j)I'(i+x, j+y) \dots\dots\dots (2.2)$$

where $I(i, j)$ represents the intensity value for the (i, j) pixel. This function statistically measures the degree of correlation between two samples I and I' for a given shift (x, y) . The shift position where the pixel values align with each other gives the highest cross-correlation value, and this represents the average displacement of the particles in a given interrogation window. A high cross-correlation peak is identified when a particle match up with its corresponding shifted partner, and low cross-correlation peaks may be observed when single particle match up with surrounding particles. The former correlation is correct correlation, and the latter one is called random correlation or undesired correlation. If the shift of each particle is stable then the correct correlation produce a peak value that must be higher than the noise peaks produced by the random correlations. The height of the main peak relates to the number of particle pair correlations and hence to the signal to noise ratio. Seeding particles entering or leaving the interrogation area between the recording of the first and the second image, will not contribute to the true correlation. They do contribute to the random correlations that make decrease the signal-to-noise ratio. This phenomenon is called as “loss-of-pairs” or “signal drop-out”. Determination of the location of the peak value is the key factor to define displacements precisely. R_{II} can be decomposed into the following components

$$R_{II} = R_C + R_P + R_F + R_{D^-} + R_{D^+} \dots\dots\dots (2.3)$$

R_C is the convolution of mean image intensity, R_P is the pedestal component resulting from each

particle image correlating with itself, and R_F is the fluctuating component resulting from the correlation between fluctuating image intensity with mean image intensity (Adrian, 1988). The positive and negative displacement components are R_D^+ and R_D^- , respectively (see Figure 2.3). The signal used to measure displacement is contained only in the R_D^+ component. Contributions from all other components of the correlation function may bias the measurements, add random noise to the measurements, or even cause erroneous measurements. Therefore, it is desirable to reduce or eliminate as much as possible the other components. In practice, to efficiently compute the correlation plane, Fourier transform processing is adopted in PIV. A camera image may be considered a two-dimensional signal field analogous to a one-dimensional time series. Fast Fourier Transforms (FFT's) are used to speed up the cross-correlation process. The FFT's cross-correlation method resulted in a single peak on the correlation plane that represented the average displacement of the particles in the window during the time delay between two frames. Instead of performing a sum over all elements of the sampled region, the operation can be reduced to a complex conjugate multiplication of each corresponding pair of Fourier coefficients. The cross-correlation was then obtained by using the FFT's algorithm in Equation 2.4 and 2.5:

$$R_{II}(x, y) = f(x, y) \otimes g(x, y) \dots\dots\dots (2.4)$$

$$F\{R_{II}(x, y)\} = F(u, v)G^*(u, v) \dots\dots\dots (2.5)$$

where $F(u,v)$ and $G(u,v)$ are the Fourier transforms of $f(x, y)$ and $g(x, y)$, $*$ denotes a complex conjugate and F represents a Fourier transform. The cross-correlation could be computed become simpler and less computer expensive by taking the inverse Fourier transform of the product of the FFT's of each of the interrogation areas. The position of the correlation peak was then estimated to sub-pixel accuracy by using a Gaussian fit function.

In this part the basic principles of PIV have been introduced. The following section describes the PIV system and experimental practices used in this study.

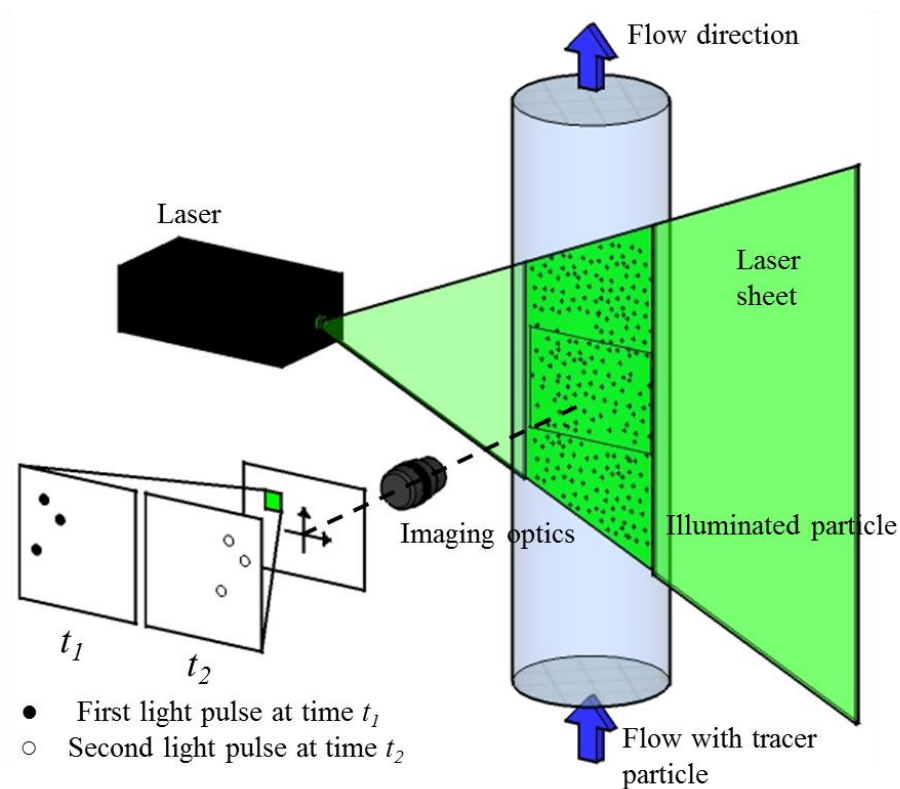


Figure 2.2 Description of PIV system

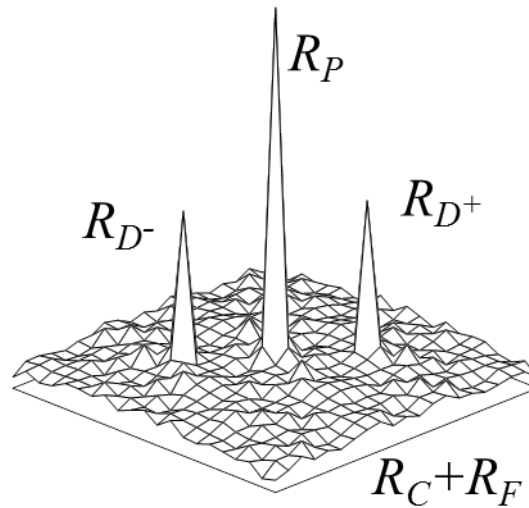


Figure 2.3 Spatial cross correlation function

2.2 3D REPLICA MONKEY AIRWAY MODEL

To perform the PIV measurements, a monkey air way model was made from silicon. The present silicon model was developed from a 3D replica model of the monkey using computed tomography (CT) data. Figure 2.4 is shown the CT data. The subject monkey, *Macaca fascicularis*, was a 6-month-old male with a weight of 1.2 kg. Micro-CT imaging from the upper airway of the monkey including nasal and oral cavities and trachea were performed at a resolution of 200 μm . The original CT images were converted into a compatible file format by using Mimics $\text{\textcircled{R}}$ (Materialise NV) to generate and modify 3D surface models of medical images. A surface model was generated from continuous 2D contour data by translating segmented, modified, and smoothed contour points into a data series that was loaded into ANSYS preprocessing software package ICEM-CFD (ANSYS Inc.). Additionally, ICEM-CFD was used to modify the surface mesh and create a volume mesh of the model with unstructured

tetrahedral elements (See figure 2.5). Surface geometries of the monkey respiratory tract were also exported as an STL file format. The monkey respiratory tract model possessed a length and inner surface area approximately corresponding to 1.05×10^{-1} m and 2.81×10^{-5} m², respectively. Table 2.1 lists the details of the monkey's geometry.

Table 2.1 Details of the 3D replica monkey model by using the STL data.

	Original data	Scale-up 1.5 time data
Total inner surface area (m ²)	2.81×10^{-5}	6.32×10^{-5}
Total inner volume (m ³)	1.27×10^{-5}	4.29×10^{-5}
Total length (m)	1.05×10^{-1}	1.58×10^{-1}
Maximum height excluding pipe (m)	4.32×10^{-2}	6.48×10^{-2}
Maximum width excluding pipe (m)	2.81×10^{-2}	4.22×10^{-2}
Area of right naris (m ²) /Equivalent diameter (m)	$5.48 \times 10^{-6} / 2.64 \times 10^{-3}$	$1.23 \times 10^{-5} / 3.96 \times 10^{-3}$
Area of left naris (m ²) /Equivalent diameter (m)	$5.46 \times 10^{-6} / 2.64 \times 10^{-3}$	$1.23 \times 10^{-5} / 3.96 \times 10^{-3}$
Area of mouth (m ²) /Equivalent diameter (m)	$4.08 \times 10^{-6} / 7.21 \times 10^{-3}$	$9.18 \times 10^{-5} / 1.08 \times 10^{-2}$
Area of trachea (m ²) /Equivalent diameter (m)	$2.81 \times 10^{-5} / 5.98 \times 10^{-3}$	$6.32 \times 10^{-5} / 8.97 \times 10^{-3}$

2.3 PIV APPARATUS AND EXPERIMENTAL PROCEDURES

2.3.1 Creation of a 3D silicon model

In order to create a 3D silicone model, a 3D respiratory tract model was created with a 3D

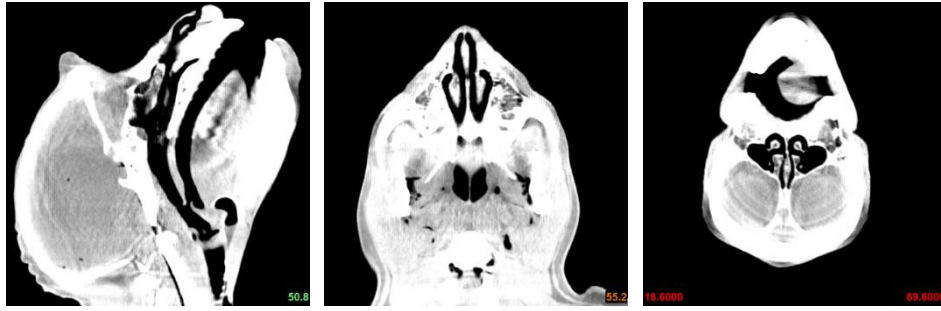


Figure 2.4 CT data of a real monkey airway using Mimics ®(Materialise NV)



Figure 2.5 Computational geometry and mesh of virtual airway

printer (CMET Inc., ATOMm-4000) by using the STL data. First, a negative model that represented the monkey's upper airway was constructed from a water-soluble plastic. The lamination layer in the z-direction corresponded to $15\ \mu\text{m}$ and the object resolution corresponded to $20 \times 20\ \mu\text{m}$ in the x- and y-direction. Following a precise and suitable surface treatment of a negative model, the model was placed in a rectangular box, and transparent silicon material (TSR-833) was poured into the box. Finally, a plastic (a negative model in silicon material) was dissolved and flushed out by water to create a positive model that corresponded to a solid containing void space to reproduce the respiratory tract geometry with a transparent silicone material as shown in figure 2.6.

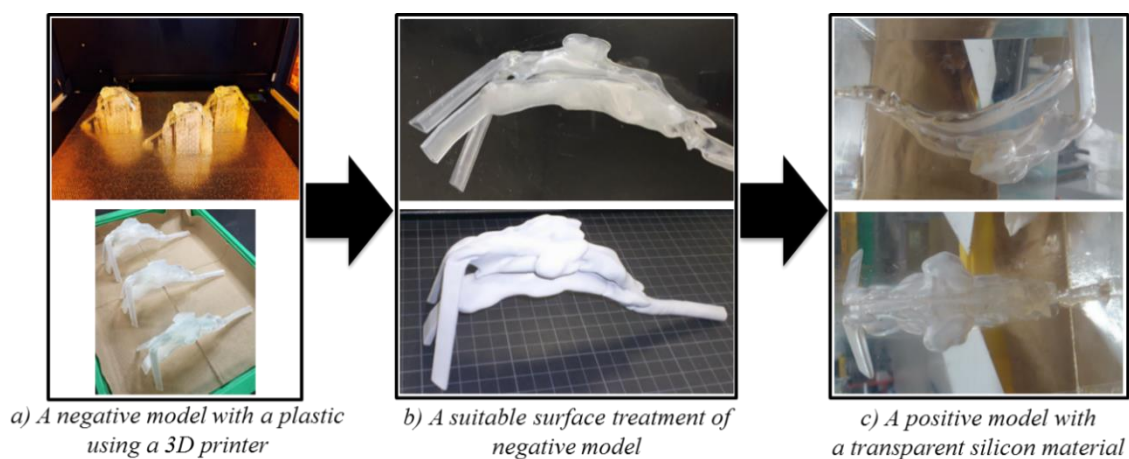


Figure 2.6 A silicone monkey airway model created by a 3D printer

In order to ensure the measurement accuracy of the PIV experiment, a silicone airway model that was 1.5 times larger than the actual size was created. This CT data was provided by third parties (Ina-Research Co.) and corresponds to secondary usage of in vivo data acquired in experiments conducted completely separately from this study.

2.3.2 PIV measurement setup

The PIV is a technique for measuring the velocities of tracer particle ensembles from images of particles captured at successive times by assuming that the particle movement is the same as the fluid motion. The instantaneous velocity field that plays an important role in the structure of turbulent flow fields is measured by using light scattered from tracer particles on an illuminated plane. In the PIV algorithm, the consecutive images are compared to calculate the particle displacement of the interested area. The two velocity vectors between pairs of frames at any point are determined by dividing the distance of displacement by the time delay. The analysis of the PIV images is conducted by dividing the single frame into an interrogation area

(IA) consisting of smaller sub-areas. A displacement vector for the tracer particles is detected in each IA by using a cross-correlation statistical method. All the fore-mentioned procedures are repeated in the next interrogation area until all areas of captured frames are completed. In the PIV measurement in the study, the visualization of the 2D flow field in the monkey upper airway was conducted by using silver-coated hollow glass spheres with a mean diameter of 10 μm as tracer (seeding) particles. The movement of tracer particles were captured by using a high-speed camera (Photron, Inc., FASTCAM SA4 model 500K-C1) and recorded on a complementary metal-oxide semiconductor (CMOS) sensor. The density of the hollow glass spheres corresponded to 1.4 g/cm^3 . The field of view in the CMOS camera was focused on the target region by illuminating a light sheet with a thickness of 3 mm discharged from the continuous wave (CW) laser. A CW laser (Beamtech Optronics, Diode-pumped solid-state green laser 2W) with a wavelength of 532 nm was used as the light source. The image data were analyzed with Dynamic studio 3.31. The frame rate was defined as 500 frames per second and 2000 frames per second based on the flow rate for the flow velocity at a full size corresponding to 1024×1024 pixels. Initially, the particle displacements were determined by using an interrogation size corresponding to 128×128 pixels. The vector fields were analyzed by using the cross-correlation method adaptive based on fast Fourier Transform (FFT) algorithms. The size of the initial interrogation area (IA) was set as 8×8 pixels with a 50% overlap to satisfy the Nyquist criterion. The adaptive correlation method iteratively calculated velocity vectors with an initial IA of a size equal to N times the size of the final IA and used the

intermediary results as information for the next IA of a smaller size until the final IA size was reached. The spurious vectors on the vector field were removed by using velocity range, peak ratio, and local median filters. The vector statistics map was calculated by using 5456 velocity vector maps of an averaged velocity vector obtained from two consecutive images. Figures 2.7 show the experimental setup with the monkey airway model for the PIV system.

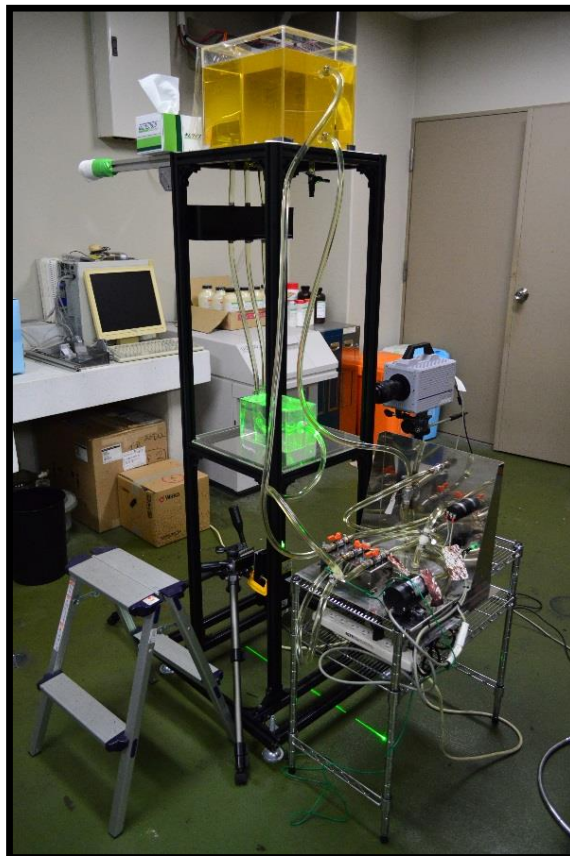


Figure 2.7 The experimental setup for PIV

The silicone material forming a positive model for a monkey upper airway and pure water possesses a different refractive index (RI). In order to capture particle motion by using a laser light sheet without refraction, it is necessary to match the refractive index of the silicone material with the working fluid. Because, if the light passes through different material, the refraction happen. Then we can't get the correct image (See figure 2.8).

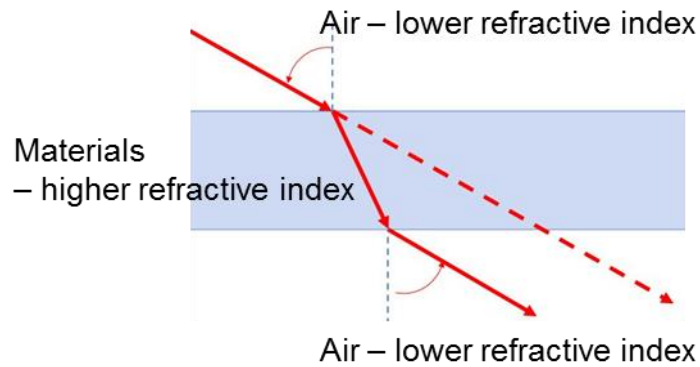
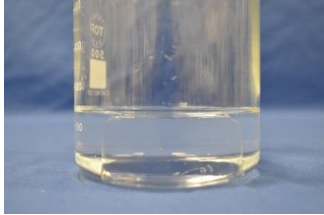
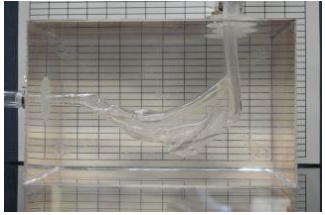
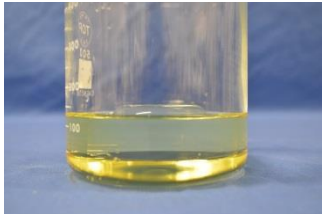

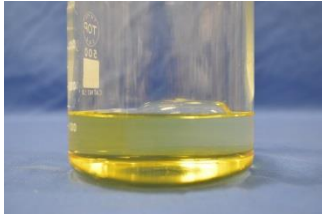
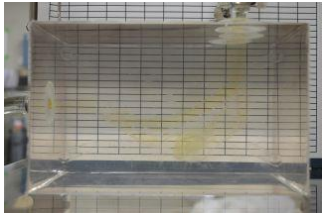


Figure 2.8 The action of refractions

In order to eliminate the refraction of laser sheet, we used water/sodium iodide mixture as working fluid. The Refractive index (RI) of the working fluid and silicon material model is matched with the naked eye. In the experiment, a 61/39 water/sodium iodide mass percentage mixture was used as a working fluid to match the RI of the flow of the working fluid and the silicone material constituting the monkey airway model. The refractive index of the NaI solution changed based on the temperature. With respect to a solubility of the NaI solution dependent on temperature, the PIV experiment was conducted at a constant temperature. The RI of the experiment was specified as 1.413. The gridline examination for matching the RI is shown in table 2.2.

Table 2.2 Refractive index matching using Grid line.

Water (ml)	Sodium Iodide(g) (NaI)	Refractive index of aqueous NaI solution	Picture	Verification of Gridline
100	0	1.336		
	42	1.390		
	62	1.413		

A liquid was used as a working fluid as opposed to air, and thus the Reynolds number should be the same based on the inhalation condition in real airflow in the numerical simulations as well as in the experimental measurements. Given that model is scaled by a factor of 1.5, the relationship is defined according to equation 2.6 and equation 2.7 as follows:

$$V_{working\ fluid} = \frac{v_{working\ fluid}}{v_{air}} \frac{L_{real}}{L_{silicone\ model}} V_{air} \dots\dots\dots(2.6)$$

$$Q_{working\ fluid} = V_{working\ fluid} \times A_{silicone\ model} = \frac{L_{siliconemodel}}{L_{real}} \frac{v_{NaI}}{v_{air}} Q_{air} \dots\dots\dots(2.7)$$

where $V_{working\ fluid}$ denotes the representative velocity in the trachea, $Q_{working\ fluid}$ denotes the

volumetric flow rate, ν denotes the kinematic viscosity of the fluid, and L denotes the length scale (m) of the trachea ($L_{silicone\ model}/L_{real}=1.5$). Additionally, A denotes the representative area (m^2) of the trachea. The kinematic viscosity of the working fluid corresponds to $\nu_{working\ fluid} = 0.712 \times 10^{-6} m^2/s$ as determined by using a Cannon-Fenske routine viscometer(See figure 2.9, table 2.3).

Table 2.3 Kinematic viscosity of NaI solution for PIV.

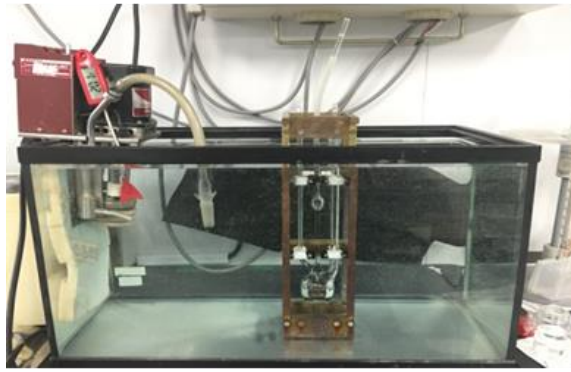
water 100ml, NaI 63g, refractive index 1.413, 20°C				
20°C	Dropping time(s)			average of time
	1	2	3	
NaI aq	55.533	55.531	55.535	55.533
H ₂ O	61.225	61.216	61.280	61.240

T(°C)	μ_{H_2O} (mPa·s)	μ_{H_2O} (kg/m·s)
15	1.140000	0.001140
16	1.110000	0.001110
17	1.083000	0.001083
18	1.056000	0.001056
19	1.030000	0.001030
20	1.005000	0.001005

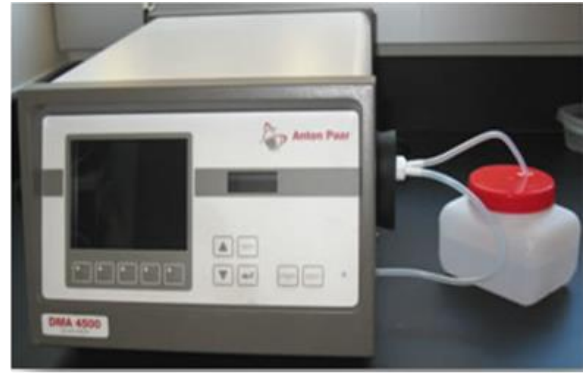
μ_{NaI}	0.00091
-------------	---------

	$\rho_{NaI\ aq}$ (g/cm ³)	$\rho_{NaI\ aq}$ (kg/m ³)
15.000	1.285	1284.800
19.300	1.282	1282.300
20.100	1.280	1279.587

$\nu_{NaI\ aq}$ (m ² /s)	0.000000712
-------------------------------------	-------------



Viscometer



Density meter DMA4500

Figure 2.9 The equipment for measurement of viscosity and density

The density ($\rho_{working\ fluid}$) corresponds to $1.28 \times 10^3 \text{ kg/m}^3$, and the temperature of the working fluid and surrounding environment are maintained at 20°C during the experiment. The flow rate of the working fluid on the trachea was controlled by using a flow control valve placed behind a high-pressure flowmeter (KOFLOC, model RK1400 with an accuracy of $\pm 2\%$). In the experiment, the condition of the monkey upper airway model was reproduced for nasal and oral cavities by connecting a pump to the entrances of the oral and nasal cavities. The monkey upper airway model was inverted to control the inflow working fluid profile approaching nasal and/or oral cavities. Working fluid was supplied from the top to bottom, and the formation of fully developed working fluid profile in supplied tube was confirmed in the preliminary experiment.

2.4 RESULTS AND DISCUSSIONS

2.4.1 The case of PIV experiment

In order to measure PIV by using a 3D silicon monkey airway model, the case is divided into two parts under oral and nasal inhalation. With respect to the oral inhalation, the nasal cavity entrance (i.e., the nostril) was closed and vice versa. The flow rate of the working fluid (Q_{Nal}) ranged from 0.2826 L/min to 1.5544 L/min in accordance with the Reynolds number matching

of air flow rate, respectively. Table 2.4 shows the experimental cases of PIV measurement based on the Reynolds number setting.

Table 2.4 Cases of PIV measurements based on Reynolds number matching under seven types of oral and nasal inhalation conditions.

Q_{air} (L/min)	$Q_{working\ fluid}$ (L/min)	$V_{working\ fluid}$ (m/s)	V_{air} (m/s)	Reynolds number (Re)	Nominal time constant (s)	Recording time (s)
4	0.2826	0.0745	2.3725	938	9.12	10.914
6	0.4239	0.1118	3.5587	1407	6.41	10.914
10	0.7066	0.1863	5.9312	2346	3.64	5.547
14	0.9892	0.2608	8.3037	3284	2.60	5.547
18	1.2718	0.3353	10.6762	4222	2.03	2.7285
20	1.4121	0.3725	11.8624	4692	1.84	2.7285
22	1.5544	0.4098	13.0486	5161	1.49	2.7285

The distance between the CMOS camera and illumination section with respect to the laser light sheet are considered to divide the target X-Y plane into two regions, namely the cavity and trachea regions as shown in figure 2.9.

In the cavity region, lines L1 and L2 were adopted for the oral inhalation condition and line L3 and L4 were adopted for the nasal inhalation condition to discuss the velocity profile of working fluid. In the trachea region, the visualized target region was consistent with respect to the oral and nasal inhalation conditions. The velocity profiles of the oral and nasal inhalation conditions were compared on lines L5 and L6 at the trachea region. The distances of the cross line (from L1 to L6) at the PIV measurements were normalized by dividing them

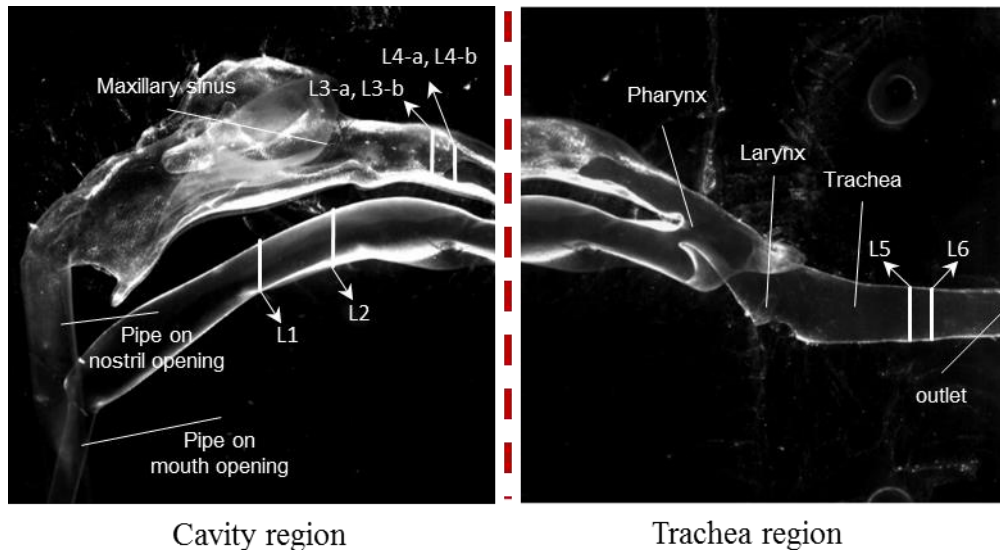


Figure 2.9 Visualized target region in 2-dimensional captured picture.

with the diameter of inlet (D). The non-dimensional distance was defined as dependent on the diameter of the cross line along the Y-axis, respectively. Individual non-dimensional distances were compared with different diameters of each cross line.

2.4.2 Uncertainty analysis of PIV measurements

In order to examine the PIV results, a preliminary PIV experiment was conducted to locate a suitable tracer particle by using particles of mean diameter (d_p) corresponding to 10 μm and 60 μm under oral inhalation with an airflow rate of 10 L/min. The results indicated that the size of the tracer particles was of particular importance in the PIV measurement. Generally, the magnitude of the drag force increased with the frontal area of a sphere that impinges on the fluid, and it can influence particle movement. The density of the permeable tracer particle ($d_p = 60 \mu\text{m}$) was fairly identical to the working fluid density ($\rho = 1.28 \times 10^3 \text{ kg/m}^3$). The tracer ($d_p = 10 \mu\text{m}$) with a density of $1.4 \times 10^3 \text{ kg/m}^3$ displayed a discrepancy of approximately 9%.

Gravitational settling velocity of the tracer particle ($d_p = 10 \mu\text{m}$) as estimated by Stokes' Law corresponded to $7.2 \times 10^{-6} \text{ m/s}$. In a centrifugal force field, a centrifugal force deflects the tracer particle from the actual fluid flow in the flow in the bending tube. In figure 2.10, the branch has a tangential velocity component and a velocity component and has a radial velocity component [m/s]. The direction and force of gravity equilibrium do not move. The order of the settling velocities was considerably smaller than average convective velocity in the cavity and trachea, and these were negligible. It is also necessary to verify deflection by a centrifugal force acting on tracer particle as follows:

$$\tan \theta = \frac{v_r}{u_t} = \frac{\rho_p d_p^2}{18\mu} \left(1 - \frac{\rho}{\rho_p}\right) \frac{u_t}{r} \dots\dots\dots (2.8)$$

where v_r denotes settling velocity, and u_t denotes representative fluid velocity. In the PIV measurement, the degree of deflections of rotational motion and particle motion ($\tan \theta_{4L/min}$, $\tan \theta_{10L/min}$ and $\tan \theta_{20L/min}$) corresponded to 2.0×10^{-5} , 4.6×10^{-5} , and 9.2×10^{-5} , respectively. The values were reasonably small ($\tan \theta < 0.01$), and it was concluded that the tracer particle ($d_p = 10 \mu\text{m}$) perfectly followed the motion of the working fluid.

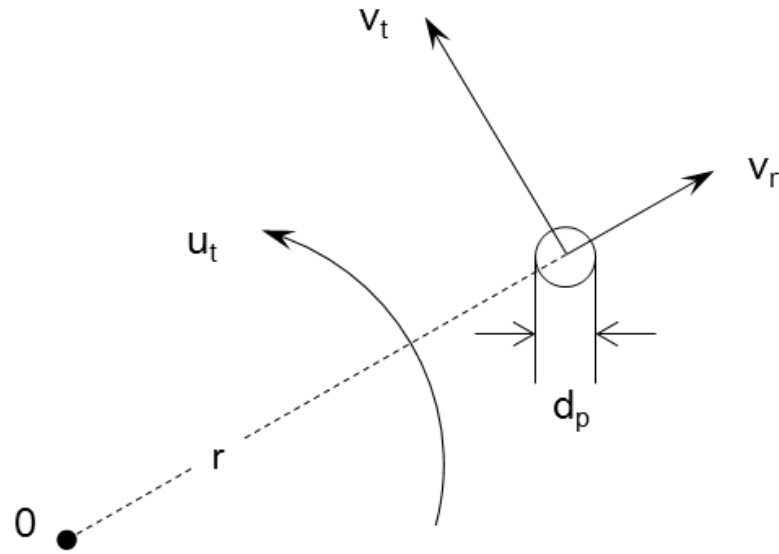


Figure 2.10 Particle motion in a centrifugal field

In order to visualize a flow pattern, PIV measurement was conducted using with tracer particles of mean diameter corresponding to $10\ \mu\text{m}$ and $60\ \mu\text{m}$ under oral inhalation of $10\ \text{L}/\text{min}$. The normalized scalar velocity in the trachea region is shown as figure 2.11. The tracer ($d_p = 10\ \mu\text{m}$) was coated with silver, and relatively definite visualization images were obtained. In case of the tracer ($d_p = 60\ \mu\text{m}$), an unstable distribution was observed because of the negative influence of the drag force in the fully developed fluid flow. Figure 2.12 shows a comparison of scalar velocity profiles with two upstream locations (line L5 and L6). The amplitudes of error bars correspond to the standard deviation of the measurements. On the near top surface, the drag force had a larger impact on the tracer (with $d_p = 60\ \mu\text{m}$) than on the tracer (with $d_p = 10\ \mu\text{m}$).

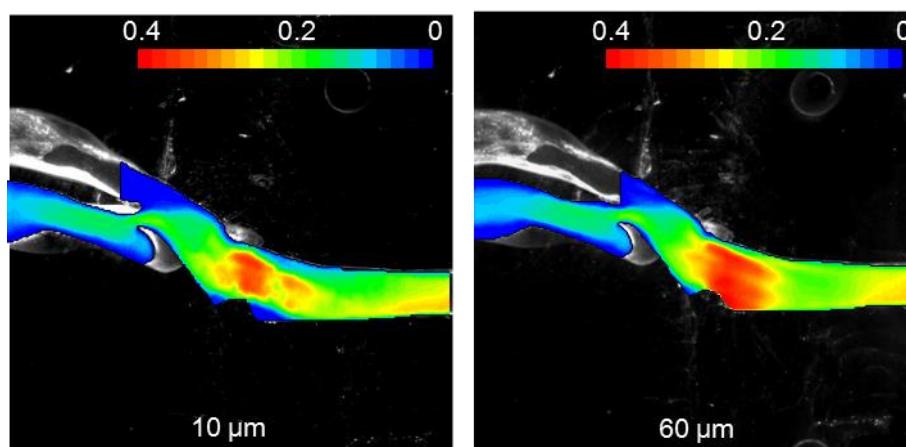


Figure 2.11 A flow pattern of normalized scalar velocity in the trachea region with tracer particles of mean diameter corresponding to $10\ \mu\text{m}$ and $60\ \mu\text{m}$ by PIV under oral inhalation of $10\ \text{L}/\text{min}$.

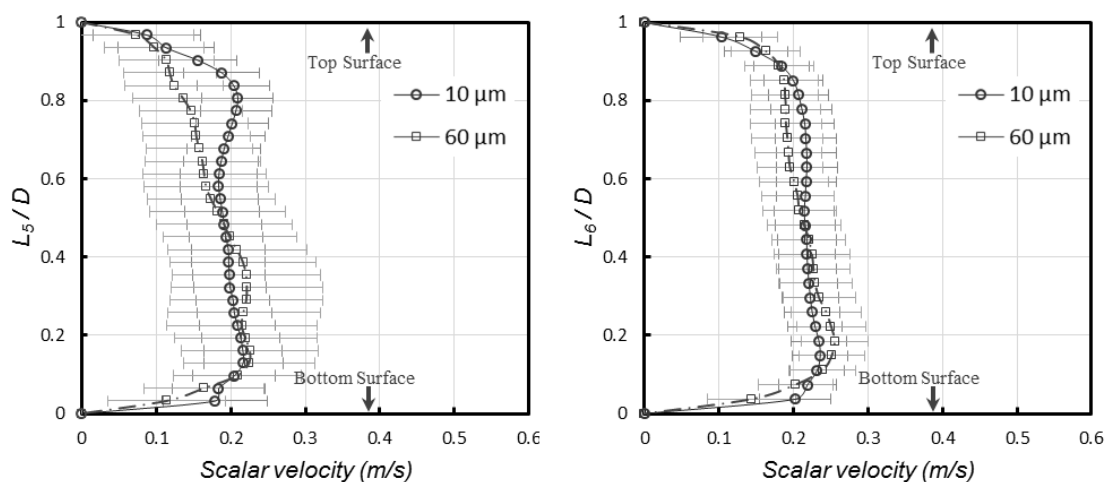


Figure 2.12 Profile with standard deviation on line L_5 and L_6 under oral inhalation of $10\ \text{L}/\text{min}$

The velocity magnitude of tracer particle ($d_p = 60\ \mu\text{m}$) was smaller than the scalar velocity of the tracer particle ($d_p = 10\ \mu\text{m}$). The velocity of the tracer ($d_p = 60\ \mu\text{m}$) increased on the near bottom surface because the settling velocity influenced the velocity magnitude of the y-component. In this study, $10\ \mu\text{m}$ tracer particle was adopted with respect to the following PIV experiments.

2.4.3 Velocity vector map and profile obtained by PIV technique

In order to classify the flow pattern as a function of Reynolds number, the results of seven fluid flow rates were compared based on the oral inhalation. The velocity values are calculated as scalar velocities by using two velocity components. Figure 2.13(A) shows the PIV results of the seven cases with scalar velocity at line L6 (see figure 2.9). The mean velocities at cross line L6 were normalized by using the outlet velocity as shown in figure 2.13(B) ($U_{y^*}/U_{out}, U_{y^*} = \sqrt{u^2 + v^2}$, u : velocity magnitude of x-component, v : velocity magnitude of y-component). The flow through the passageway was not sufficiently developed in cases involving 4 L/min and 6 L/min of the fluid flow rate. A gradual increase in the value of flow rate to 22 L/min (Re=5161) led to the flow becoming fully developed in the passageway. In the trachea region, the 10 L/min (Re=2346) flow rate was located in the transition zone.

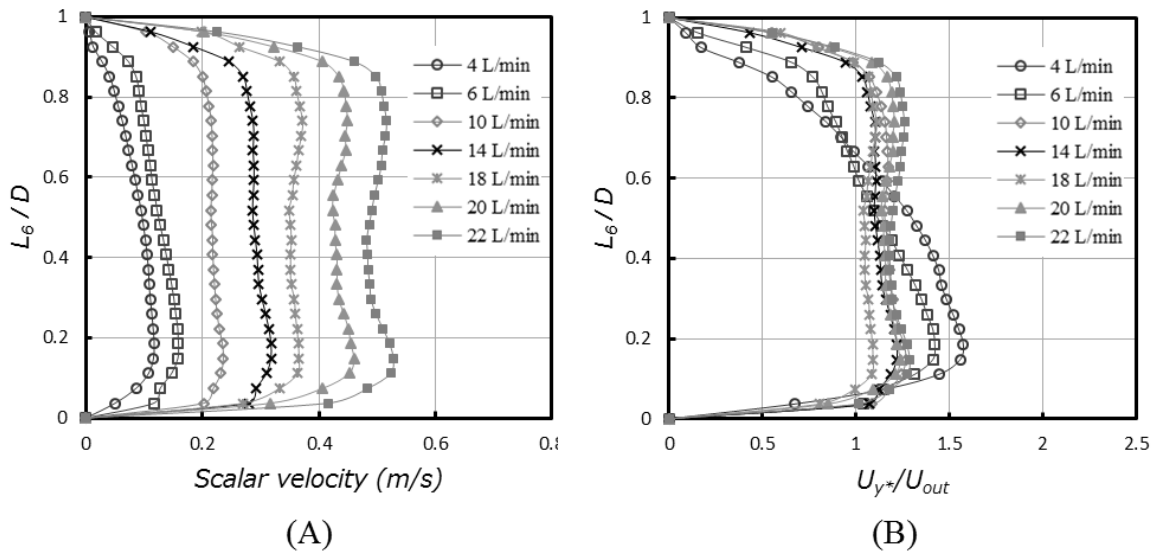


Figure 2.13 Profiles of all conducted experimental result on line L6 (Figure. 2.9) based on the Reynolds number matching under oral inhalation.

2.4.3.1 Velocity map cavity region

Oral inhalation condition

In this study, PIV results divided by cavity and trachea regions were compared in the cases involving fluid flow rates corresponding to 4 L/min, 10 L/min, and 20 L/min. The PIV measurement results of the velocity vectors and velocity distribution of the oral cavity region are shown in figures 2.14 and 2.15, respectively. Figure 2.14 shows the velocity vector map obtained using PIV at cross-section of oral cavity for the flow rates corresponding to (A) 4 L/min, (B) 10 L/min, and (C) 20 L/min. Fig 2.15 shows the two dimensional mean velocity distribution of oral cavity plotted at the vertical cross section A-A' of the mouth entrance center for the flow rates corresponding to (A) 4 L/min, (B) 10 L/min, and (C) 20 L/min. The bottom part of the oral cavity that segued into the trachea presents minute flow fields that appear to be stagnant. Figure 2.16 shows the velocity distribution with velocity vectors of trachea region under oral inhalation condition. The flow is characterized by the region of separated flow at the start of the nasal/oral cavity, pharynx, and larynx and down to trachea. The fluid flow in the oral cavity for the three cases is indicated by a similar flow structure and complicated flow patterns. An angle of the inflow boundary leads to the occurrence of recirculating flow in the vicinity of the mouth opening. In the recirculation zone, back flow and reattachment point is confirmed (see Fig. 2.17).

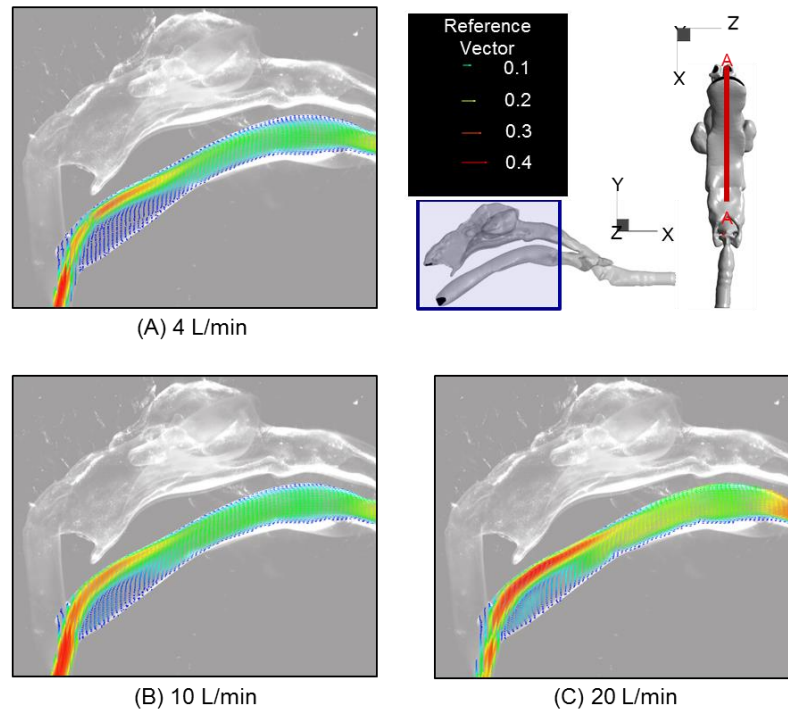


Figure 2.14 The velocity vector map obtained using PIV at cross-section of oral cavity

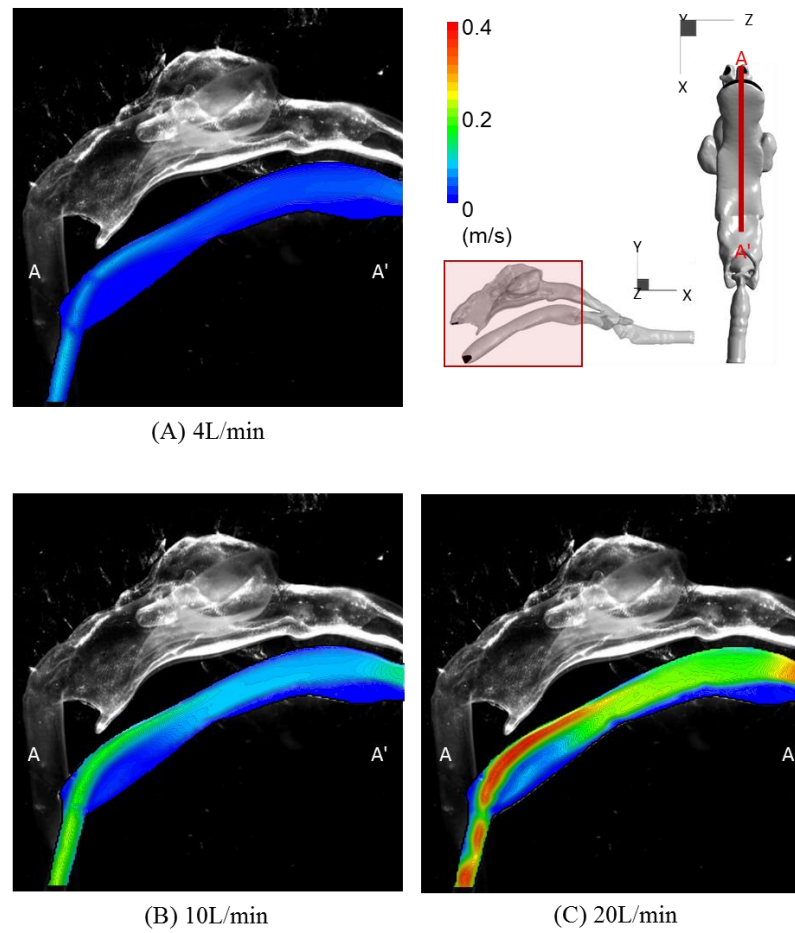


Figure 2.15 The contours of the time averaged velocity distribution obtained using PIV at cross-section of oral cavity

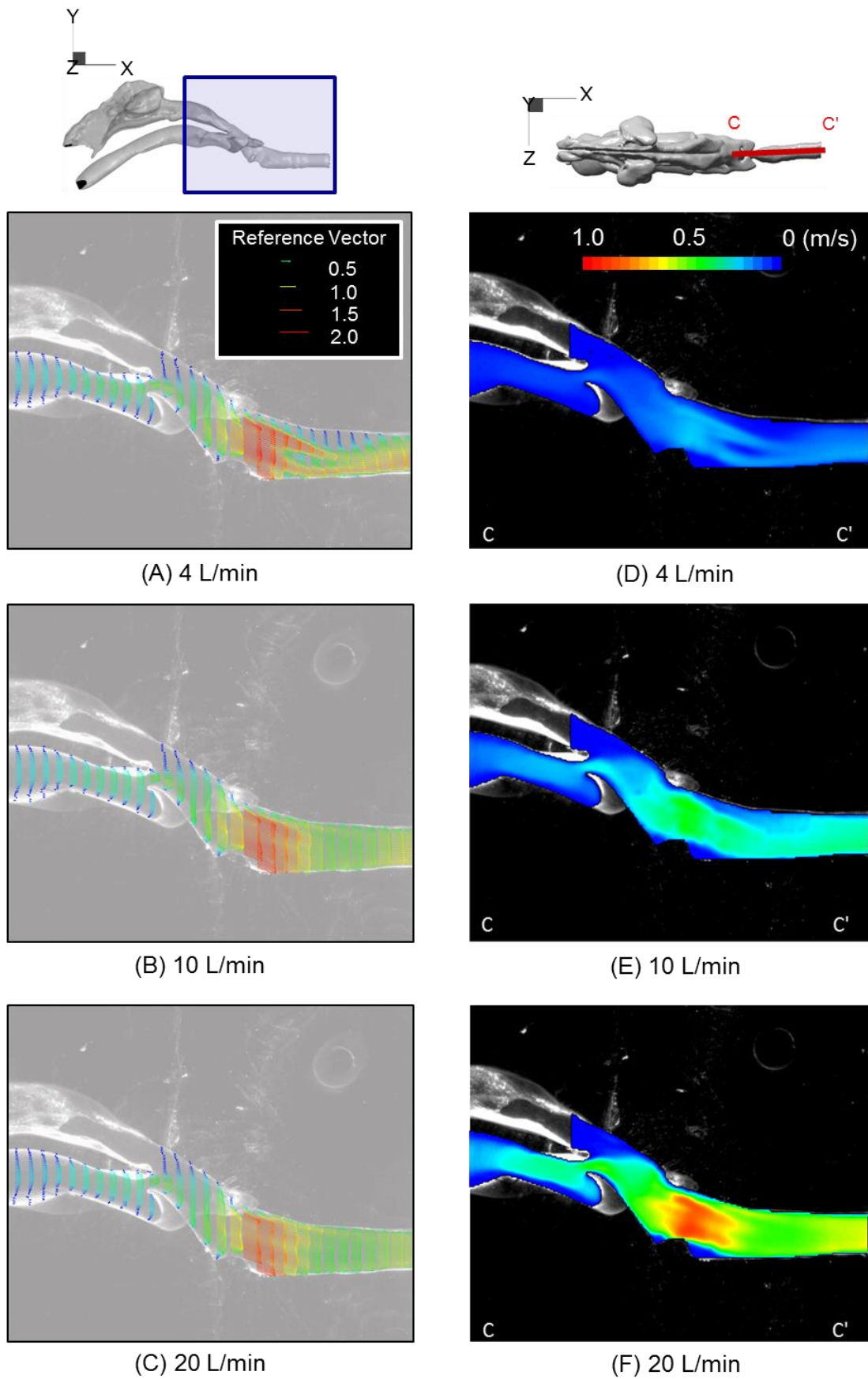
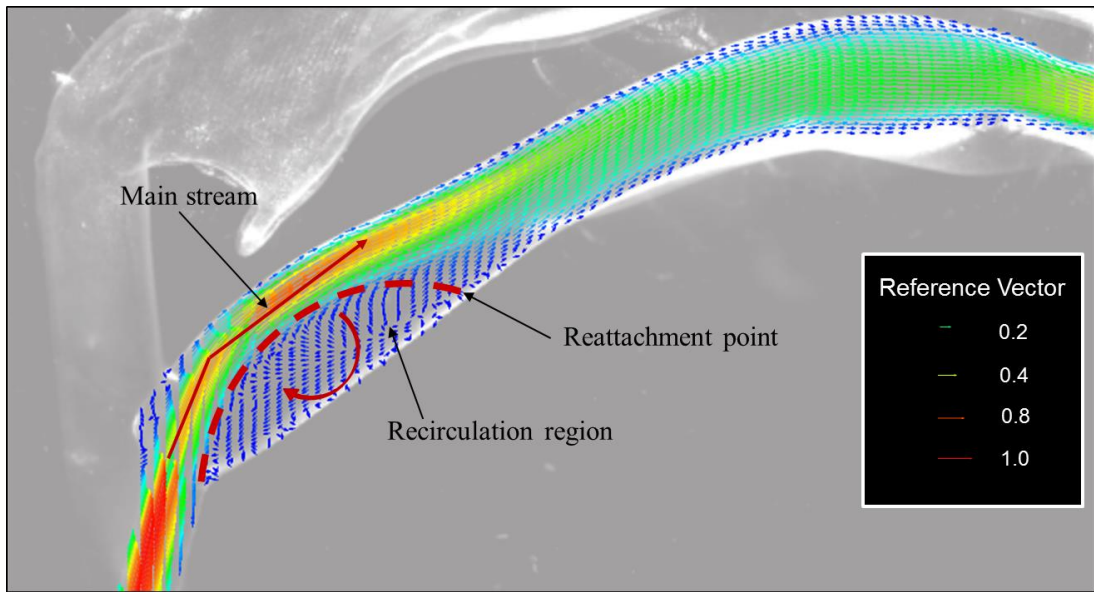
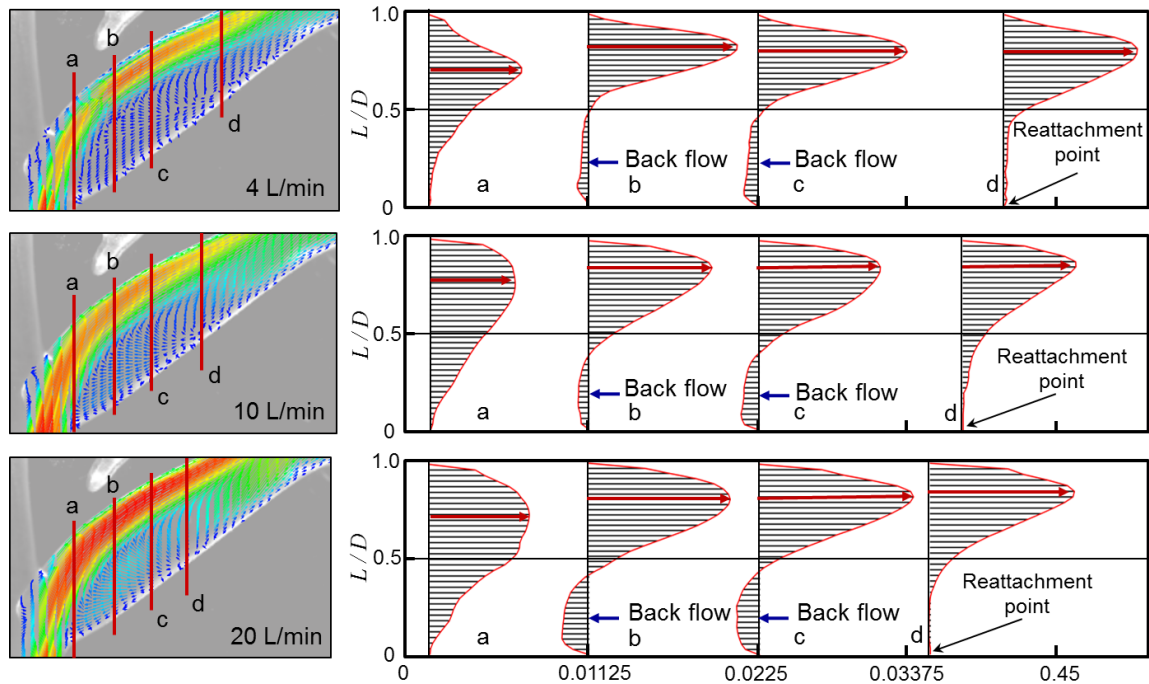


Figure 2.16 Contours of time averaged velocity distribution in the trachea with velocity vectors under oral inhalation condition (Cross-section C-C' : center of trachea region)



(A) The recirculation zone and main stream at cross-section of oral cavity under 4 L/min



(B) Normalized scalar velocity profile and reattachment point

Figure 2.17 The recirculation zone and reattachment point at cross-section of oral cavity

Nasal inhalation condition

The PIV measurement results of the velocity vectors and velocity distribution of the nasal cavity region are shown in figures 2.18 and 2.19, respectively. Figure 2.18 shows contours of time averaged velocity distribution in the left nasal cavity with velocity vectors at cross-section A-A' for the flow rates corresponding to (A) 4 L/min, (B) 10 L/min, and (C) 20 L/min. Figure 2.18 shows contours of time averaged velocity distribution in the right nasal cavity with velocity vectors at cross-section A-A' for the flow rates corresponding to (A) 4 L/min, (B) 10 L/min, and (C) 20 L/min. The velocity distribution under a nasal inhalation condition with velocity vectors of the vertical cross section are plotted on cross section A-A' (left cavity) and B-B' (right cavity) by the center of the nostril. The velocity vectors were scaled to a common reference value to improve the clarity of the results. The PIV results do not indicate the same geometry in the left and right nasal cavities since the shape of nasal cavity is not symmetric. It was not possible to confirm the flow patterns of vicinal maxillary sinus because of the deposition of particles on the wall. However, the flow pattern in the region passing through the oral cavity to the pharynx was reliably obtained. A similar flow structure at the inlet was confirmed despite a difference in shape. The protruding part around the inlet changes the flow pattern abruptly. The velocity is reduced due to the interference of walls with complex shapes. The velocity increases again after the airflow moves into the pharynx area. Figure 2.20 shows the velocity distribution with velocity vectors of trachea region under nasal inhalation condition. The PIV results between oral and nasal inhalation are compared with a scalar velocity distribution of an outlet

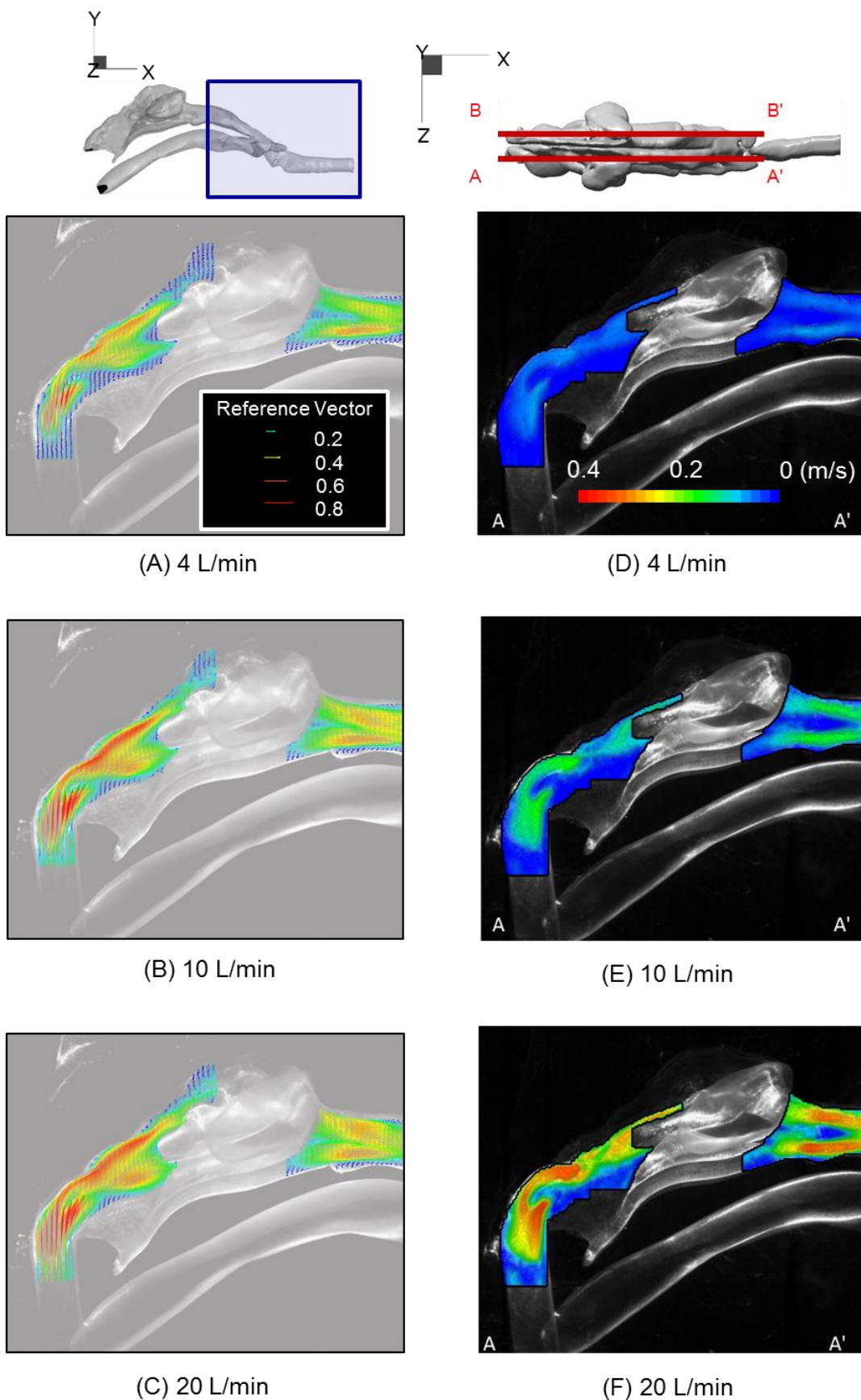


Figure 2.18 Contours of time averaged velocity distribution in the nasal cavity with velocity vectors at cross-section A-A' of left nasal cavity

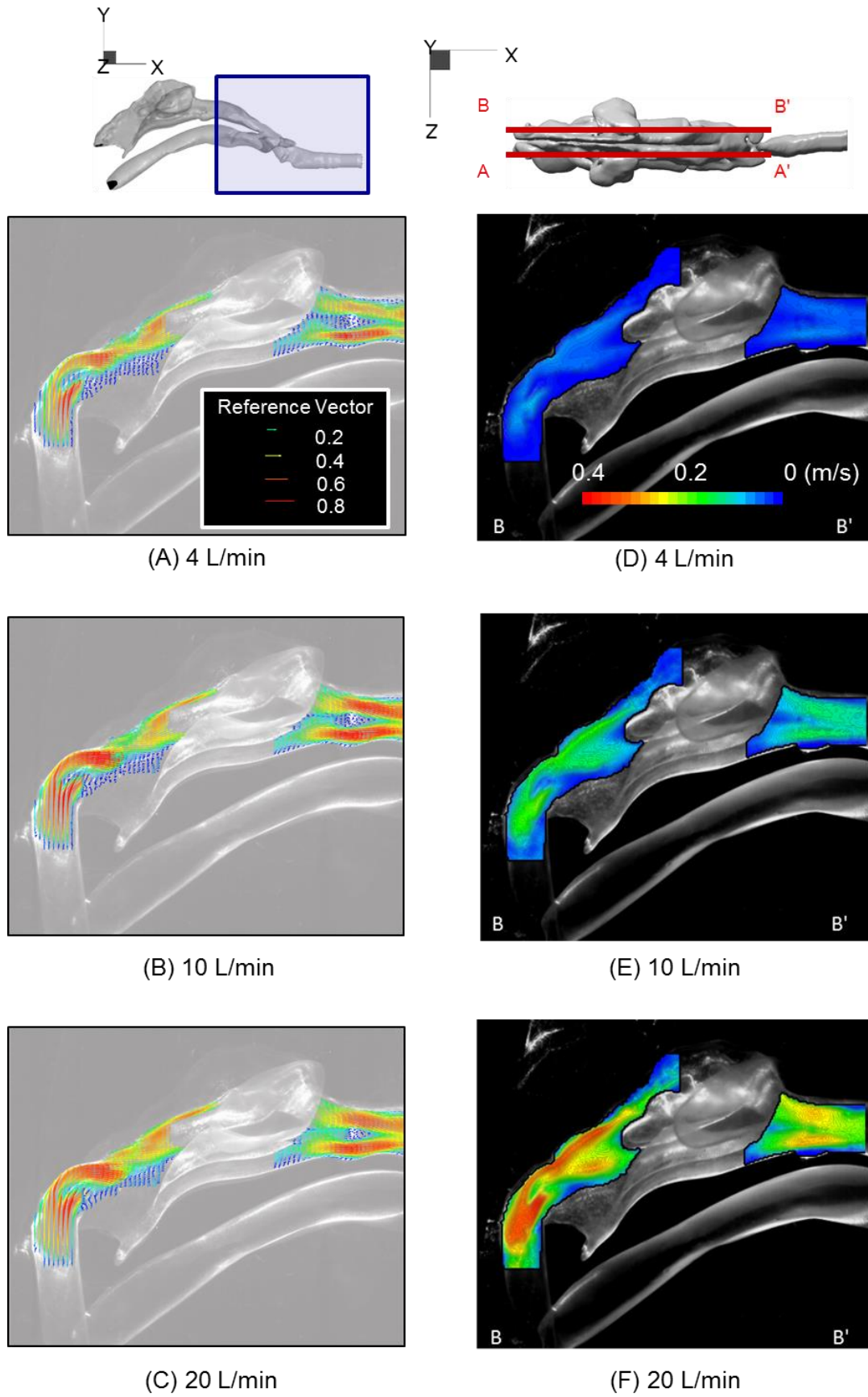


Figure 2.19 Contours of time averaged velocity distribution in the nasal cavity with velocity vectors at cross-section B-B' of right nasal cavity

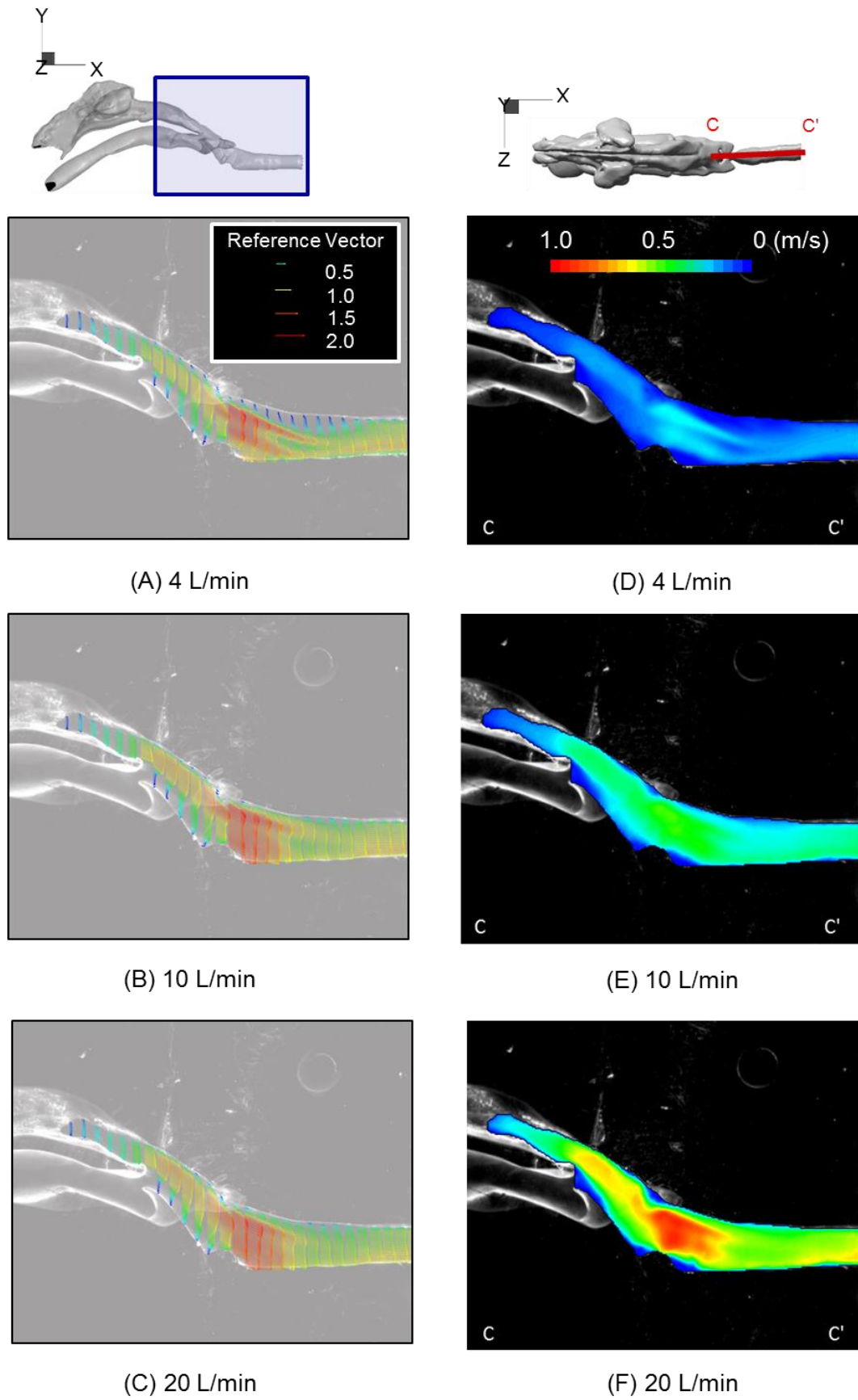
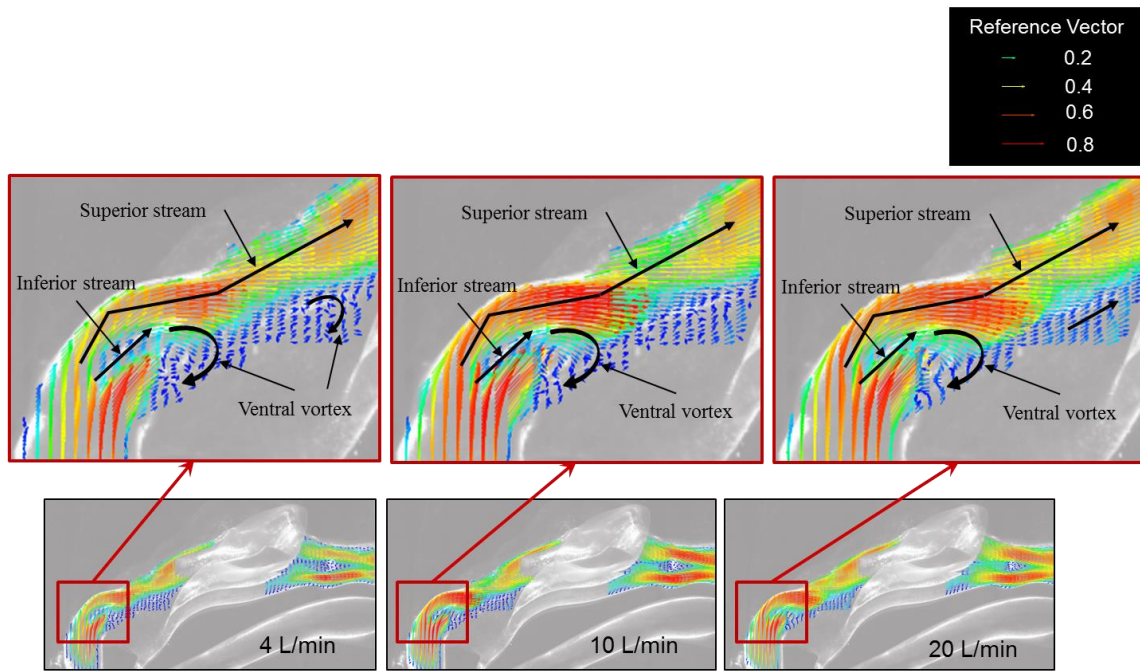
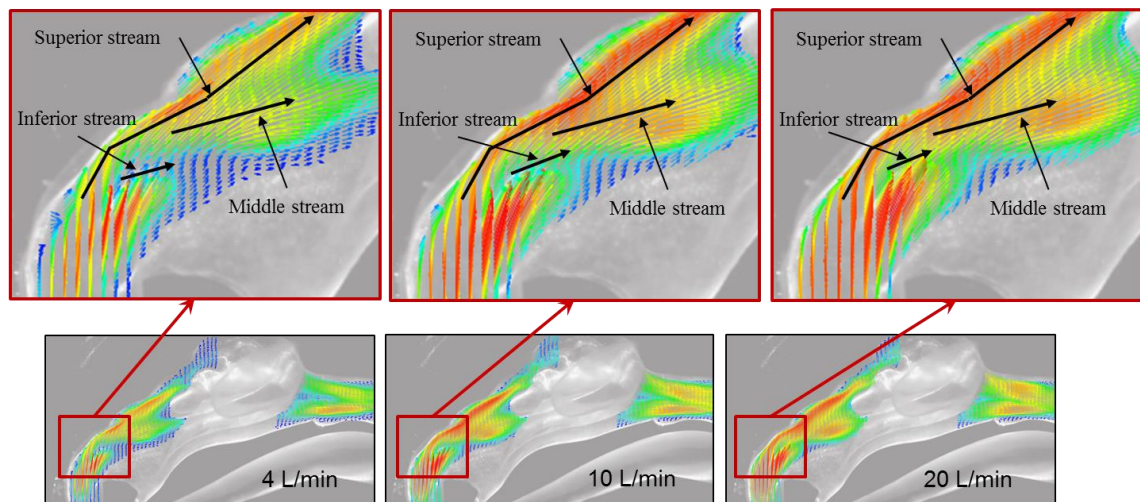


Figure 2.20 Contours of time averaged velocity distribution in the trachea with velocity vectors under nasal inhalation condition (Cross-section C-C' : center of trachea region)



(A) The left nasal cavity under 4, 10 and 20 L/min



(B) The right nasal cavity under 4, 10 and 20 L/min

Figure 2.21 Observed flow structures on nasal vestibule in the monkey nasal airway.

part that possesses the same geometry. The flow of nasal inhalation condition also is characterized by the region of separated flow at the start of the nasal/oral cavity, pharynx, and larynx and down to trachea. The velocity vector plots exhibited a similar flow structure in oral and nasal inhalation for all three flow rates. However, flow structural variations exist due to the

inlet location to access trachea. After the fluid flow passes the converging path of pharynx, the velocity vector increases, and thus flow separation occurred with abrupt geometrical changes from the larynx to trachea.

2.4.3.2 Profile of Oral and Nasal cavities

Profile of oral inhalation condition

In order to compare the profile of three flow rate, the mean velocities at each cross line were normalized by using the outlet velocity ($U_{y^*} / U_{out}, U_{y^*} = \sqrt{u^2 + v^2}$, u : velocity magnitude of x-component, v : velocity magnitude of y-component). Figure 2.20 shows the normalized velocity profiles for the three inspiratory flow rates that are plotted at two cross line locations for oral inhalation. As shown in Figure 2.22A, the normalized scalar velocity profiles of the line L1 indicates that the fluid on the upper (vicinal palate) side moves faster while the fluid on the lower (vicinal tongue) side moves slower. Hence, the deposition is expected to occur at the lower side of trachea with a weak velocity magnitude as shown in Fig 2.22A. Figure 2.22B shows the normalized velocity profiles for the three inspiratory flow rates at two cross line locations in trachea region. The fluid flow corresponding to 4 L/min exhibits a precipitous inclination of the velocity magnitude at the upper sides.

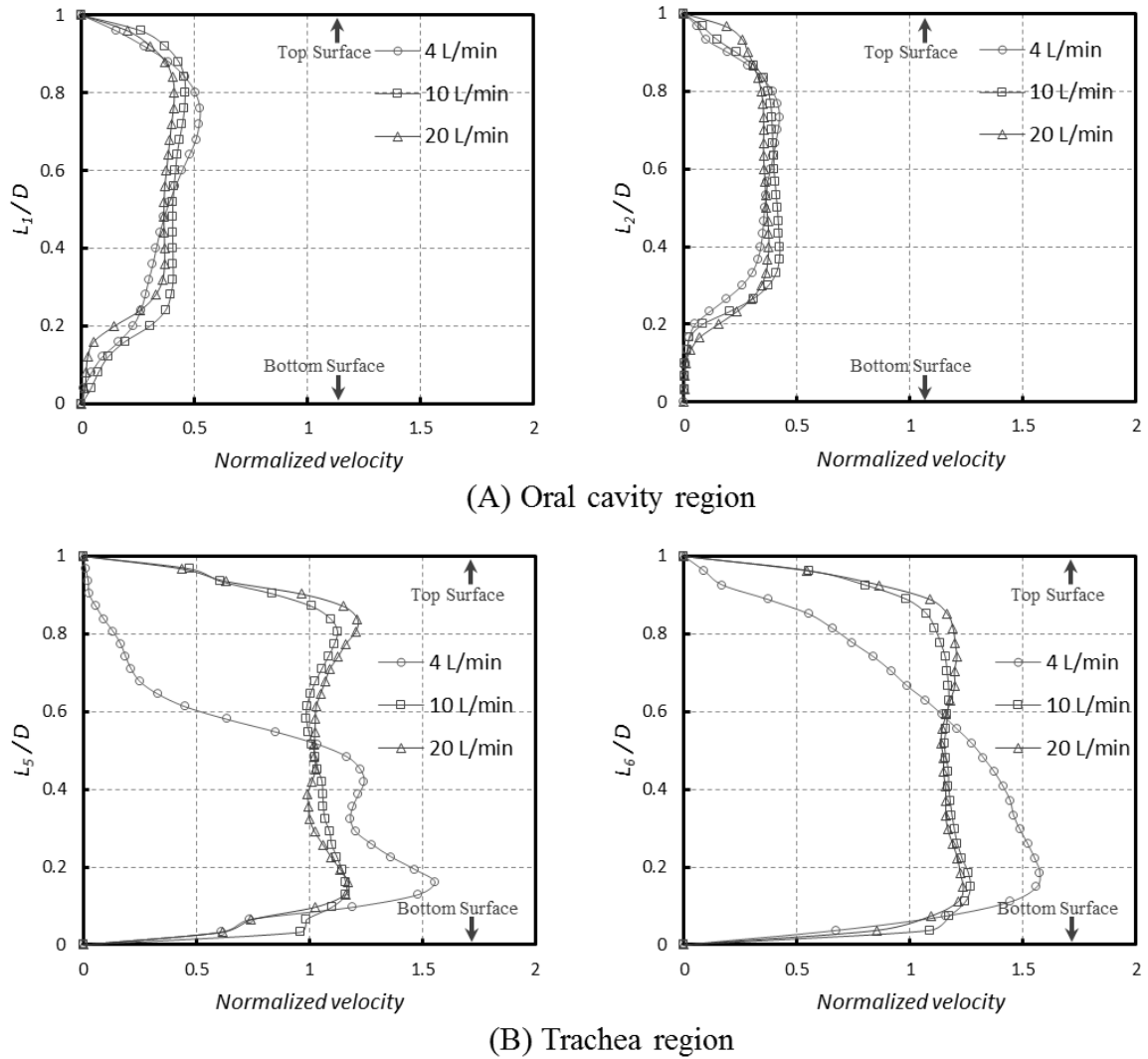
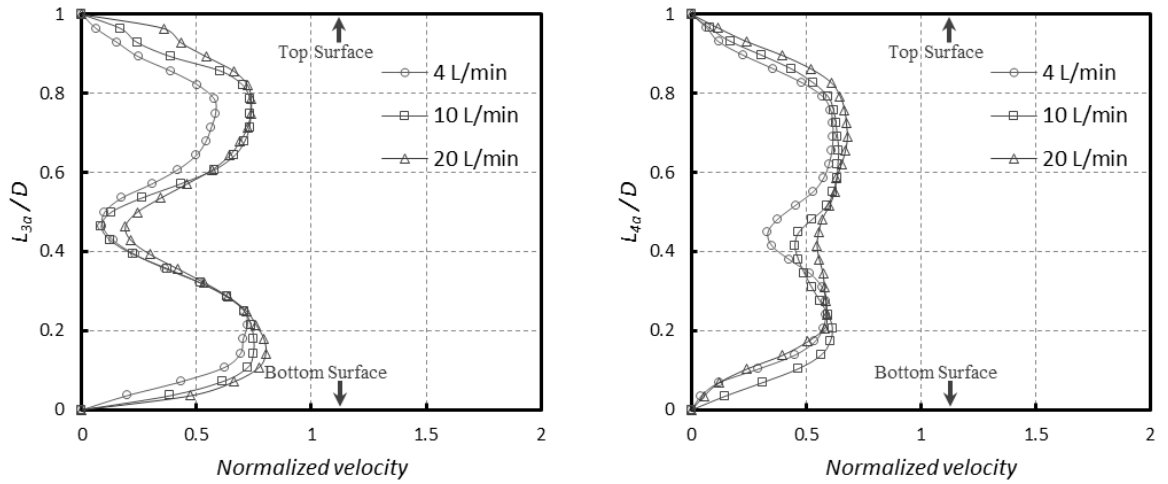


Figure 2.22 Profile of normalized scalar velocity in oral cavity and trachea region under oral inhalation.

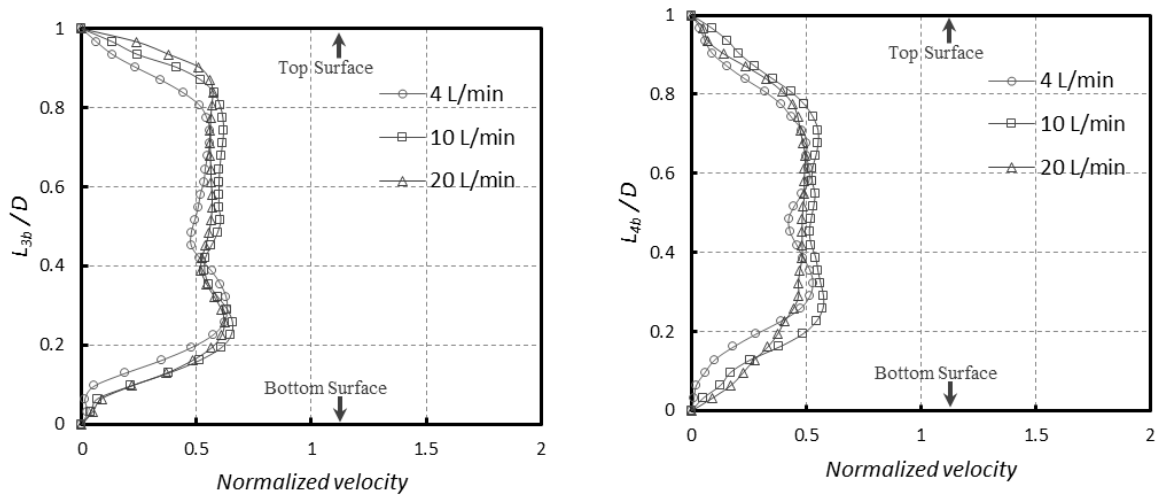
Profile of nasal inhalation condition

The velocity magnitude of the line L2 in figure 2.9 corresponds to a developed convex profile. In the case of line L2, normalized scalar velocities indicate a minute value near the bottom surface. The normalized velocity profiles for the three inspiratory flow rates are plotted at three cross line locations for nasal inhalations as shown in figure 2.9. As described above, the nasal cavity with unequal geometry exhibits different patterns in the flow field. As shown in figure

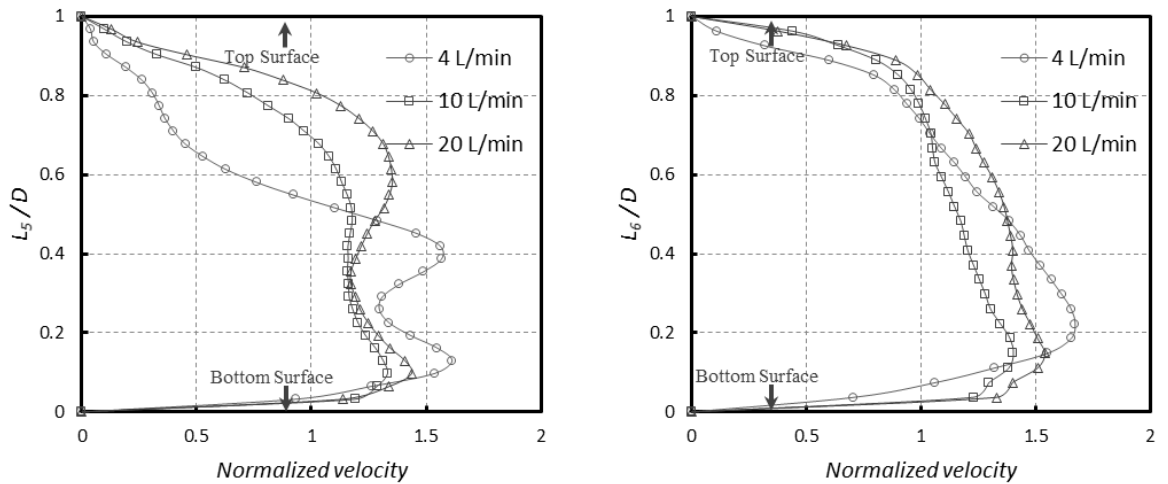
2.23A (left nasal cavity), a pronounced concave curve profile appears as indicated by the protruding portion around the inlet. Figure 2.23C (right nasal cavity) shows unstable profiles that are due to complex shapes. The flow field profile is well developed in the trachea region in the cases involving oral inhalation corresponding to 10 L/min and 20 L/min. In a manner similar to the flow rate corresponding to 4 L/min under an oral inhalation condition, the fluid flows corresponding to 4 L/min under the nasal inhalation condition are represented by unevenly developed flow rates as shown in figure 2.23C(trachea region). The fluid flow from the nasal cavity passes through the top of the larynx at a high velocity. The profiles of flow rates corresponding to 10 L/min and 20 L/min under nasal inhalation condition reveal that the velocity magnitude exhibits a discrepancy between the two flows. The highest velocities in the flow field are achieved at the lower side in the trachea for nasal inhalation. This acceleration is caused by a unique shape, an angle, and a contracting cross-sectional area from the larynx to the trachea region. The results indicate that the velocities on the upper side are smaller when compared to those on the lower side.



(A) Left nasal cavity



(B) Right nasal cavity



(C) Trachea region

Figure 2.23 Profile of normalized scalar velocity in the nasal cavity and trachea under nasal inhalation condition

2.4.4 Conclusion and discussions

2.4.4.1 Conclusion

In this study, a PIV experiment was conducted to investigate the fluid flow pattern of the upper airway of a monkey by using transparent realistic replica model and visualization techniques, and the representative results were reported. This realistic monkey upper airway model was used to investigate flow patterns under three constant inhalation conditions involving the following flow rates: 4 L/min, 10 L/min, and 20 L/min. The target was divided into the cavity and trachea regions. The fluid flow passing through the inlet to the trachea was measured to obtain the characteristic flow mechanisms. The respiratory tract model provided the flow pattern around the inlet and the end of trachea. The phenomenon of flow in the trachea region was confirmed with a characterized flow field. An increasing in the flow rate led to a constant profile of velocity magnitude at the position of upper and lower sides in trachea region. In the oral inhalation scenario, the particle is expected to be deposited on the bottom surface because the case of three flow rates (4 L/min, 10 L/min, and 20 L/min) led to recirculation near the inlet and the end of the oral cavity. It is expected that the results of this chapter will significantly contribute to a validation study for developing an in silicone model and especially with respect to the CFD analysis involved.

2.4.4.2 Discussion

The PIV measurement was limited due to the complex geometry and bias error. It was assumed that the total error in estimating a single displacement vector corresponded to a sum of the bias

error and the measurement uncertainty. Each displacement vector is related with a certain degree of over or underestimation error, i.e., bias error, and a specific degree of random error or measurement uncertainty. Bias errors involve a correlation mapping error and a conversion error resulting from the conversion of the pixel spacing to dimensional measurements. These errors were assumed to be negligible in the measurements performed in this study. Measurement uncertainty was attributed to the collection techniques used for the experimental data. Common sources included variations and uncertainties in the range of particle diameter, flow rates of the working fluid, laser reflections, refractive index, air bubbles, and tracer particle attached on the model surface. The PIV experiment was carefully conducted to reduce experimental error.

In order to determine the kinematic viscosity of working fluid, the efflux time measurement using a Cannon-Fenske routine viscometer was obtained through the average of eight-times measurements. It was assumed that the error in the determination of viscosity of working fluid is related to the efflux time measurement because the efflux time was measured with a stopwatch through naked eye. The efflux time depended on the temperature range and fluctuations of ambient conditions. The 10 μ m mean diameter particle as a tracer consisted typically of a diameter in the order of 2 to 20 μ m. Thus particle size was balanced to scatter enough light to accurately visualize all particles within the laser sheet plane with the assumption that small particle size has weak scattering from a laser sheet. The minimum airway caliber to relate the captured left and right nasal meatus has over 3mm against the laser light sheet. Concerning interrogation area (IA), initial IA starts with 128 \times 128 pixels and decreases

gradually until 8×8 pixels. The side length of 8 pixels did not exceed 36% of the minimum larynx diameter in the captured frame. An average of 10 or more particles per IA was employed in order to maximize PIV algorithm accuracy (Keane, R.D et al., 1992). Also, the particle displacement did not exceed the standard of 25% of the IA length (in our case 22%). The particle size was determined according to minimum passage width of the model at the target region by laser light sheet. The spatial resolution was determined by the maximum spatial separation of captured particle displacement as well as the first interrogation area that had enough pixel size. The PIV experiment in this study was carefully conducted to reduce experimental error. The study involved successfully constructing a rigid and compliant optically transparent model that contained a reproduced detailed geometry of the monkey's upper airway region suitable for flow visualization by PIV experiments.

Reference

- 2-1) Andersen I and Proctor DF. The fate and effects of inhaled materials. In: the nose: Upper
- 2-2) Vardoulakis, S. et al. Impact of climate change on the domestic indoor environment and associated health risks in the UK. *Environ. Int.* 85, 299–313. 2015.
- 2-3) Phuong, N. L. & Ito, K. Investigation of flow pattern in upper human airway including oral and nasal inhalation by PIV and CFD. *Build. Environ.* 94, 504–515. 2015.
- 2-4) Phuong, N. L., Yamashita, M., Yoo, S. J. & Ito, K. Prediction of convective heat transfer coefficient of human upper and lower airway surfaces in steady and unsteady breathing conditions. *Build. Environ.* 100, 172–185. 2016.
- 2-5) Yoo, S.-J. & Ito, K. Numerical prediction of tissue dosimetry in respiratory tract using computer simulated person integrated with physiologically based pharmacokinetic–computational fluid dynamics hybrid analysis. *Indoor Built Environ.* 1420326X1769447. 2017. doi:10.1177/1420326X17694475
- 2-6) Kuga, K. et al. First- and second-hand smoke dispersion analysis from e-cigarettes using a computer-simulated person with a respiratory tract model. *Indoor Built Environ.* 1420326X1769447. 2017. doi:10.1177/1420326x17694476
- 2-7) Ito, K. et al. Prediction of convective heat transfer coefficients for the upper respiratory tracts of rat, dog, monkey, and humans. *Indoor Built Environ.*t. 2016. doi:10.1177/1420326x16662111
- 2-8) Raub, J. a, Mathieu-Nolf, M., Hampson, N. B. & Thom, S. R. Carbon monoxide poisoning - a public health perspective. *Toxicology* 145, 1–14. 2000.
- 2-9) Darby, S. et al. Radon in homes and risk of lung cancer: collaborative analysis of individual data from 13 European case-control studies. *BMJ* 330, 223. 2005.
- 2-10) Chauhan, A. J. & Johnston, S. L. Air pollution and infection in respiratory illness. *Br. Med. Bull.* 68, 95–112. 2003.
- 2-11) Gilmour, M. I., Jaakkola, M. S., London, S. J., Nel, A. E. & Rogers, C. A. How exposure to environmental tobacco smoke, outdoor air pollutants, and increased pollen burdens influences the incidence of asthma. *Environ. Health Perspect.* 114, 627–633. 2006.
- 2-12) Blanc, P. D. et al. Impact of the home indoor environment on adult asthma and rhinitis. *J. Occup. Environ. Med.* 47, 362–372. 2005.
- 2-13) Vermeulen, M. et al. Flow Analysis in Patient Specific Lower Airways Using PIV. *Appl. Laser Tech. to Fluid Mech.* 15th Int. Symp. Proc. 2010.
- 2-14) Adler, K. & Brücker, C. Dynamic flow in a realistic model of the upper human lung airways. *Exp. Fluids* 43, 411–423. 2007.
- 2-15) Report, T. Estimation of human toxicity from animal data (dstl 1987).pdf. 2, 2004.

- 2-16) Schroeter, J. D. et al. Application of physiological computational fluid dynamics models to predict interspecies nasal dosimetry of inhaled acrolein. *Inhal Toxicol* 20, 227–243. 2008.
- 2-17) Corley, R. A. et al. Comparative computational modeling of airflows and vapor dosimetry in the respiratory tracts of rat, monkey, and human. *Toxicol. Sci.* 128, 500–516. 2012.
- 2-18) Corley, R. A. et al. Comparative risks of aldehyde constituents in cigarette smoke using transient computational fluid dynamics/physiologically based pharmacokinetic models of the rat and human respiratory tracts. *Toxicol. Sci.* 146, 65–88. 2015.
- 2-19) Geoghegan, P. H., Buchmann, N. A., Spence, C. J. T., Moore, S. & Jermy, M. Fabrication of rigid and flexible refractive-index-matched flow phantoms for flow visualisation and optical flow measurements. *Exp. Fluids* 52, 1331–1347. 2012.
- 2-20) Westerweel, J., Draad, A. A., van der Hoeven, J. G. T. & van Oord, J. Measurement of fully-developed turbulent pipe flow with digital particle image velocimetry. *Exp. Fluids* 20, 165–177. 1996.
- 2-21) Scarano, F. & Riethmuller, M. L. Iterative multigrid approach in PIV image processing with discrete window offset. *Exp. Fluids* 26, 513–523. 1999.
- 2-22) Hopkins, L. M., Kelly, J. T., Wexler, a. S. & Prasad, a. K. Particle image velocimetry measurements in complex geometries. *Exp. Fluids* 29, 91–95. 2000.
- 2-23) Bai, K. & Katz, J. On the refractive index of sodium iodide solutions for index matching in PIV. *Experiments in Fluids* 55, 2014.
- 2-24) Keane, R.D., Adrian, R.J., Theory of cross-correlation analysis of PIV images. *Appl. Sci. Res.* 49, 191–215. <https://doi.org/10.1007/BF00384623>. 1992.

CHAPTER 3

PRE-PROCESSING FOR CFD SIMULATION IN MONKEY AIRWAY MODEL

3.1 NUMERICAL ANALYSIS OF FLOW FIELD

The mathematical equations and numerical models used for the numerical simulations are described. Computational fluid dynamics (CFD) is a computerized method to predict airflow by using numerical methods and algorithms. In this method, computers are used to perform the numerous calculations needed to simulate the interactions of the fluid itself and its surroundings. CFD is based on the governing equations of fluid dynamics. These equations are mathematical statements of the conservation laws of physics, consisting of a continuity equation, momentum equations and an energy equation which are called the comprehensive Navier-Stokes equation.

3.1.1 Numerical methodology

3.1.1.1 Fundamental numerical analysis

Fluid transport phenomena are defined by the continuity equation of (3-1) and the Navier-Stokes equation of (3-2) for incompressible fluids.

$$\frac{\partial U_i}{\partial x_i} = 0 \dots\dots\dots (3-1)$$

$$\frac{\partial U_i}{\partial t} + U_j \cdot \frac{\partial U_i}{\partial x_j} = -\frac{1}{\rho} \cdot \frac{\partial P}{\partial x_i} + \nu \frac{\partial}{\partial x_j} \left(\frac{\partial U_i}{\partial x_j} + \frac{\partial U_j}{\partial x_i} \right) - g_i \beta \theta \dots\dots\dots (3-2)$$

Where U_i is the component of the flow velocity (u, v, w), ρ is the density of the fluid, P is the pressure, ν is the kinematic viscosity, θ is the temperature (or temperature difference with absolute zero), g is the gravitational acceleration vector and β represents a coefficient of thermal expansion. In the case of a continuous incompressible fluid of the formula (3-1), it is derived from the law of conservation of mass assuming that the density does not change (3-2). The Navier-Stokes equations represent momentum conservation laws, but this expression is derived by Newton's second law and considers the effects of buoyancy.

In the case of a non-isothermal flow field, the temperature field can be expressed by the heat energy transport equation shown in Eq. (3-3).

$$\frac{\partial \theta}{\partial t} + \frac{\partial U_j \theta}{\partial x_j} = \frac{\partial}{\partial x_j} \alpha \frac{\partial \theta}{\partial x_j} + S \dots\dots\dots (3-3)$$

Where α is the heat diffusion coefficient ($=\lambda/C_p \cdot \rho$), and S is the heat source. This heat energy transport equation represents energy conservation law and is derived based on Fourier's law. In the same way as the thermal energy transport equation of the formula (3-3), for the scalar such as moisture and pollutants, the transport phenomenon can be defined by the scalar transportation equation of (3-4).

$$\frac{\partial \phi}{\partial t} + \frac{\partial U_j \phi}{\partial x_j} = \frac{\partial}{\partial x_j} D \frac{\partial \phi}{\partial x_j} + S' \dots\dots\dots (3-4)$$

Where ϕ is the scalar quantity of moisture and contaminants and D is the diffusion coefficient of the substance. The incompressible fluid and scalar transport phenomena can be understood using coupled analysis between equation (3-1) and (3-4).

3.1.1.2 Non-dimensionalization for Navier-Stokes equation

From equation (3-1), equation (3-4) is non-dimensionalized. When the Navier-Stokes equation shown in Eq. (3-2) is non-dimensionalized. Equation (3-5) can be expressed by the non-dimensionalization using the representative length L_0 (the size of the inflow interface) and the representative velocity U_0 (inflow velocity).

$$\frac{\partial U_i^*}{\partial t^*} + U_j^* \cdot \frac{\partial U_i^*}{\partial x_j^*} = -\frac{\partial P^*}{\partial x_i^*} + \frac{1}{\text{Re}} \cdot \frac{\partial}{\partial x_j^*} \left(\frac{\partial U_i^*}{\partial x_j^*} + \frac{\partial U_j^*}{\partial x_i^*} \right) - \text{Ar} \dots\dots\dots (3-5)$$

Where the subscript * is a dimensionless quantity and can be expressed $U_i^* = U_i/U_0$, $x_i^* = x_i/L_0$, $t^* = t/t_0 = t/(L_0/U_0)$, $P^* = P/P_0 = P/U_0^2$, respectively. The Reynolds number and Archimedes number are defined as parameters that govern the similarity of the flow field and the temperature field, as shown in equations (3-6) and (3-7).

$$\text{Re} = \frac{U_0 L_0}{\nu} \dots\dots\dots (3-6)$$

$$\text{Ar} = \frac{g_i \cdot \beta \cdot \theta \cdot L_0}{U_0^2} \dots\dots\dots (3-7)$$

Equation (3-6) and (3-7) is a dimensionless parameter called Reynolds number (Re) and Archimedes number (Ar). Regarding the relationship between the Re and the Ar in Equation

(3-5), it can be expected that the flow properties will be the same in each flow field in case of that the Re is equal to the Ar. In the equation (3-5), the diffusion term decreases as the Re increases and the instability of the flow increases because the convection term becomes relatively large. Also, if the Re is large enough, the diffusion term will be negligible decreased relative to the convection term and the Re at this time is called the Critical Reynolds number.

The heat energy transport equation shown in equation (2-3) can also be dimensionless as shown in the following equation.

$$\frac{\partial \theta^*}{\partial t^*} + \frac{\partial U_j^* \theta^*}{\partial x_j^*} = \frac{\partial}{\partial x_j^*} \left(\frac{1}{\text{Re}} \cdot \frac{1}{\text{Pr}} \cdot \frac{\partial \theta^*}{\partial x_j^*} \right) + S^* \dots\dots\dots (3-8)$$

Where θ^* is expressed θ/T_0 , Pr is a dimensionless number representing the ratio of thermal diffusion coefficient $\alpha(=\lambda/C_p \cdot \rho)$ to the diffusion coefficient of molecules ν and is called Prandtl Number.

$$\text{Pr} = \frac{\nu}{\alpha} \dots\dots\dots (3-9)$$

The following equation can be derived by non-dimensionalization of the transport equation of scalar, shown in equation (3-4).

$$\frac{\partial \phi^*}{\partial t^*} + \frac{\partial U_j^* \phi^*}{\partial x_j^*} = \frac{\partial}{\partial x_j^*} \left(\frac{1}{\text{Re}} \cdot \frac{1}{\text{Sc}} \cdot \frac{\partial \phi^*}{\partial x_j^*} \right) + S^* \dots\dots\dots (3-10)$$

Where ϕ^* is ϕ/ϕ_0 , Sc is a dimensionless number representing the ratio of the diffusion coefficient of material D to the diffusion coefficient of molecules ν and is called the Schmitt Number.

$$Sc = \frac{\nu}{D} \dots\dots\dots (3-11)$$

When the value of $Re \times Sc$ is the same in equation (3-10), the distribution properties of the scalar quantity are similar. When the Re is sufficiently large, since the effect of the diffusion term is relatively smaller than the convection term, the distribution properties of the scalar quantity are similar also as equation (3-5),

3.1.1.3 Reynolds (Ensemble) Averaging

From equation (3-1), the instantaneous values are separated by the average and fluctuation quantity in the equation (3-3), and then the ensemble average is expressed as shown as the equation (3-12), (3-13) and (3-14).

$$\frac{\partial \bar{U}_i}{\partial x_i} = 0 \dots\dots\dots (3-12)$$

$$\frac{\partial \bar{U}_i}{\partial t} + \bar{U}_j \cdot \frac{\partial \bar{U}_i}{\partial x_j} = -\frac{1}{\rho} \cdot \frac{\partial \bar{P}}{\partial x_i} + \nu \frac{\partial}{\partial x_j} \left(\frac{\partial \bar{U}_i}{\partial x_j} + \frac{\partial \bar{U}_j}{\partial x_i} \right) - \frac{\partial}{\partial x_j} \overline{u_i' u_j'} - g_i \beta \bar{\theta} \dots\dots\dots (3-13)$$

$$\frac{\partial \bar{\theta}}{\partial t} + \frac{\partial \bar{U}_j \bar{\theta}}{\partial x_j} = \frac{\partial}{\partial x_j} \alpha \frac{\partial \bar{\theta}}{\partial x_j} + \frac{\partial}{\partial x_j} \overline{u_j' \theta'} \dots\dots\dots (3-14)$$

Where U_i , P , θ is the average quantity, u_i' , θ' represent the quantity variation, The over line means the ensemble average.

The equation (2-13) is called the Reynolds equation. Also, $\overline{u_i' u_j'}$ on the right side of the equation (2-13) is the Reynolds stress, and $\overline{u_j' \theta'}$ on the right side of the equation (2-16) is the temperature flux. In generally, the definition of Reynolds stress is expressed $\rho \times \overline{u_i' u_j'}$, but here,

it is represented only as by simplification. The equation (3-14) is expressed by the average quantity except Reynolds stress and temperature flux from the equation (3-12). Therefore, it is necessary to complete the equation by modeling these two variables as the average quantity. The gradient diffusion approximation and the eddy viscosity model for Reynolds stress will be described later.

3.1.2 Selection of turbulence model

This section describes the standard k- ϵ model of the Reynolds Averaged Navier-Stokes (RANS) model. The low Reynolds number type k- ϵ turbulent model is described.

3.1.2.1 The standard k- ϵ model

It is necessary to close the Reynolds stress term in the correlation term related to the fluctuation velocity with an average quantity. Therefore, Reynolds stress is proportional to the average velocity gradient. Therefore, we assume that the Reynolds stress is proportional to the mean velocity gradient and use the Eddy Viscosity Model, shown in equation (3-15).

$$-\overline{u_i u_j} = \nu_t \left(\frac{\partial \overline{U}_i}{\partial x_j} + \frac{\partial \overline{U}_j}{\partial x_i} \right) - \frac{2}{3} k \delta_{ij} \dots \dots \dots (3-15)$$

Reynolds Stress is calculated by calculation of eddy viscosity coefficient ν_t . The eddy viscosity coefficient ν_t is defined using the turbulent kinetic energy k and the dissipation rate ϵ of the turbulent energy in the standard k- ϵ type turbulence model. k and ϵ is calculated by

solving the transport equation. When ν_t is expressed using k and ε , the following expression is obtained.

$$\nu_t = C_\mu \frac{k^2}{\varepsilon} \dots\dots\dots (3-16)$$

Here, C_μ generally uses the value of $C_\mu = 0.09$ proposed by Spalding and Launder et al. A kinematic equation relating to the fluctuation velocity is derived by subtracting the Reynolds equation of the equation (3-13) from the Navier-Stokes equation of the equation (3-2). Furthermore, when the equation is multiplied by the fluctuation component u_i' , the ensemble average is carried out and when it is sorted out using the turbulent kinetic energy $k = \overline{u_i' u_j'} / 2$, the following equation is obtained.

$$\begin{aligned} & \frac{\partial k}{\partial t} + \overline{U_j} \frac{\partial k}{\partial x_j} + \overline{u_i' u_j'} \frac{\partial \overline{U_i}}{\partial x_j} + \frac{\partial}{\partial x_j} \overline{u_j' k} \\ &= -\frac{1}{\rho} \cdot \frac{\partial}{\partial x_j} \cdot \overline{u_j' p} + \nu \frac{\partial}{\partial x_j} \cdot \overline{u_i' \left(\frac{\partial u_i'}{\partial x_j} + \frac{\partial u_j'}{\partial x_i} \right)} - \nu \cdot \overline{\left(\frac{\partial u_i'}{\partial x_j} + \frac{\partial u_j'}{\partial x_i} \right) \frac{\partial u_i'}{\partial x_j}} \dots\dots\dots (3-17) \end{aligned}$$

The equation given by equation (3-17) is the transport equation of exact turbulence energy k . By simplifying this equation, the transport equation about k is derived as follows. First, the second term on the right-hand side (k transport by molecular diffusion) and the third term on the right-hand side (the ratio of k to thermal energy due to molecular viscosity = viscous dissipation rate) are expressed as follows,

$$\begin{aligned}
 & \nu \frac{\partial}{\partial x_j} \cdot \overline{u_i \left(\frac{\partial u_i}{\partial x_j} + \frac{\partial u_j}{\partial x_i} \right)} - \nu \cdot \overline{\left(\frac{\partial u_i}{\partial x_j} + \frac{\partial u_j}{\partial x_i} \right) \frac{\partial u_i}{\partial x_j}} \\
 &= \nu \frac{\partial^2 k}{\partial x_j^2} + \nu \overline{\left(\frac{\partial u_i}{\partial x_j} \cdot \frac{\partial u_j}{\partial x_i} \right)} + \nu \overline{\left(u_i \frac{\partial}{\partial x_j} \left(\frac{\partial u_j}{\partial x_i} \right) \right)} - \nu \overline{\left(\frac{\partial u_i}{\partial x_j} \cdot \frac{\partial u_i}{\partial x_j} \right)} - \nu \overline{\left(\frac{\partial u_j}{\partial x_i} \cdot \frac{\partial u_j}{\partial x_i} \right)} \\
 &= \nu \frac{\partial^2 k}{\partial x_j^2} - \nu \cdot \overline{\frac{\partial u_i}{\partial x_j} \cdot \frac{\partial u_i}{\partial x_j}} \dots \dots \dots (3-18)
 \end{aligned}$$

The second term on the right side of the equation (3-18) is a definition equation of the dissipation rate ε of the turbulent kinetic energy. The turbulent energy dissipation rate can be expressed using the turbulence velocity U_t and the turbulence length scale A and is shown in the following equation.

$$\varepsilon = C \cdot \frac{U_t^3}{\ell} = C_\mu \frac{k^{3/2}}{\ell} \dots \dots \dots (3-19)$$

Where C is a proportional constant. If it is possible to predetermine its spatial distribution with respect to the length scale, it is unnecessary to solve the transport equation for ε , and the equation system defined by $\nu_t = k^{1/2} \cdot \ell$ can be closed. A model that calculates only the transport equation of k is called a one-equation turbulence model.

When the third term on the left side (production of k by Reynolds Stress) is expressed using the eddy viscosity coefficient ν_t in the equation (3-15), the following equation is obtained.

$$\begin{aligned}
 -\overline{u_i u_j} \frac{\partial \overline{U}_i}{\partial x_j} &= \nu_t \left(\frac{\partial \overline{U}_i}{\partial x_j} + \frac{\partial \overline{U}_j}{\partial x_i} \right) \frac{\partial \overline{U}_i}{\partial x_j} - \frac{2}{3} k \delta_{ij} \frac{\partial \overline{U}_i}{\partial x_j} \\
 &= \nu_t \left(\frac{\partial \overline{U}_i}{\partial x_j} + \frac{\partial \overline{U}_j}{\partial x_i} \right) \frac{\partial \overline{U}_i}{\partial x_j} \dots \dots \dots (3-20)
 \end{aligned}$$

Regarding the fourth term on the left side (transport by turbulent diffusion of k) and the first term on the right side (redistribution between direction components of k due to pressure fluctuation), approximate the gradient diffusion by rearranging them.

$$\frac{\partial}{\partial x_j} \overline{u_j k} + \frac{1}{\rho} \frac{\partial}{\partial x_j} \overline{u_j p} = \frac{\partial}{\partial x_j} \left(-\frac{v_t}{\sigma_k} \cdot \frac{\partial k}{\partial x_j} \right) \dots \dots \dots (3-21)$$

Here, σ_k uses the value of $\sigma_k = 1.0$ proposed by Spalding and Launder et al. By rearranging the above equations, the transport equation of the turbulent kinetic energy k is derived.

$$\frac{\partial k}{\partial t} + \overline{U_j} \frac{\partial k}{\partial x_j} = \frac{\partial}{\partial x_j} \left(\left(\nu + \frac{v_t}{\sigma_k} \right) \frac{\partial k}{\partial x_j} \right) + v_t \left(\frac{\partial \overline{U_i}}{\partial x_j} + \frac{\partial \overline{U_j}}{\partial x_i} \right) \frac{\partial \overline{U_i}}{\partial x_j} - \varepsilon \dots \dots \dots (3-22)$$

(1) (2) (3) (4) (5)

The terms (1)-(5) in Equation (3.22), the turbulent kinetic energy k transport equation, can be interpreted as the following:

- | | | |
|-----|---------------------|--|
| (1) | Transient term | Rate of increase of k |
| (2) | Convection term | Transport of k by convection |
| (3) | Diffusion term | Diffusive transport of k by pressure, viscous stresses, and Reynolds stresses (must be modelled) |
| (4) | Production term | Rate of production of k due from the mean flow |
| (5) | Viscous dissipation | Rate of viscous dissipation of k (must be modelled) |

Here, σ_k is a constant (turbulent Schmidt number) of the k equation

In order to derive the transport equation of the dissipation rate ε , the equation of motion relating

to the speed variation is obtained by subtracting the Reynolds equation of the equation (3-13) from the Navier-Stokes equation of the equation (3-2). Also, after differentiating the equation with x_k , multiplying each term on both sides by $2\nu(\partial u_i / \partial x_k)$ and performing an ensemble average gives the following equation.

$$\begin{aligned} \frac{\partial \varepsilon}{\partial t} + \overline{U_j} \frac{\partial \varepsilon}{\partial x_j} = & \\ & -2\nu \frac{\partial^2 \overline{U_i}}{\partial x_k \partial x_j} \cdot \overline{u_j' \frac{\partial u_i'}{\partial x_k}} - 2\nu \frac{\partial \overline{U_i}}{\partial x_j} \left\{ \overline{\frac{\partial u_i'}{\partial x_k} \cdot \frac{\partial u_j'}{\partial x_k}} + \overline{\frac{\partial u_k'}{\partial x_i} \cdot \frac{\partial u_i'}{\partial x_j}} \right\} \\ & -2\nu \left(\overline{\frac{\partial u_i'}{\partial x_k} \cdot \frac{\partial u_j'}{\partial x_k} \cdot \frac{\partial u_i'}{\partial x_j}} \right) - \frac{\partial}{\partial x_j} \cdot \overline{u_j' \varepsilon'} - \frac{2\nu}{\rho} \cdot \frac{\partial}{\partial x_i} \left(\overline{\frac{\partial u_i'}{\partial x_k} \cdot \frac{\partial p}{\partial x_k}} \right) + \nu \frac{\partial^2 \varepsilon}{\partial x_j^2} - 2\nu^2 \left(\overline{\frac{\partial u_i'}{\partial x_j \partial x_k}} \right)^2 \end{aligned}$$

Here, $\varepsilon' = \nu \frac{\partial u_i'}{\partial x_j} \cdot \frac{\partial u_i'}{\partial x_j}$ (3-23)

In this case, modeling is performed by approximating each term of the equation (3-23), but the diffusion of turbulence mainly occurs from velocity fluctuations including large energy, so using k and ε is reasonable to calculate the diffusion scale of turbulence. In addition, this method is the basic premise of the k - ε type two-equation model. In this case, modeling is performed by approximating each term of the equation (3-23). Since diffusion of turbulence is mainly caused by velocity fluctuations including large energy, it is reasonable to calculate the diffusion scale of turbulence using k and ε . By expressing the length scale of turbulence $\ell = k^{3/2} / \varepsilon$, the time scale of turbulence $t = k / \varepsilon$, and the speed scale of turbulence $u = k^{1/2}$, we can use the above to model the fourth term(diffusion term of ε due to velocity fluctuation) on the right side of

equation (2-25) and the fifth term(diffusion term of ε due to pressure fluctuation) on the right side. The following equation is obtained.

$$\begin{aligned}
 & -\frac{\partial}{\partial x_j} \overline{u_j \varepsilon} - \frac{2\nu}{\rho} \cdot \frac{\partial}{\partial x_i} \cdot \frac{\partial \overline{u_i}}{\partial x_k} \cdot \frac{\partial p}{\partial x_k} = \frac{\partial}{\partial x_i} \left\{ -\overline{u_j \varepsilon} - \frac{2\nu}{\rho} \cdot \frac{\partial \overline{u_i}}{\partial x_k} \cdot \frac{\partial p}{\partial x_k} \right\} \\
 & = \frac{\partial}{\partial x_i} \left\{ C_\varepsilon \left(\frac{\ell^2}{t} \right) \frac{\partial \varepsilon}{\partial x_i} \right\} = \frac{\partial}{\partial x_i} \left\{ C_\varepsilon \frac{k^2}{\varepsilon} \cdot \frac{\partial \varepsilon}{\partial x_i} \right\} = \frac{\partial}{\partial x_i} \left\{ \frac{\nu_t}{\sigma_\varepsilon} \cdot \frac{\partial \varepsilon}{\partial x_i} \right\} \dots\dots\dots (3-24)
 \end{aligned}$$

In the equation (3-24), $C_\varepsilon \cdot k^2/\varepsilon$ is an isotropic scalar quantity irrespective of the direction of flow, hence it is called an isotropic diffusion model.

In the equation (3-23), the production terms of ε is the first term on the right side and the second term on the right side. But comparing the production term of the first term on the right side with the dissipation term of the third term on the right side, the dissipation term is considered to be sufficiently large in usually. Regarding the production term of the second term on the right side, when $i \neq j$, it becomes 0 from the process of isotropic dissipation, and in the case of $i=j$, it becomes 0 from the continuous equation (3-1) as well. Therefore, the production term of ε is ignored with modeling. Further, the dissipation term indicating dissipation of ε is two terms of the third term on the right side and the seventh term on the right side. These dissipation terms are modeled as follows, assuming that the production term (P_k) of k in the transport equation of k is balanced with the dissipation term (ε) of k from the process of local equilibrium.

$$\begin{aligned}
 & -2\nu \left(\frac{\partial u'_i}{\partial x_k} \cdot \frac{\partial u'_j}{\partial x_k} \cdot \frac{\partial u'_i}{\partial x_j} \right) - 2\nu^2 \cdot \left(\frac{\partial^2 u'_i}{\partial x_j \partial x_k} \right)^2 = \frac{\varepsilon}{k} (C_{\varepsilon 1} \cdot P_k - C_{\varepsilon 2} \cdot \varepsilon) \\
 & = C_{\varepsilon 1} \frac{\varepsilon}{k} \cdot \overline{u'_i u'_k} \cdot \frac{\partial \overline{U}_i}{\partial x_k} - C_{\varepsilon 2} \frac{\varepsilon^2}{k} \dots\dots\dots (3-25)
 \end{aligned}$$

In summary, the transport equation for ε is given by the following equation.

$$\begin{aligned}
 & \frac{\partial \varepsilon}{\partial t} + \overline{U}_j \frac{\partial \varepsilon}{\partial x_j} = \\
 & \frac{\partial}{\partial x_j} \left(\left(\nu + \frac{\nu_t}{\sigma_\varepsilon} \right) \frac{\partial \varepsilon}{\partial x_j} \right) + C_{\varepsilon 1} \frac{\varepsilon}{k} \left\{ \nu_t \left(\frac{\partial \overline{U}_i}{\partial x_j} + \frac{\partial \overline{U}_j}{\partial x_i} \right) \cdot \frac{\partial \overline{U}_i}{\partial x_j} \right\} - C_{\varepsilon 2} \frac{\varepsilon^2}{k} \dots\dots\dots (3-26) \\
 & \qquad \qquad \qquad (3) \qquad \qquad \qquad (4) \qquad \qquad \qquad (5)
 \end{aligned}$$

Similar to the transport equation for k , the transport equation for ε includes the terms (1)-(5):

- (1) Rate of increase of ε ,
- (2) Convection term of ε .
- (3) Diffusion term of ε ,
- (4) Rate of production of ε , and
- (5) Rate of destruction of ε ,

Where, $C_{\varepsilon 1} = 1.44$, $C_{\varepsilon 2} = 1.92$, $\sigma_\varepsilon = 1.3$ have been proposed by Spalding and Launder et al.

By solving the transport equation of the turbulent kinetic energy k indicated by the equation (3-20) and the transport equation of the dissipation rate ε , the eddy viscosity coefficient ν_t is calculated from the equation (3-22). It is also possible to calculate Reynolds Stress from equation (3-15). This completes the ensemble-averaged Navier-Stokes equation shown in the

equation (3-13). The standard $k - \varepsilon$ model is summarized and shown in Table 2-1.

The standard $k - \varepsilon$ model described about an isotropic flow field that has Reynolds number large scale. So it is difficult to estimate the area within the viscous sub-layer near the wall surface, the strong anisotropic flow field, etc. in case of low Reynolds number. Analysis using the standard $k - \varepsilon$ model generally does not analyze the region near the wall surface where the influence of viscosity is large, the wall boundary condition is set assuming the wall rule showing the relationship between the wall surface and the first cell. As an example of the adhesion boundary layer, it is shown that sufficient analysis accuracy is secured by using wall functions such as log law, power law, etc., which have been proposed in the past. Because the temperature boundary layer accompanying adhesion, collision, reattachment and heat transfer generated in the vicinity of the wall surface becomes a problem, there is a problem in performing analysis using a universal function. The low Reynolds type $k-\varepsilon$ model was developed to improve the weak point of such a standard $k - \varepsilon$ model.

Table 3.1 The fundamental equations of standard k- ε model (flow field only)

$$\frac{\partial \bar{U}_i}{\partial t} + \bar{U}_j \cdot \frac{\partial \bar{U}_i}{\partial x_j} = -\frac{1}{\rho} \cdot \frac{\partial \bar{P}}{\partial x_i} + \nu \frac{\partial}{\partial x_j} \left(\frac{\partial \bar{U}_i}{\partial x_j} + \frac{\partial \bar{U}_j}{\partial x_i} \right) - \frac{\partial}{\partial x_j} \overline{u_i u_j} \dots\dots\dots (3-27)$$

$$-\overline{u_i u_j} = \nu_t \left(\frac{\partial \bar{U}_i}{\partial x_j} + \frac{\partial \bar{U}_j}{\partial x_i} \right) - \frac{2}{3} k \delta_{ij} \dots\dots\dots (3-28)$$

$$\nu_t = C_\mu \frac{k^2}{\varepsilon} \dots\dots\dots (3-29)$$

$$\frac{\partial k}{\partial t} + \bar{U}_j \frac{\partial k}{\partial x_j} = D_k + P_k - \varepsilon \dots\dots\dots (3-30)$$

$$\frac{\partial \varepsilon}{\partial t} + \bar{U}_j \frac{\partial \varepsilon}{\partial x_j} = D_\varepsilon + \frac{\varepsilon}{k} \cdot (C_{\varepsilon 1} \cdot P_k - C_{\varepsilon 2} \cdot \varepsilon) \dots\dots\dots (3-31)$$

$$P_k = -\overline{u_i u_j} \cdot \frac{\partial \bar{U}_i}{\partial x_j} \dots\dots\dots (3-32)$$

$$D_k = \frac{\partial}{\partial x_j} \cdot \left(\left(\nu + \frac{\nu_t}{\sigma_k} \right) \frac{\partial k}{\partial x_j} \right) \dots\dots\dots (3-33)$$

$$D_\varepsilon = \frac{\partial}{\partial x_j} \cdot \left(\left(\nu + \frac{\nu_t}{\sigma_\varepsilon} \right) \frac{\partial \varepsilon}{\partial x_j} \right) \dots\dots\dots (3-34)$$

Here, $C_\mu = 0.09$, $\sigma_k = 1.0$, $C_{\varepsilon 1} = 1.44$, $C_{\varepsilon 2} = 1.92$, $\sigma_\varepsilon = 1.3$

3.1.2.2 The Low Reynolds type k- ε Abe-Kondoh-Nagano Model

In this study, three RANS turbulence models, Low Reynolds $k - \varepsilon$ by Abe et al., were adopted to predict airflow in monkey airway. This model has some modifications compared to the standard $k-\varepsilon$ model origin. The standard type $k-\varepsilon$ model is generally a turbulence model for analyzing a flow field with a high Reynolds number, but in order to solve the above problem, a low Reynolds number type $k - \varepsilon$ model has been developed. The low Reynolds type $k-\varepsilon$ model includes a damping function f_μ and the turbulent Reynolds number R_t when obtaining the eddy viscosity coefficient ν_t . The wall boundary condition is applied as non-slip after the mesh is divided into sufficiently fine in the region near the wall surface. For the equation of the dissipation rate ε , model functions of f_1 and f_2 are introduced in the production term and the dissipation term. The reproducibility of laminar flow field by the turbulence behavior near the wall, the effect of low Reynolds number and reduction of distortion are studied.

The low Reynolds type $k - \varepsilon$ model is shown in Table 3.2. D and E are introduced as additional terms when using f_u, f_1 and f_2 that represent model functions. In the basic equations in Table 3.2, assuming that $f_u = f_1 = f_2 = 0, D = E = 0$, it becomes a normal standard type $k-\varepsilon$ model as shown in Table 3.1.

Table 3.2 The low Reynolds type k - ε model (flow field only)

$$\frac{\partial \bar{U}_i}{\partial t} + \bar{U}_j \cdot \frac{\partial \bar{U}_i}{\partial x_j} = -\frac{1}{\rho} \cdot \frac{\partial \bar{P}}{\partial x_i} + \nu \frac{\partial}{\partial x_j} \left(\frac{\partial \bar{U}_i}{\partial x_j} + \frac{\partial \bar{U}_j}{\partial x_i} \right) - \frac{\partial}{\partial x_j} \overline{u_i u_j} \quad \dots \quad (3-35)$$

$$-\overline{u_i u_j} = \nu_t \left(\frac{\partial \bar{U}_i}{\partial x_j} + \frac{\partial \bar{U}_j}{\partial x_i} \right) - \frac{2}{3} k \delta_{ij} \quad \dots \quad (3-36)$$

$$\nu_t = C_\mu \cdot f_\mu \cdot \frac{k^2}{\varepsilon} \quad \dots \quad (3-37)$$

$$\frac{\partial k}{\partial t} + \bar{U}_j \frac{\partial k}{\partial x_j} = D_k + P_k - (\bar{\varepsilon} + D) \quad \dots \quad (3-38)$$

$$\frac{\partial \bar{\varepsilon}}{\partial t} + \bar{U}_j \frac{\partial \bar{\varepsilon}}{\partial x_j} = D_\varepsilon + \frac{\bar{\varepsilon}}{k} \cdot (C_{\varepsilon 1} \cdot f_1 \cdot P_k - C_{\varepsilon 2} \cdot f_2 \cdot \bar{\varepsilon}) + E \quad \dots \quad (3-39)$$

$$P_k = -\overline{u_i u_j} \cdot \frac{\partial \bar{U}_i}{\partial x_j} \quad \dots \quad (3-40)$$

$$D_k = \frac{\partial}{\partial x_j} \cdot \left(\left(\nu + \frac{\nu_t}{\sigma_k} \right) \frac{\partial k}{\partial x_j} \right) \quad \dots \quad (3-41)$$

$$D_\varepsilon = \frac{\partial}{\partial x_j} \cdot \left(\left(\nu + \frac{\nu_t}{\sigma_\varepsilon} \right) \frac{\partial \bar{\varepsilon}}{\partial x_j} \right) \quad \dots \quad (3-42)$$

$$\bar{\varepsilon} = \varepsilon - 2\nu \left(\frac{\partial \sqrt{k}}{\partial x_k} \right)^2 \quad \dots \quad (3-43)$$

The above equation for transport of k , along with the equation for transport of ε , constitute the two additional transport equations to be solved in addition to the RANS equations in the low Reynolds k- ε turbulence model. Furthermore, f_μ and f_ε are new parameters represent for

damping functions in velocity field turbulence model. Damping functions of this model introduced the Kolmogorov velocity instead of friction velocity as the velocity scale that can avoid the singularity problems associated with the friction velocity at the separating and reattaching points. In equation (3.44) and (3.46), y^* is non-dimensional distance from the wall surface, R_t is turbulent Reynolds number, and u_ε is Kolmogorov velocity that can be calculated as follow Table 3-3:

Table 3.3 The Low Reynolds type k- ε Abe-Kondoh-Nagano Model (flow field only)

$f_\mu = \left\{ 1 - \exp\left(-\frac{y^*}{14}\right) \right\}^2 \left[1 + \frac{5}{R_t^{3/4}} \cdot \exp\left\{ -\left(\frac{R_t}{200}\right)^2 \right\} \right] \dots\dots\dots (3-44)$
$f_1 = 1.0 \dots\dots\dots (3-45)$
$f_2 = \left\{ 1 - \exp\left(-\frac{y^*}{3.1}\right) \right\}^2 \left[1 - 0.3 \cdot \exp\left\{ -\left(\frac{R_t}{6.5}\right)^2 \right\} \right] \dots\dots\dots (3-46)$
$\bar{\varepsilon} = \varepsilon = 2\nu \left(\frac{\partial \sqrt{k}}{\partial y} \right)^2 \dots\dots\dots (3-47)$
$R_t = \frac{k^2}{\nu \varepsilon} \dots\dots\dots (3-48)$
$y^* = \frac{u_\varepsilon y}{\nu} = \frac{y}{\eta} \dots\dots\dots (3-49)$
$\eta = \frac{\nu^{3/4}}{\varepsilon^{1/4}} \dots\dots\dots (3-50)$
$u_\varepsilon = (\nu \varepsilon)^{1/4} \dots\dots\dots (3-51)$
$\text{ここに } C_\mu = 0.09, \sigma_k = 1.4, C_{\varepsilon 1} = 1.5, C_{\varepsilon 2} = 1.9, \sigma_\varepsilon = 1.4, D = E = 0$

Here, the expression (3-47) expresses the wall boundary condition of ε . Also, η given by the expression (3-50) means the length scale of Kolmogorov.

3.2 NUMERICAL SETUP AND VALIDATION prediction

3.2.1 Grid design

3.2.1.1 Near-wall treatment

Turbulent flows in enclosed duct and tube are used to influence by the solid surfaces referred to as "walls" in this case. Near wall, the tangential velocity fluctuations are damping faster than the other side due to viscosity effect. In the far away from wall, in contrast, turbulence is increased by the production of turbulence kinetic energy due to the high gradients in the mean velocity.

Through the experimental records, the near-wall region is might subdivided into three layers. The innermost layer is called the viscous sub-layer where the flow is considered laminar, and the molecular viscosity plays a dominant role. The outer layer is recognized as fully turbulent layer. There are a buffer layer which is located between the viscous sub-layer and the fully turbulent layer, and the effects of molecular viscosity and turbulence are equally important. To numerically resolve a solution in the sub-layer requires a very fine mesh, since the sub-layer is thin and gradients are large.

The high-Reynolds number models, such as standard $k-\epsilon$ model or RNG $k-\epsilon$ model, are not solved the viscous sub-layer and buffer layer to reduce the computer burden. Semi-empirical formulas that are called "wall functions" are used to link the viscosity-affected region between the wall and the fully turbulent region. The two approaches to the sub-layer problem are illustrated in Figure 2.5 (Ansys Fluent, 2009).

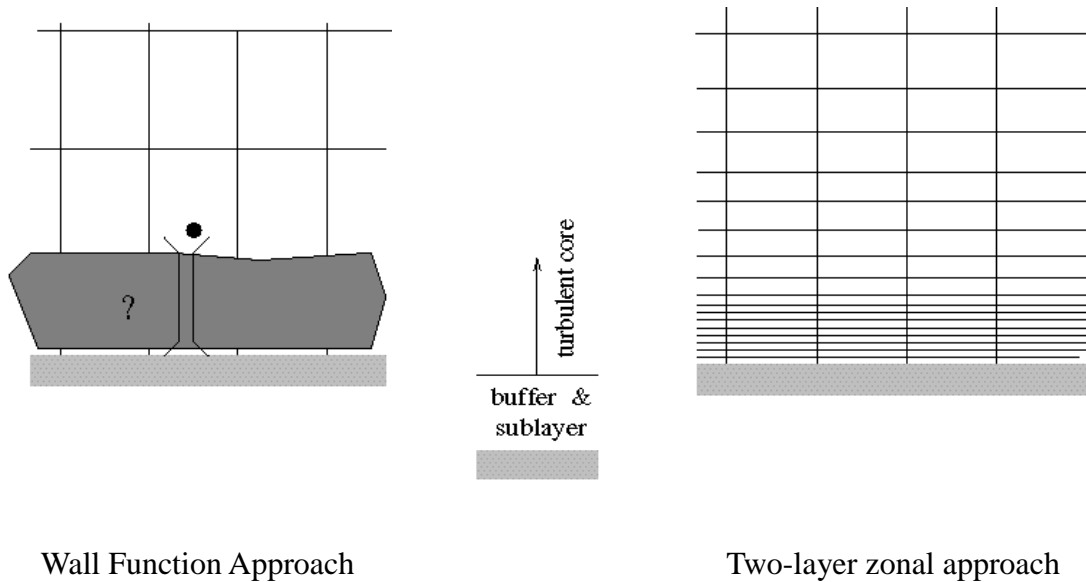


Figure 3.1 Near-wall grids

The wall function is based on the assumption that the velocity follows the log law-of-the-wall:

$$U^* = \frac{1}{\kappa} \ln(Ey^*) \dots\dots\dots (3-52)$$

where

$$y^* = \frac{\rho C_{\mu}^{1/4} k_P^{1/2} y_P}{\mu} \dots\dots\dots (3-53)$$

In case of $y^* \geq 11.225$, the U^* is calculated as

$$U^* = \frac{U_p C_{\mu}^{1/4} k_P^{1/2} y_P}{\tau_w / \rho_g} \dots\dots\dots (3-54)$$

Otherwise, $y^* < 11.225$, the U^* is considered equal to y^* , $U^* = y^*$. E is an empirical constant that depends on the roughness of the walls, κ is the von Karman constant, U_p is the velocity in the center of the cell adjacent to the wall, y_p is the distance between the wall and the cell center,

k_p is the turbulent kinetic energy in the cell center, and τ_w is wall shear stress.

$$\tau_w = \frac{U_p C_\mu^{1/4} k_p^{1/2}}{U^* / \rho} \dots\dots\dots (3-55)$$

We can define a Reynolds number based on the distance to the wall y^+ and make the velocity

U^+ at y as the usual notation in the turbulent field:

$$y^+ = \frac{\sqrt{\tau_w / \rho_g}}{\nu} y_p \dots\dots\dots (3-56)$$

$$U^+ = \frac{U_p}{\sqrt{\tau_w / \rho_g}} \dots\dots\dots (3-57)$$

$$u_\tau = \sqrt{\frac{\tau_w}{\rho}} \dots\dots\dots (3-58)$$

The wall function approach has a disadvantage that it relies on empirical correlations. The two-layer zonal model is preferred apply to calculate the low-Reynolds flows or flows with complex near-wall phenomena. Zones distinguished by a wall-distance-based turbulent Reynolds number:

$$\text{Re}_y \equiv \frac{\rho \sqrt{k}}{\mu} y \dots\dots\dots (3-59)$$

Regular turbulence models are used in the turbulent core region. The k equation is solved in the viscosity-affected region and ε is computed using a correlation for the turbulent length scale.

The solution of two-layer zonal model is dynamic and adaptive.

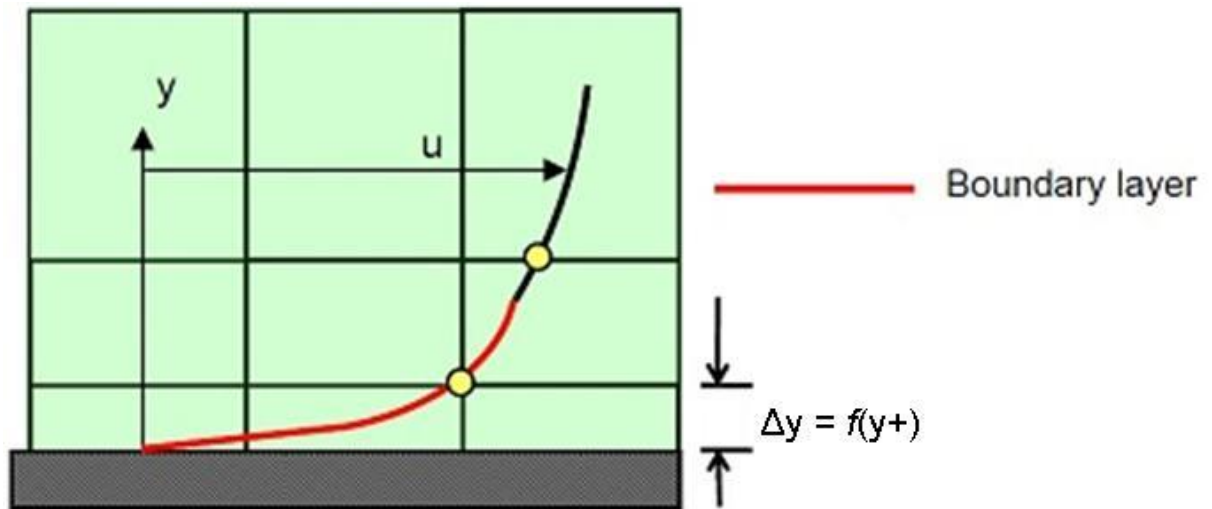


Figure 3.2 y^+ value for boundary layer

3.2.1.2 Model construction

The data used to construct the digital model came from micro-CT images analysis of serial coronal scans from a 1.2-kg, 6-month-old male rhesus monkey. The micro-CT data was provided by third parties (Ina-Research Co.) and no rhesus monkey was euthanized for the purpose of this study. The micro-CT imaging from the upper airway of the monkey consisted of two-dimensional coordinates of airway perimeters for cross sections spaced at intervals of 200 μm . In all, 161 sagittal sections, 185 coronal sections and 306 axial sections were used to span a distance of 105 mm from the tip of the nostril through the trachea. Geometry of the airway with cross-sectional areas estimated from micro-CT images obtained from rhesus monkey. The original CT images were converted into a compatible file format by using Mimics® (Materialise NV) to generate and modify 3D surface models. A surface model was generated from continuous 2D contour data by translating segmented, modified, and smoothed contour

points into a data series that was loaded into ANSYS preprocessing software package ICEM-CFD (ANSYS Inc.). Surface geometries of the monkey respiratory tract were also exported as an STL file format. The monkey respiratory tract model possessed an inner surface area approximately $2.81 \times 10^{-5} \text{ m}^2$. The information of original monkey's geometry is shown in Table 2.1 (chapter 2). In the nose, the area distributions are shown separately for the left and right cavities. Features of interest include the nostril surface (A), nasal palantine duct (B), anterior extent of the middle turbinate (C), ventral meatus on the lateral side of the ventral turbinate (D), oral cavity (E), beginning of the trachea (F), and outlet (G). Five characteristic structure regions are also indicated as nasal vestibule, central nasal and oral passages, pharynx, larynx and trachea (figure. 3.3). Plot of cross-sectional area along the main flow direction. Most of the data is taken from cross sections corresponding to the serial sections used to construct the model. The locations of the labeled points (1–17) correspond to the locations of the representative sections shown in Figure 3.4. The minimum cross-sectional area in the monkey airway occurs at plane 15. This plane is located through way from cavities (nasal and oral) to trachea where the single airway. In the post-septal airway, a series of minima occur in the laryngopharyngeal zone in the region of planes 15. The plane area of left and right nasal has similar and indicate that left and right is red and blue line, respectively. The gray line indicate the plane area of oral. The green line, also, indicate single airway from larynx to trachea.

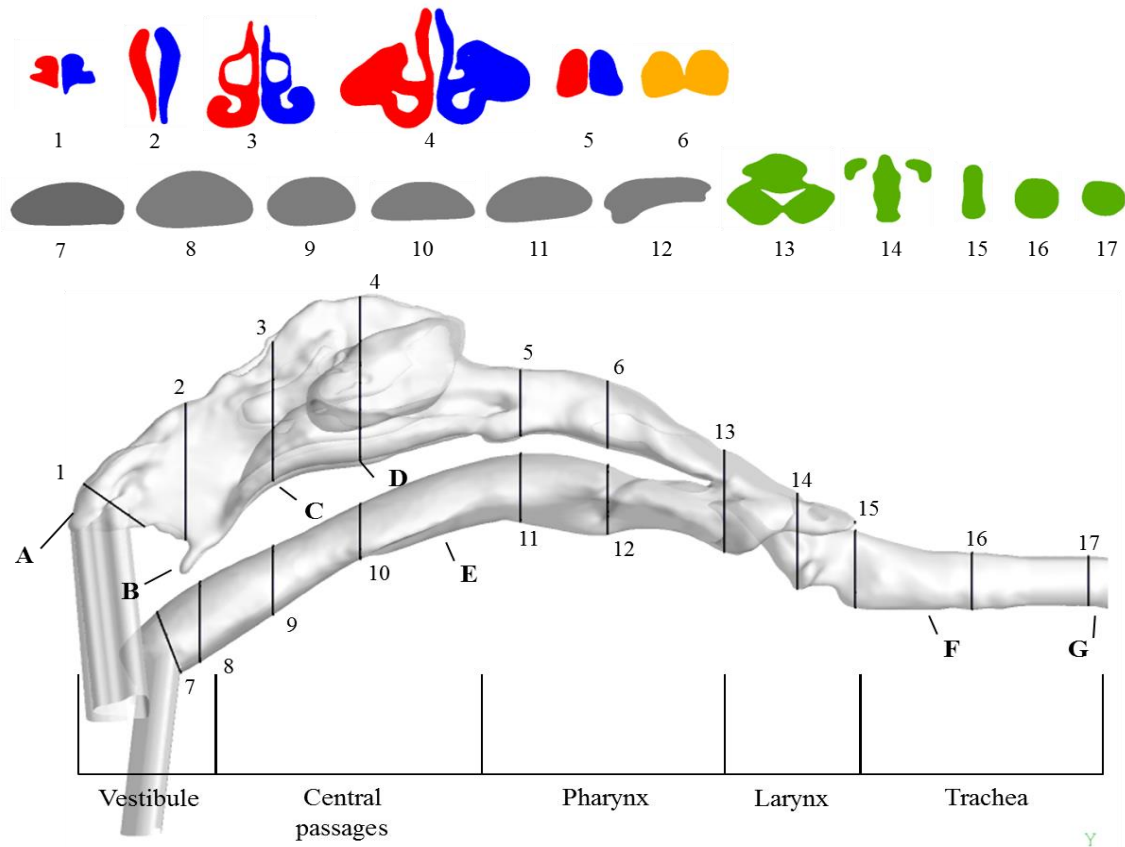


Figure 3.3 Lateral view of the nasal airway composed of 161 sagittal sections, 185 coronal sections and 306 axial sections that span a distance of 105 mm. Seventeen representative sections are also shown in frontal view.

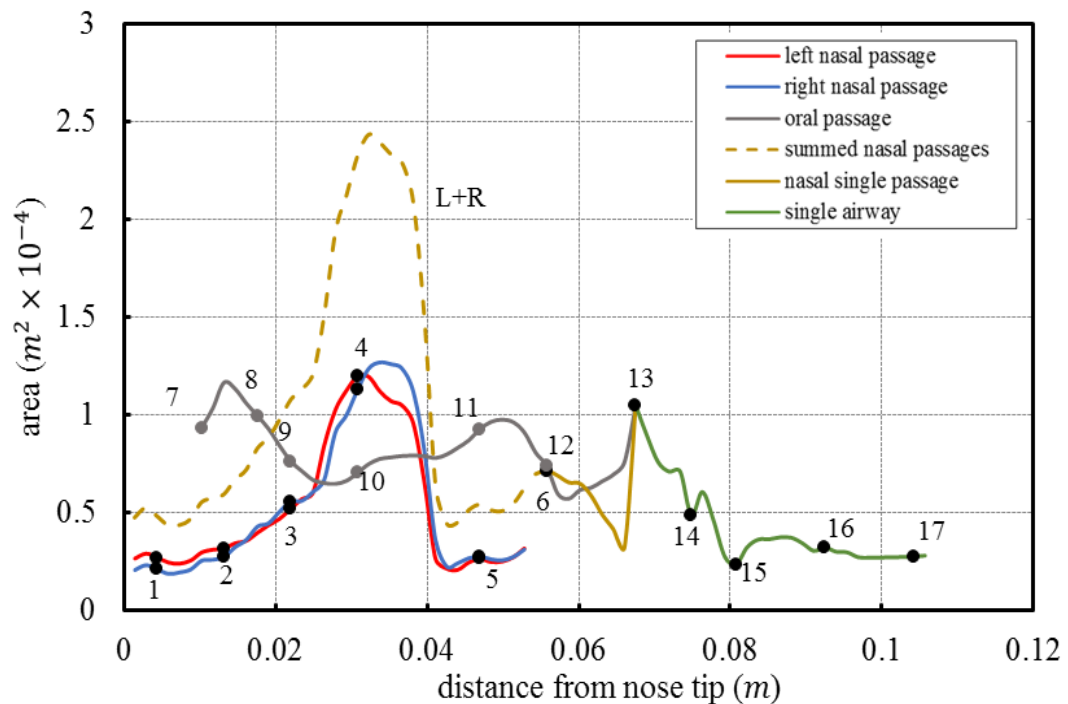


Figure 3.4 Cross-sectional area of nasal and oral passages

First cell height for prism layer

The triangular surface tessellations were re-meshed (ICEM-CFD) to provide high-quality surface elements for computational simulations. (See figure 2.5 in chapter 2). Volume meshing (ANSYS ICEM-CFD v 16.0) of each configuration yielded an unstructured mesh with a core of tetrahedral elements and ten prism layers adjacent to the wall, for improved boundary layer resolution. The solutions were performed on medium to high resolution meshes (approx. 4–10 million tetrahedron elements), with the first prism height typically within $y^+ \leq 1$. The typical densities of volume meshes are indicated in figure 3.5.

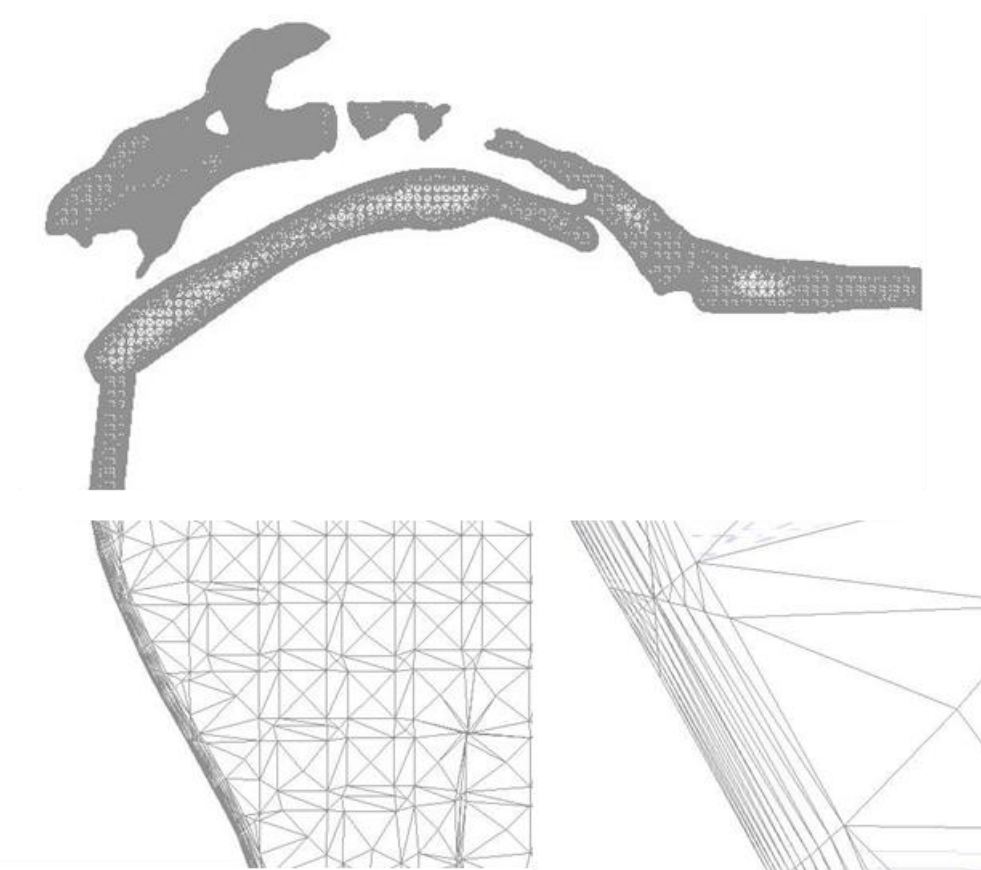


Figure 3.5 tetrahedral elements and ten prism layers adjacent to the wall

3.2.2 Inflow boundary profile prescription for numerical simulation of oral and nasal airflow

The study of how the air through the airway relies particularly on numerical simulation because the complexity and relative inaccessibility of the anatomy prevent detailed in vivo measurement.

In this study, a blunt velocity profile were applied at the entrance of a pipe inflow tract. This is of interest to experimentalists as it addresses concerns regarding the required entrance length for developed flow, and the effect of the flow loop profile (at the entrance to the convergent pipe inflow) on experimentally resolved airflow patterns. In the PIV measurement, a pipe was converged on the nostril and mouth to fully develop the inlet air flow. The effect of the inflow geometry on flow predictions during steady nasal and oral inspiration is important in computational simulation. The study of different inflow boundary configurations about velocity profile and the entrance to a convergent pipe inflow is described in D.J. Taylor *et al.* (2010). Computational simulations using configurations the convergent pipe highlight the negligible impact of applying either a blunt or parabolic boundary profile at the entrance of the convergent inflow tract. This is helpful to experimentalists as it negates the need for flow loops extensive enough to provide a fully developed (or known) velocity profile at the replica model inflow (which may be considerable for scaled-up models). The level of sensitivity to inflow prescription was found to be relatively low for qualitative flow patterns and gross flow measures. In the model for CFD, a pipe was converged on the nostril and mouth in accordance with experimental scenarios, as the inlet boundary condition for fully developed air flow.

3.2.3 Grid independence study

Solving a CFD problem, a continuous solution space is approximated using discrete elements. These discrete elements form the target mesh. As the number of elements used to approximate the continuous solution increases, the accuracy of the CFD method used to calculate the actual solution also increases. But, as the number of elements increases, the computational cost required to get the solution also increases. The optimization for numerical simulation is needed to obtain an accurate solution using the least amount of computational resources. Mesh or grid independence study is carried to determine this optimum point where an accurate solution for the problem is found at the expense of least computational resources. In other words, given a level of accuracy (the deviation of the solution calculated from the CFD method, compared to the actual solution of the Navier-stocks equations) for the solution, the mesh used is good enough to achieve that accuracy at the expense of minimum possible computational power. Using an optimum mesh, the accuracy of the results are good enough to capture all the necessary flow features, their gradients and so forth. In other words, a coarse grid will not capture all the flow features (not a solution of required accuracy) and a finer mesh will give a solution of a little higher accuracy than required but at the expense of computational power and time. The adequacy of grid resolution is tested by verifying fluid result at the flow rate of 4 L/min. Figure 3.6 shows CFD results of the grid independence check with scalar velocities along the A-B section. Five levels of grid resolution were adopted: 4.0 million, 6 million, 8 million, 10 million and 12 million total mesh cells. The mean velocity taken at a cross-line at trachea region agrees

well in the case of 10 million meshes. Hence the monkey airway geometry in case of 10 million meshes is sufficient for predicting accurately efficient calculation time in this study.

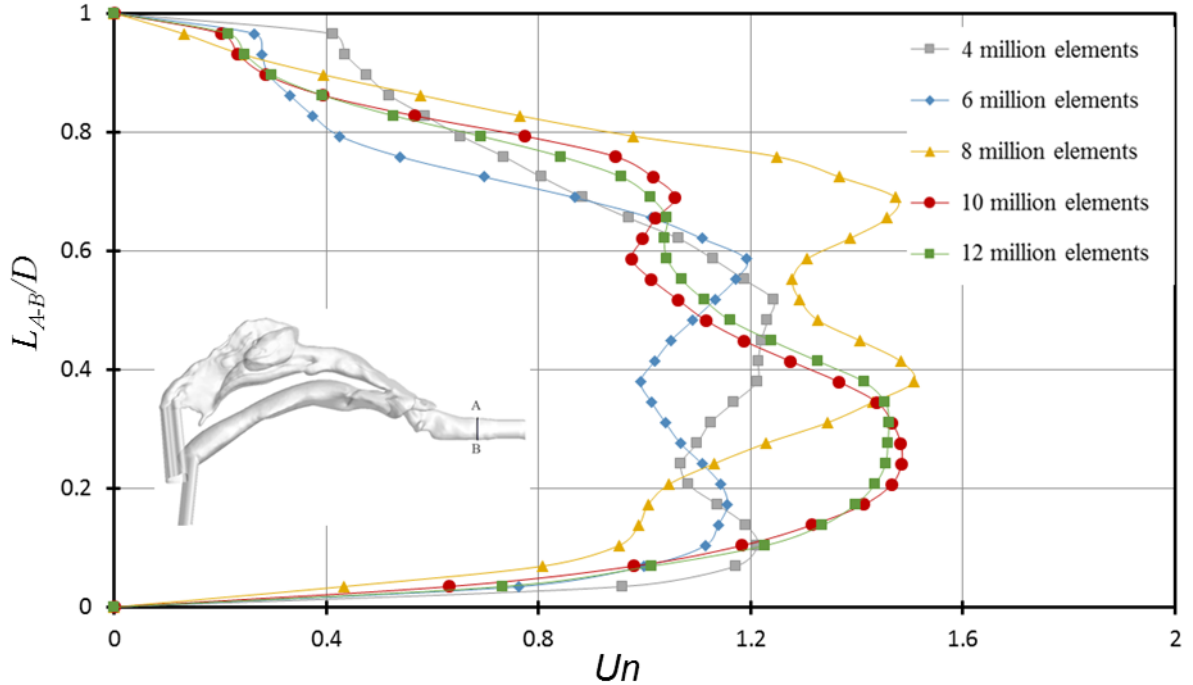


Figure 3.6 The results of the grid independence check

3.3 CONCLUSION AND DISCUSSIONS

In this chapter 3, the mathematical equations and numerical models used for the numerical simulations were described. CFD is based on the governing equations of fluid dynamics. The Navier-Stokes equation was introduced for mathematical statements of the conservation laws of physics, consisting of a continuity equation, momentum equations. For the numerical simulation, the Low Reynolds type k- ϵ Abe-Kondoh-Nagano Model was selected as turbulence model to consider near wall treatment where parabolic profiles are obtained in the viscous sub-layer. In order to increase the accuracy of computational simulation, y^+ value for viscous sub-layer was considered for the prism layers. In the CFD model, a pipe was converged on the

nostrils and mouth in accordance with experimental scenarios, as the inlet boundary condition for fully developed inflow profile.

For the grid independence check, volume meshing of each configuration yielded an unstructured mesh with a core of tetrahedral elements and ten prism layers adjacent to the wall, for improved boundary layer resolution (Five levels of grid resolution were adopted: 4.0 million, 6 million, 8 million, 10 million and 20 million total mesh cells). The monkey airway geometry in case of 10 million meshes was considered sufficient for prediction accuracy in this study.

In order to validate the CFD results, the PIV experimental results will be used in chapter 4.

Reference

- 3-1) 荒川忠一:数値流体力学, 東京大学出版会, 1994.
- 3-2) Boussinesq, J: *Theorie Analytique de la Chaleur*, 2:157-158, Gauthier-Villars, Paris., 1903.
- 3-3) 近本智行, 村上周三, 加藤信介:浮力ダンピング下の低 Re 数流れに対応可能な新しい $k-\varepsilon$ モデル, 温度成層した室内気流の数値解析に関する研究(その2), 日本建築学会計画系論文集, 第481号, pp 67-74, 1995.
- 3-4) E. R. van Driest: *On Turbulent Flow near a Wall*, *Journal of the Aeronautical Sciences*, Vol. 23, pp. 1007-1011, 1956.
- 3-5) Germano, M., Piomelli, U., Moin, P. and Cabot, W. H.: *A dynamic subgrid-scale eddy viscosity model*, *Phys. Fluids*, A3, 1760., 1991.
- 3-6) Ghosal, S., Lund, T. S. and Moin, P.: *A local dynamic model for large-eddy simulation*, *Center for Turbulence Research, Annual Research Briefs.*, 1992.
- 3-7) 日野乾雄:流体力学, 朝倉書店, 1974.
- 3-8) J. S. Smagorinsky: *General Circulation Experiments with the Primitive Equations*, Part I, *Basic Experiments*, *Monthly Weather Review*, Vol.91, pp99-164, 1963.
- 3-9) K. Abe, T. Kondo, Y. Nagano: *A New Turbulent Model for Predicting Fluid Flow and Heat Transfer in Separating and Reattaching Flows – 1*, *Flow Fields Calculations*, *Int. J. Heat Mass Transfer*, Vol. 37. No. 1., pp139-151, 1994.
- 3-10) K. Abe, T. Kondo, Y. Nagano: *A New Turbulent Model for Predicting Fluid Flow and Heat Transfer in Separating and Reattaching Flows – 1*, *Thermal Fields Calculations*, *Int. J. Heat Mass Transfer*, Vol. 38. No. 8., pp1467-1481, 1995.
- 3-11) K. Akselvoll and P. Moin: *Engineering Applications of Large Eddy Simulation*, FED-Vol.1162, ASME, 1993.
- 3-12) Launder, B. E., and Spalding, D. B.: *Mathematical Models of Turbulence*, Academic Press, 1972.
- 3-13) Launder, B. E., and Spalding, D. B.: *The Numerical Computation of Turbulent Flows*, *Computer Methods in Applied Mechanics and Engineering*, 1974.
- 3-14) L. C. Rotta: *乱流*, 岩波書店, 1975.
- 3-15) Lilly, D. K.: *A proposed modification of the Germano subgrid-scale closure method*, *Phys. Fluids* A4, 633, 1992.
- 3-16) Meneveau, C., Lund, T. S. and Cabot, W.: *Center for Turbulence Research, Summer Program*, 1994.
- 3-17) 村上周三: *風工学のための乱流数値シミュレーション*, 第138回生研セミナーテキスト, 1988.
- 3-18) 村上周三, 加藤信介, 近本智行: *低 Re 数領域にも適用可能な新しい $k-\varepsilon$ モデル*, 温度成層した室内気流の数値解析に関する研究(その1), 日本建築学会計画系論文集, 第476号, pp9-17, 1995.
- 3-19) Patankar, S., V.: *コンピュータによる熱移動と流れの数値解析*, 森北出版, 1985.

- 3-20) 数值流体力学編集委員会編:3 乱流解析, 東京大学出版会, 1995.
- 3-21) S. Murakami, S. Kato, T. Chikamoto, D. Laurence and D. Blay: New Low-Reynolds-Number k - ϵ model including damping effect due to Buoyancy in a stratified Flow Field, *Int. J. Heat Mass Transfer*, Vol. 39, No. 16, pp 3483-3496, 1996.
- 3-22) Tennekes, H., and Lumly, J. L.: *A First Course in Turbulence*, The MIT Press, 1972
- 3-23) W. Rodi : *Turbulence Models for Environmental Problems, Prediction Methods of Turbulent Flows*, A von Karman Institute Book, pp259~350, 1980.
- 3-24) M. F. Modest. *Radiative Heat transfer*. Series in Mechanical Engineering. McGraw-Hill, 1993.
- 3-25) M. E. Larsen and J. R. Howell. Least Squares Smoothing of Direct Exchange Areas in Zonal Analysis. *J. Heat Transfer*, 108:239-242, 1986.
- 3-26) ANSYS/ Fluent ver. 16.0, User Manual
- 3-27) Taylor, D.J., Doorly, D.J., Schroter, R.C., Inflow boundary profile prescription for numerical simulation of nasal airflow. *J. R. Soc. Interface* 7, 515–527. <https://doi.org/10.1098/rsif.2009.0306>, 2010.

CHAPTER 4

NUMERICAL PREDICTION OF MONKEY AIRWAY MODEL

4.1 VALIDATION FOR NUMERICAL SIMULATION USING PIV RESULTS

Particle image velocimetry (PIV) and computational fluid dynamics (CFD) modeling of air flow through a respiratory tract have been carried out in order to assess the role of physiology.

For the computational simulation regarding the targeted monkey airway model, ICEM–CFD software was used, and volume meshes were created by using unstructured meshes with tetrahedral elements (total 10 million elements). Furthermore, 10 prism layers adjacent to the wall were created for improved boundary layer resolution (described in chapter 3). For the numerical simulation, the Reynolds number (Re) was matched in terms of similarity rule between scale experiment and numerical simulation and was determined as shown in equation (4-1).

$$Re = \frac{L_{real}}{v_{air}} V_{air} = \frac{L_{silicone\ model}}{v_{working\ fluid}} V_{working\ fluid} \dots\dots\dots (4-1)$$

Table 4.1 and 4.2 lists the cases of numerical simulation based on Reynolds number matching and numerical and boundary conditions for CFD, respectively.

Table 4.1 Cases of numerical simulation based on Reynolds number matching

Q_{air} (L/min)	$V_{working\ fluid}$ (m/s)	V_{air} (m/s)	Reynolds number (Re)
4	0.0745	0.0745	938
10	0.1863	0.1863	2346
20	0.3725	0.3725	4692

Table 4.2 Numerical and boundary condition for CFD

Turbulence model	Low Re type k- ϵ model (Abe–Kondoh–Nagano model)
Mesh design	10 million cell mesh (Unstructured, Tetrahedral with 10 prism layer)
Algorithm	Steady state with SIMPLE algorithm
Scheme	Convection term: Second order upwind Others: second order upwind
Inflow boundary condition	Pressure inlet on the convergent pipe on the nostrils and mouth, Turbulent intensity TI (%) = 10
Outflow boundary condition	$U_{out} = -2.3725$ m/s (4 L/min) $U_{out} = -5.9312$ m/s (10 L/min) $U_{out} = -11.8624$ m/s (20 L/min)
Wall treatment	Velocity: no slip
Others	Isothermal condition

Velocity obtained by CFD prediction is compared against PIV obtained for same geometry and boundary condition. In order to validate the CFD results, the case of 4 L/min were compared based on the nasal and oral inhalation. The velocity values are calculated as scalar velocities by using two velocity components. The mean velocities at cross line L1-6 were normalized by using the outlet velocity as shown in figure 4.1 and 4.2 ($U_{y'} / U_{out}, U_{y'} = \sqrt{u^2 + v^2}$, u : velocity magnitude of x-component, v : velocity magnitude of y-component). The cross line 1-6 has the different hydraulic diameter because of the complicated geometry. In order to recognize the

comparison between PIV and CFD results, the vertical axis is, also, normalized by using the cross line height from bottom to top inside wall of monkey airway. Figure 4.1 shows the normalized scalar velocity profile in monkey airway by PIV and CFD under nasal inhalation condition. To compare the profile of flow profile, the cross line in nasal cavity is divided line 3 for left and right and line 4 for left and right as shown figure 4.1(a),(b),(c) and (d).

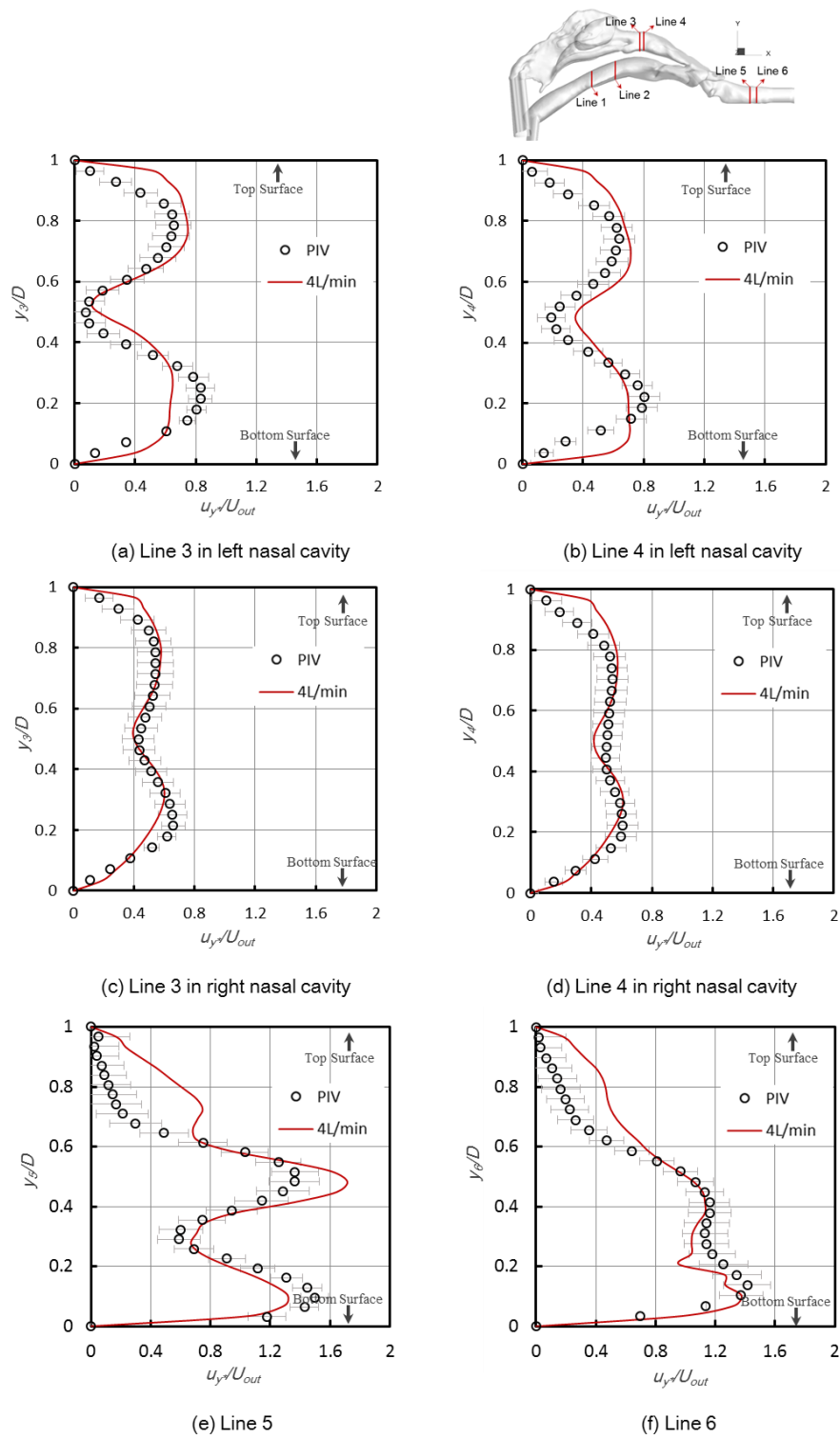


Figure 4.1 The normalized scalar velocity in monkey airway by PIV and CFD under Nasal inhalation Condition (4 L/min)

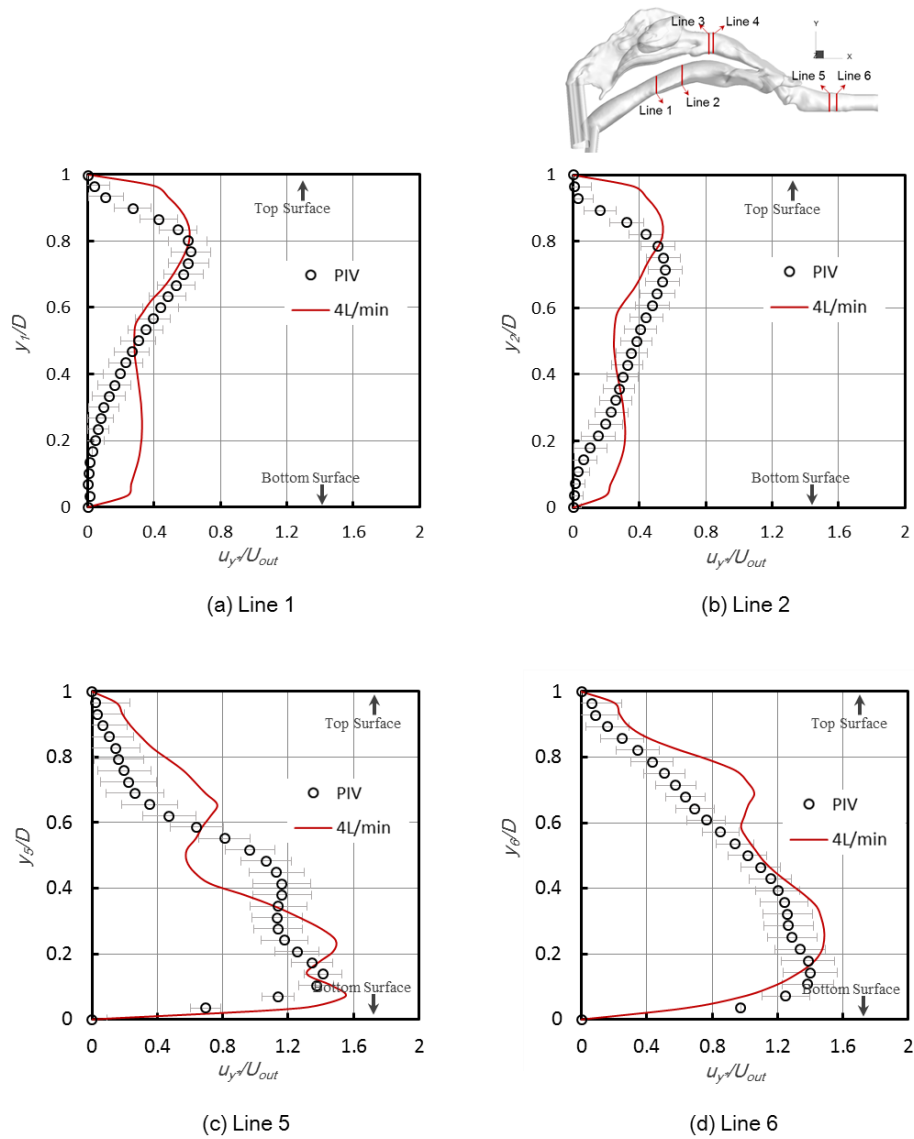


Figure 4.2 The normalized scalar velocity in monkey airway by PIV and CFD under Oral inhalation Condition (4 L/min)

The profile of CFD results was similar to PIV results. However, lines 3 and 4 of the left nasal cavity had significant differences when comparing to lines 3 and 4 of the right nasal cavity.

Figure 4.2 shows the normalized scalar velocity profile in monkey airway by PIV and CFD calculations under oral inhalation condition.

4.2 COMPARISON OF CFD ANALYSIS RESULTS AND PIV EXPERIMENTAL RESULTS

CFD simulations were conducted to investigate the tracheal flow profile associated with the two inhaling modes (nasal and oral) and three flow rates. The three flow rates, Q_{air} , were of 4, 10 and 20 L/min, respectively. CFD simulations were also conducted with the low Reynolds number type k- ϵ models (LR-ANK). Figure 4.3 and 4.4 are normalized velocity magnitude and PIV plots of these results for nasal and oral inhalation condition, respectively. CFD results can be compared with corresponding PIV maps. The velocity values were calculated as scalar velocities using two velocity components ($U_{y^*} / U_{out}, U_{y^*} = \sqrt{u^2 + v^2}$, u : velocity magnitude of x-component, v : velocity magnitude of y-component). In figure 4.3, the laryngeal jet is apparent, which transfers more momentum from larynx to the flow downstream (trachea). The highest velocities in the flow field ($>2U_{inlet}$) are achieved at the larynx region, which then pass to the trachea under nasal and oral inhalation. This acceleration is caused by the inclination, unique shape, and contracting cross-sectional area of the trachea region. Because of the laryngeal jet, this high-speed flow enters the trachea at an angle, impinging against and flowing along the anterior wall of the trachea. This induces a recirculation region in the beginning of the trachea which extends downstream. The velocity contours show that the basic structure of the flow field is predicted well by the CFD computation, and that changing the inlet boundary condition has some effect on the simulated flow structure. The effects of the different inlet conditions on velocity magnitudes are largely confined to the monkey airway via nasal/oral

routes.

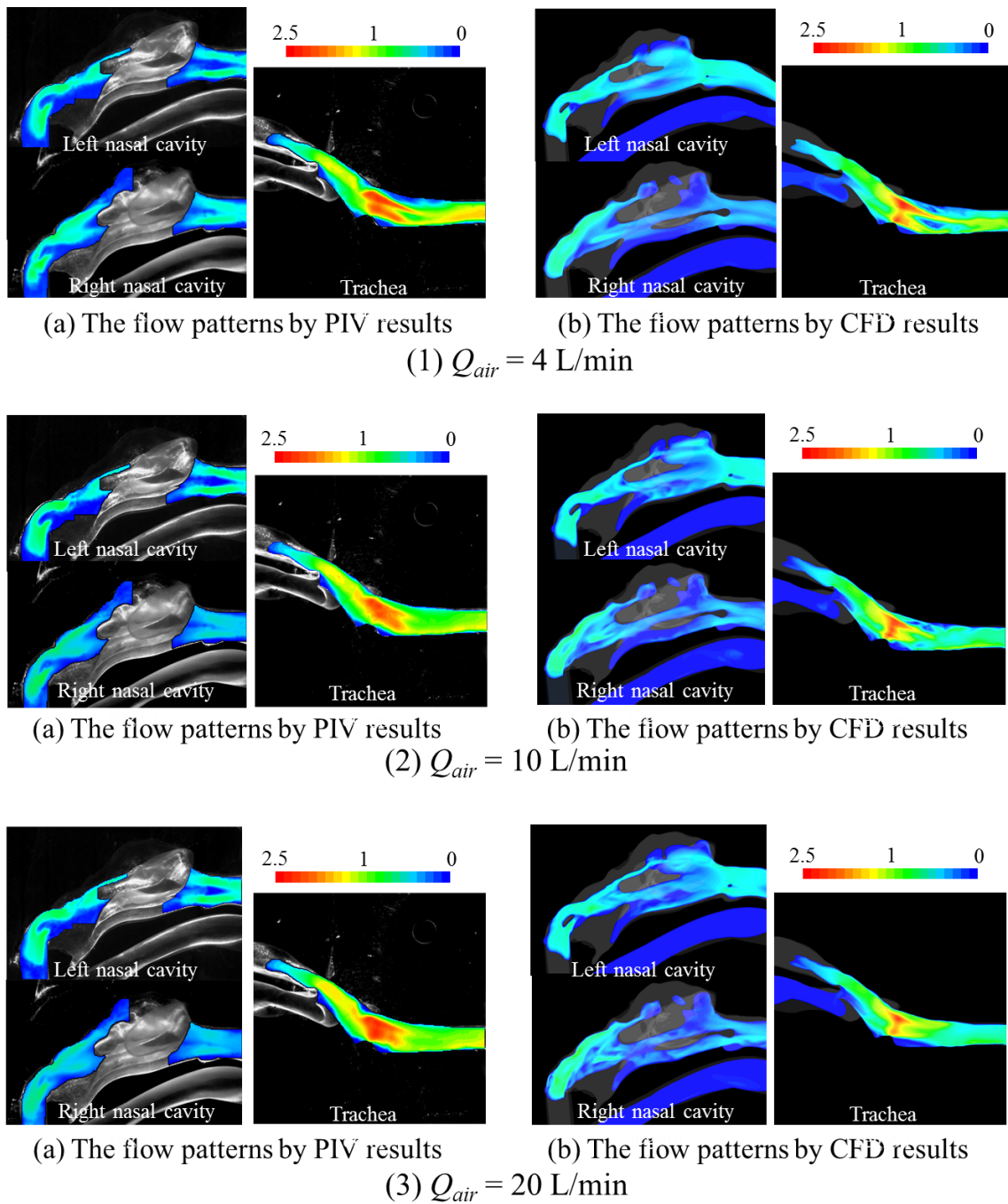


Figure 4.3 Scalar Velocity Distributions by PIV and CFD under Nasal inhalation Condition

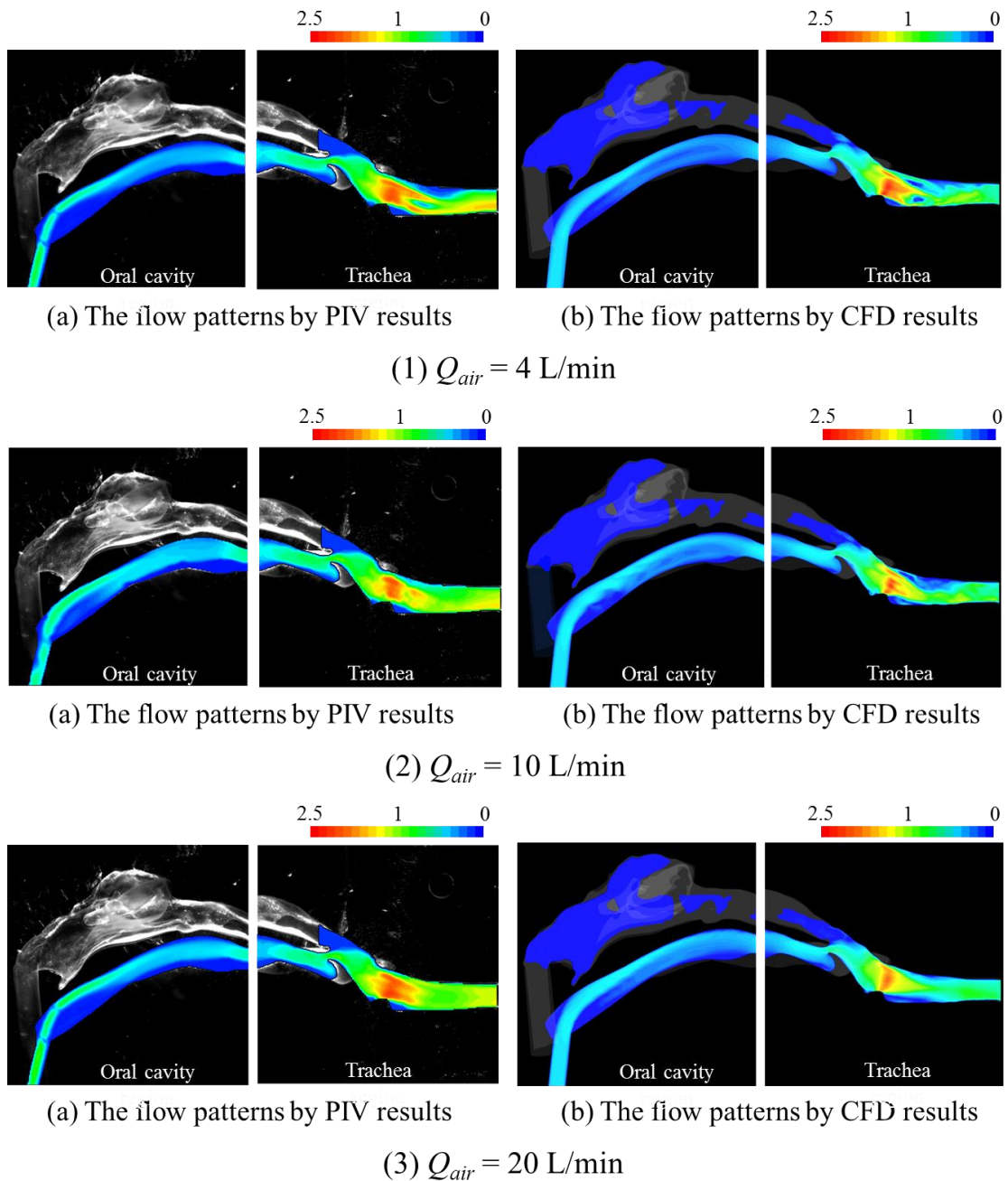


Figure 4.4 Normalized Scalar Velocity Distributions by PIV and CFD under Oral inhalation Condition

The velocity magnitude plots for all three inlet conditions and both inhalation methods were reasonably similar to the experimental results. All the major separation regions were well captured in the flow rates of 4, 10 and 20 L/min. The structure of the separated flow in the trachea was indicated in the CFD contour patterns. The overall flow patterns obtained from PIV

and CFD in the respiratory tract showed qualitatively good agreement with each other. In nasal cavity, the significant differences of flow patterns in left and right cavities were observed because of bilateral asymmetry of the original monkey. The existence of a pipe at the opening of the mouth, for supplying the air, exerted a certain influence on the flow field formation in the oral cavity.

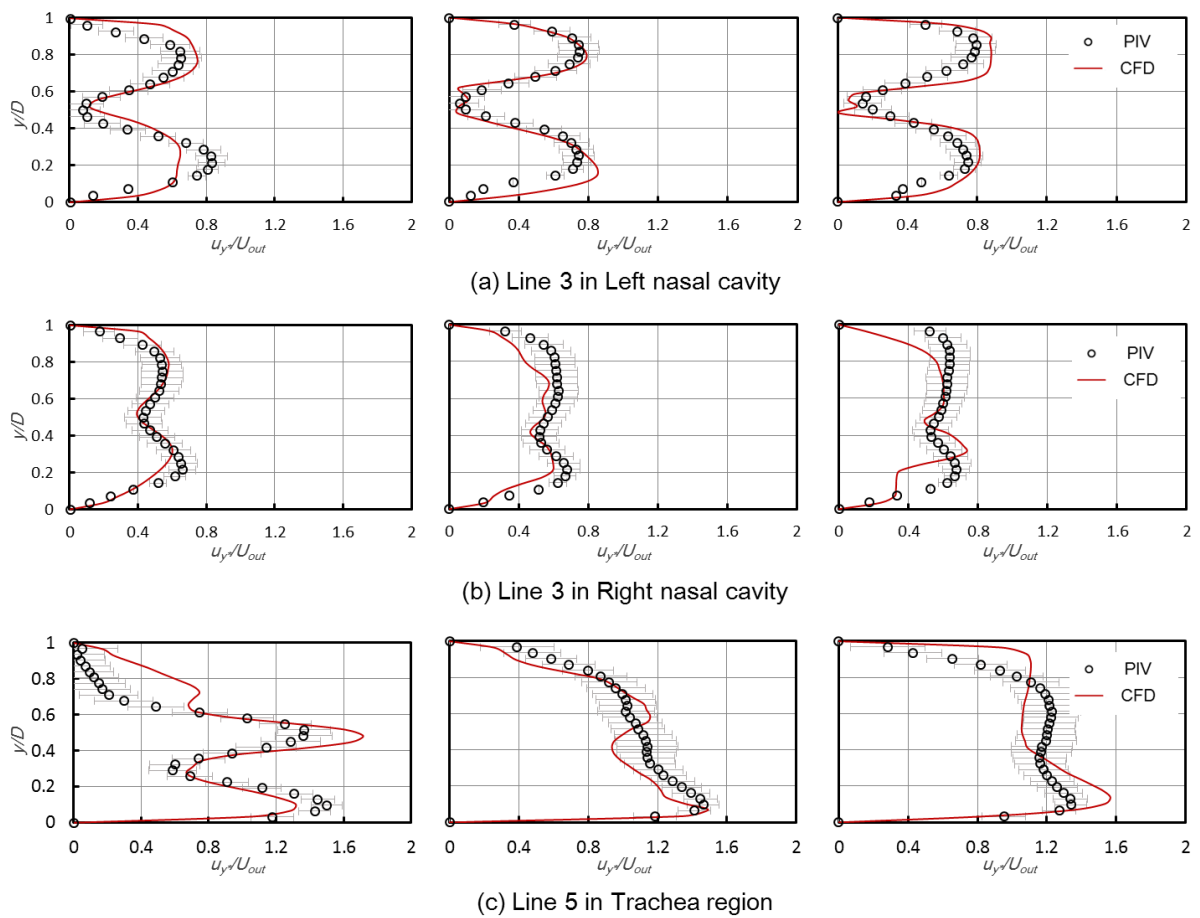


Figure 4.5 Profiles of normalized scalar velocity under Nasal inhalation Condition

(Left: 4 L/min, Center: 10 L/min, Right: 20 L/min) ($U_{y^*}/U_{out}, U_{y^*} = \sqrt{u^2 + v^2}$)

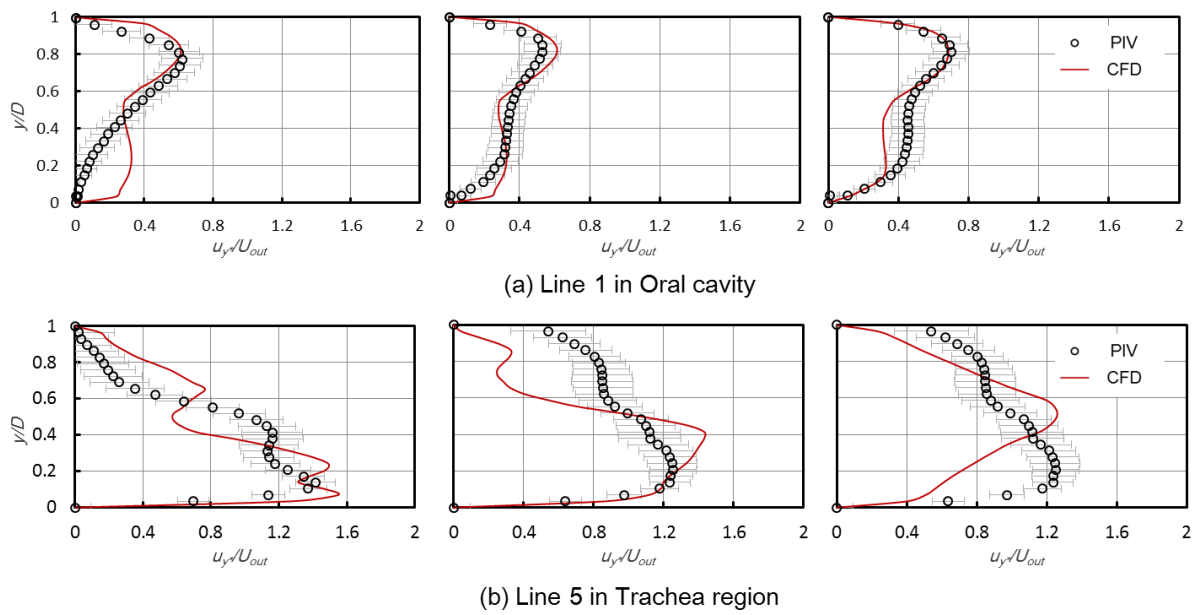


Figure 4.6 Profiles of normalized scalar velocity under Oral inhalation Condition

(Left: 4 L/min, Center: 10 L/min, Right: 20 L/min) ($U_{y^*}/U_{out}, U_{y^*} = \sqrt{u^2 + v^2}$)

Figures 4.5 and 4.6 show the scalar velocity profiles measured by CFD, corresponding to the cross line for PIV results as shown in Figure 2.9 (in chapter 2). Considering the profiles obtained from PIV and CFD, the tiny differences in the flow patterns of the oral cavity were caused by the differences in inlet boundary conditions. Although significant differences were confirmed quantitatively, and discrepancies of maximum velocity were approximately 10% in trachea region under 10 L/min oral inhalation condition. Under 20 L/min oral inhalation condition, profile patterns were indicated sufficiently different. The PIV and CFD results were in reasonable qualitative agreement in cavities and trachea region under 4 and 10 L/min. In the cavities and tracheal region, the velocity profiles and their magnitudes from PIV and CFD analysis agreed with each other.

4.3 CONCLUSION AND DISCUSSION

In this chapter, a Computational simulation was conducted to investigate the fluid flow pattern of the upper airway of a monkey by using Low Re type k - ϵ model (Abe–Kondoh–Nagano model), and the representative results were reported by CFD results corresponding to PIV experimental data. For the prediction accuracy, the boundary conditions of CFD were validated by using PIV experimental results. For the similarity rule between scale experiment and numerical simulation, the velocity was determined based on the Reynolds number (Re). As the PIV results were used for validation, the CFD simulation was carefully conducted to ensure that discrepancies between the experimental and CFD results were minimized. The calculation in flowfield was very challenging for the complex geometry that has highly curved and narrow spaces in many regions as it includes the nasal/oral cavity, pharynx, larynx and trachea. The flow patterns in the nasal cavity were complex due to its geometry. The difference between instantaneous CFD and averaged PIV results is a potential source of error in the validation procedure.

In the nasal cavity, the flow showed a complicated structure owing to its repeated collision, bifurcation/ separation, and reattachment inside the complicated geometry. The peak/maximum velocity in upper respiratory tract of the monkey was observed at the pharynx/larynx region, where the flow from left/right nasal cavities and/or oral cavity was confluent. The flow structure in upper airway was characterized by a region of separated flow at the start of the nasal/oral cavity, and down to the trachea. The PIV and CFD results show possibilities of contribution

towards the development of *in silico* models to replace *in vivo* and *in vitro* experiments.

CHAPTER 5

CONCLUSION, RECOMMENDATION AND FUTURE WORK

5.1 CONCLUSION

This study involved Particle Image Velocimetry (PIV) experiments and corresponding Computational Fluid Dynamic (CFD) analysis to investigate air flow patterns in the monkey upper airway including nasal and oral cavities and trachea region. A monkey was used as a representative surrogate mammal for laboratory tests. The 3D replica model of the respiratory tract of a monkey was created to visualize the air flow structure/mechanism in nasal and oral cavities. In this study, *in vitro* experiment and numerical prediction was conducted to investigate the flow distribution in the realistic geometry of a monkey airway. The *in vitro* experiment and numerical prediction models (*in silico*) were reproduced from CT data of an actual monkey airway of a 6-month-old male monkey with weight of 1.2 kg. Detailed measurements from the Particle Image Velocimetry (PIV) technique, as well as the numerical simulation through Computational Fluid Dynamics (CFD) were challenging but crucial in the understanding of respiratory system. The purpose of the study included visualizing flow inside an upper airway

with a complicated geometry.

Chapter 2

This study was performed to gain an understanding of the flow structure of the airflows within a realistic monkey upper airway by performing a PIV experiment under three constant inhalation conditions involving the following flow rates: 4 L/min, 10 L/min, and 20 L/min.

The main focus of PIV measurement was to gain a quantitative understanding of the fluid flow structure within a monkey upper airway as well as to provide well defined experimental data for CFD validation. It was assumed that the total error in estimating a single displacement vector corresponded to a sum of the bias error and the measurement uncertainty. Although there were limitations due to the complex geometry and bias error, the study involved successfully constructing a rigid and compliant optically transparent model that contained a reproduced detailed geometry of the monkey's upper airway region suitable for flow visualization and PIV experiments.

Chapter 3

This chapter introduced the selection of turbulence model and the procedure of numerical setup that were appropriate for the monkey upper airway model. Grid independence check was performed using 4, 6, 8, 10 and 12 million total mesh cell with 10 prism layer. The monkey airway geometry in the case of 10 million meshes was sufficient for prediction accuracy in this

study. Given a level of accuracy (the deviation of the solution calculated from the CFD method, compared to the actual solution of the Navier-stocks equations) for the solution, the mesh used was good enough to achieve that accuracy at the expense of minimum possible computational power and time. The results of CFD prediction under 4L/min case had good agreement with PIV experimental results.

Chapter 4

The study depicted the comparison of results between the representative velocity profiles obtained from PIV and CFD analysis. The prediction accuracy was carefully validated using PIV results in terms of fluid dynamics. The *in silico* model has considerable potential to contribute towards the understanding of inhalation exposure due to the inherent flexibility with no ethical constraints. For the similarity rule between scale experiment and numerical simulation, the velocity was determined based on the Reynolds number (Re) under 4, 10 and 20 L/min (Re 900 – 5000). In order to investigate and compare the flow patterns, the scalar distribution on vertical cross section and the normalized scalar profile of cross line were analyzed. The flow patterns showed a complicated structure owing to the repeated collision, bifurcation/ separation, and reattachment of the flow inside the complicated geometry of the cavity. The flow structure in upper airway was characterized by a region of separated flow at the start of the nasal/oral cavity, and down to the trachea. Although significant differences were confirmed quantitatively and discrepancies of maximum velocity were approximately 10% in

the trachea region under 20 L/min of oral inhalation condition, the PIV and CFD results were in reasonable qualitative agreement in cavity and trachea region. In the cavities and tracheal region, the velocity profiles and their magnitudes from the PIV and CFD analysis agreed with each other.

5.2 RECOMMENDATIONS AND FUTURE WORK

The PIV technique has the great advantage of indicating high resolution flow velocity vector information of a whole plane in the flow field. It is expected that the results of this study will significantly contribute to a validation study for developing an *in silico* model, especially in terms of CFD analysis.

In this study, the visualization within a monkey upper airway only was conducted to investigate the characteristic flow structure under steady-state. But the improved model for computational simulation has great potential to predict particle deposition and mass transfer. Further studies may also involve running the simulations under transient flow. The unsteady simulations may reveal the ambiguity of breath cycle, airflow structures which influence particle flow dynamics. Furthermore, it will be an important step in the extrapolation of respiratory mechanisms from surrogate animals to humans for various purposes, one of them being toxicological analysis.